

IMPACT OF THE SOUTHERN OCEAN WINDS ON SEA-ICE – OCEAN
INTERACTION AND ITS ASSOCIATED GLOBAL OCEAN CIRCULATION
IN A WARMING WORLD

A Dissertation

by

WOO GEUN CHEON

Submitted to the Office of Graduate Studies of
Texas A&M University
in partial fulfillment of the requirements for the degree of

DOCTOR OF PHILOSOPHY

August 2008

Major Subject: Oceanography

IMPACT OF THE SOUTHERN OCEAN WINDS ON SEA-ICE – OCEAN
INTERACTION AND ITS ASSOCIATED GLOBAL OCEAN CIRCULATION
IN A WARMING WORLD

A Dissertation

by

WOO GEUN CHEON

Submitted to the Office of Graduate Studies of
Texas A&M University
in partial fulfillment of the requirements for the degree of

DOCTOR OF PHILOSOPHY

Approved by:

Chair of Committee,	Achim Stössel
Committee Members,	Benjamin Giese
	Ping Chang
	Ramalingam Saravanan
Head of Department,	Piers Chapman

August 2008

Major Subject: Oceanography

ABSTRACT

Impact of the Southern Ocean Winds on Sea-ice – Ocean Interaction and
its Associated Global Ocean Circulation in a Warming World.

(August 2008)

Woo Geun Cheon, B.S., Yonsei University;

M.S. Yonsei University

Chair of Advisory Committee: Dr. Achim Stössel

This dissertation discusses a linkage between the Southern Ocean (SO) winds and the global ocean circulation in the framework of a coarse-resolution global ocean general circulation model coupled to a sea-ice model. In addition to reexamination of the conventional linkage that begins with northward Ekman transport and extends to the North Atlantic (NA) overturning, the author investigates a new linkage that begins with the Southern Hemisphere (SH) sea-ice – ocean interaction perturbed by the anomalous SO winds and extends to the SH overturning, the response of the NA overturning, and the long-term baroclinic adjustment of the Antarctic Circumpolar Current (ACC). How the above two linkages will interact with each other in a warming world is also investigated.

An interactive momentum flux forcing, allowing for the strength of momentum flux between atmosphere and sea ice to vary in response to the simulated sea-ice conditions, enhances wind-driven ice divergence to increase the fraction of leads and polynyas, which increases dense water formation, and thus intensifies convection. Within three experimental frameworks, this increased dense water consistently increases the

Antarctic Bottom Water formation, which directly intensifies the SH overturning and indirectly weakens the NA overturning. As a result of the hemispheric change in overturning circulations, the meridional density gradient across the ACC appears to increase, ultimately increasing the baroclinic part of the ACC via an enhanced thermal wind shear.

Subsequently, impacts of the poleward shifted and intensified SH subpolar westerly winds (SWWs) on the global ocean circulation are investigated in phases. When the SWWs are only shifted poleward, the effect of the anomalous winds is transmitted to the northern NA, decreasing both the NA overturning and the North Atlantic Deep Water (NADW) outflow. However, when the SWWs are shifted poleward and intensified, this effect is cut off by the intensified Deacon cell overturning, and is not transmitted to the northern NA, and instead increases the NADW outflow substantially. To sum up, with respect to the SO winds perturbed by the global warming, the SH overturning cell and the NADW outflow increase, leading to an increase in the volume transport of the ACC.

ACKNOWLEDGEMENTS

I am grateful to my advisor, Dr. Achim Stössel, for his assistance and guidance in the work presented here, and for his support and patience with me. I would like to thank other members of my committee: Dr. Benjamin Giese, Dr. Ping Chang, and Dr. Ramalingam Saravanan, and also Dr. Alejandro Orsi.

TABLE OF CONTENTS

	Page
ABSTRACT	iii
ACKNOWLEDGEMENTS.....	v
TABLE OF CONTENTS	vi
LIST OF FIGURES	ix
LIST OF TABLES	xii
CHAPTER	
I INTRODUCTION	1
II PREPARATION.....	6
A. Model description	6
B. Review of the linkage between the SO winds and global ocean circulation	9
C. Conceptual background of interactive momentum flux	15
III INTERACTIVE MOMENTUM FLUX FORCING OVER SEA ICE IN A GLOBAL OCEAN GCM.....	21
A. Introduction	21
B. Experiments	25
1. Reference experiment (REF)	25
2. Momentum flux affected by local sea ice (MFL)	26
3. Momentum flux affected by heterogeneous sea ice (MFH) ..	27
C. Results	31
1. MFL experiment	31
2. MFH experiment	38
3. MFH sensitivity experiments (MFHS)	41
D. Discussion and conclusions	45
IV RESPONSE OF SOUTHERN HEMISPHERE OVERTURNING TO THE INTERACTIVE MOMENTUM FLUX OVER SEA ICE AND	

CHAPTER	Page
ITS IMPACT ON THE GLOBAL OCEAN CIRCULATION	52
A. Introduction	52
B. Description of experiments	55
C. Results of reference experiments	57
D. Results of IMF experiments.....	63
1. The IMF-induced sea-ice – ocean interaction	64
2. The IMF-induced changes in meridional overturning circulations	69
3. Long-term baroclinic adjustment of the ACC to the IMF	72
E. Summary	73
V OCEANIC RESPONSE TO THE POLEWARD SHIFTED SOUTHERN HEMISPHERE SUBPOLAR WESTERLY WINDS	76
A. Introduction	76
B. Experimental setup	80
C. Results	83
D. Summary	99
VI SOUTHERN HEMISPHERE SEA-ICE – OCEAN INTERACTION AND GLOBAL OCEAN CIRCULATION IN A WARMING CLIMATE	100
A. Introduction	100
B. Experimental setup	103
C. SH sea-ice – ocean interaction in a warming climate	104
D. Global ocean circulation in a warming climate	112
E. Summary	114
VII FINAL DISCUSSION AND CONCLUSIONS	116
A. Interactive momentum flux over SO sea ice	117
B. Oceanic response to anomalous SO winds via the sea-ice – ocean interaction	118
C. Oceanic response to anomalous SO winds via the northward Ekman transport.....	119
D. Long-term baroclinic adjustment of the ACC to anomalous SO winds	122
E. Deficient baroclinic effects of mesoscale eddies	124

	Page
REFERENCES	127
APPENDIX I MODEL PHYSICS.....	136
VITA.....	147

LIST OF FIGURES

FIGURE	Page
2-1 Schematic diagram illustrating how the climate signal associated with the northward Ekman transport anomaly is transmitted into the northern North Atlantic	12
2-2 Schematic diagram illustrating three representative cells that can transport anomalous climatic signals originating from changes in the SO winds to the global ocean, and major correlations with one another	14
2-3 Schematic diagram of heterogeneous condition of sea ice and its interaction with the atmosphere in one grid cell of a general circulation model (buoyancy-driven turbulence: red arrow circle, shear-driven turbulence: blue arrow circle, form drag: dark blue arrow circle). Upward red arrows indicates the ocean-to-atmosphere heat loss via exposure of relatively warm ocean surface waters (-1.8°C) to extremely cold air (typically -30°C). The vertical scale of this figure is exaggerated	16
3-1 Mid-winter snapshot of (a) local Richardson number over the ice-covered part and (b) wind stress of REF	32
3-2 Mid-winter snapshot of (a) local friction velocity of MFL, (b) local drag coefficient of MFL, (c) wind stress difference MFL minus REF, and (d) sea-ice velocity difference MFL minus REF.....	33
3-3 Same as Fig. 3-2, but for winter mean rather than mid-winter snapshot ...	34
3-4 Western Weddell Sea winter-mean of (a) local Richardson number. MFL minus REF differences of (b) wind stress, (c) ice velocity, (d) ice thickness, (e) ice concentration, and (f) sensible heat flux	36
3-5 Western Weddell Sea winter-mean MFH minus MFL differences of (a) Richardson number. Otherwise as Fig. 3-4	38
3-6 Enlargement of the two critical coastal regions of Fig. 3-5d: (a) ice thickness, Fig. 3-5e: (b) ice concentration, and Fig. 3-5f: (c) sensible heat flux. Otherwise as Fig. 3-5d-5f	39
3-7 Winter-mean of (a) ice concentration and (b) Richardson number of MFL (left) and MFH (right)	40

FIGURE	Page
3-8 Mid-winter snapshot of large-scale Richardson number of MFHS4. Otherwise as Fig. 3-1a	42
3-9 Western Weddell Sea winter-mean MFHS4 minus MFH differences. Otherwise as Fig. 3-5	43
3-10 Global and annual-mean profiles of potential temperature (upper panel), and (b) salinity (lower panel) of REF (lines with open circles) and of MFHS4 (lines with filled circles), at quasi equilibrium after 1000 years of model integration	44
4-1 Meridional sections of potential temperature and salinity fields in the south Atlantic Ocean	59
4-2 Winter-mean ice concentrations and differences of wind stress over the SO sea ice	60
4-3 Differences of zonally averaged winter-mean ice concentration and annual net freezing rate (AIMF minus AREF: red, BIMF minus BREF: green, CIMF minus CREF: blue lines)	64
4-4 Zonally averaged meridional sections of the global potential temperature and salinity	67
4-5 Meridional overturning circulations in the Atlantic Ocean	70
4-6 Meridional overturning circulations in the Global Ocean	71
5-1 Zonally averaged annual-mean zonal wind stress	80
5-2 Annual-mean wind stress magnitude and curl of reference and anomaly .	81
5-3 Differences of zonally averaged winter-mean ice concentration and annual net freezing rate (APSW minus AREF: red, BPSW minus BREF: green, CPSW minus CREF: blue lines).....	83
5-4 Meridional overturning circulations in the Atlantic Ocean	85
5-5 Meridional overturning circulations in the Global Ocean	86
5-6 Meridional sections of global potential temperature and salinity	90
5-7 Zonally averaged global density ($\sigma_{s,\theta,p=2000m}$ and $\sigma_{s,\theta,p=0}$) fields (REF: solid, PSW: dashed lines)	91

FIGURE	Page
5-8 Vertical profiles of zonally averaged meridional velocity	94
5-9 Zonally averaged meridional velocity, potential temperature, and salinity at 20°S, and zonally averaged SSH averaged from 10°S to 10°N in the Atlantic Ocean for the first 100 years (BPSW)	96
5-10 Zonally averaged isopycnal and meridional SSH difference in the Atlantic Ocean	97
6-1 Schematic diagram of process of the SH atmosphere – sea-ice – ocean interaction in a warming world	102
6-2 Differences of zonally averaged winter-mean ice concentration and annual net freezing rate (BPSWI50S minus BREF: red, BPSW50S minus BREF: green, BIMFPSW50S minus BREF: blue lines)	104
6-3 Differences of winter-mean ice concentration and thickness	106
6-4 Differences of annual-mean SSH and potential temperature averaged from surface to intermediate depth (θ_I ; 712.5 m).....	107
6-5 Zonally averaged annual-mean convective potential energy release	108
6-6 Meridional overturning circulations in the Atlantic and Global Ocean	110
6-7 Zonally averaged global density fields ($\sigma_{s,\theta,p=2000m}$) fields	111

LIST OF TABLES

TABLE		Page
4-1	The hierarchy of model experiments	55
4-2	Equilibrium values of selected integrated quantities in respective reference and IMF applied case (NA overturning [Sv]: Maximum transport; NADW outflow [Sv]: NADW outflow across $30^{\circ}S$; ACC [Sv]: Drake Passage throughflow; $\theta_{z=4000m}$: global-mean potential temperature at 4000m depth; $S_{z=4000m}$: global-mean salinity at 4000m depth).....	57
5-1	As in Table 4-2 but for the comparison with the PSW-applied cases	84
5-2	Maximum transports of the NA overturning, Antarctic overturning, and SH overturning, outflow of NADW, and Drake Passage throughflow (ACC) in control case (CNTRL) and trend experiment of the PSW (results quoted from Oke and England (2004)). Unit of the NA overturning, NADW outflow, and ACC is Sv	87
6-1	As in Table 4-2 but for the comparison of BREF with the BPSWI50S, BPSW50S, and BIMFPSW50S	112

CHAPTER I

INTRODUCTION

The Southern Ocean (SO) is worthy of notice in respects of being connected to all oceans, being under the influence of the world-mightiest Southern Hemisphere (SH) westerly winds, being surrounded by the world-largest current, the Antarctic Circumpolar Current (ACC), and producing the world-densest water, the Antarctic Bottom Water (AABW). The Antarctic continent underlying a yearlong high-pressure center is surrounded by several yearlong low-pressure centers offshore north of coastline. Under the influence of these synoptic-scale atmospheric pressure fields, the sea-ice – ocean system forms a divergent field. The predominant SH westerly winds (SWWs) drive the deep and vigorous ACC eastward and push the Antarctic Surface Water (AASW) away from the continent through Ekman transport, which has both the effect of creating massive divergence-driven upwelling of the Circumpolar Deep Water (CDW) and of strongly tilting the isopycnal surfaces across the path of the ACC.

The SWWs also have been known to play a key role in driving the Atlantic Ocean (AO) ‘conveyor belt’ (Broecker 1987), which is composed of the northward Ekman transport in the latitude band containing the Drake Passage, North Atlantic (NA) overturning, deep southward return flow fed by the North Atlantic Deep Water (NADW) outflow, and wind shear-induced upwelling (Toggweiler and Samuels 1993, 1995; hereafter denoted as TS93 and TS95, respectively). A part of the conveyor belt, i.e. remote connection between the Ekman drift in the SWW zone and the NA overturning,

This dissertation follows the style and format of *Journal of Physical Oceanography*.

was questioned in Rahmstorf and England (1997; hereafter denoted as RE97). They suggested that the NA overturning is to some extent ‘modulated’ by the SWWs instead of being ‘controlled’. A simple predictive model of the structure of the oceanic pycnocline proposed by Gnanadesikan (1999; hereafter denoted as G99) supplies the hint toward the mechanism that can explain this remote connection between the SWWs and the NA overturning.

In addition to the direct influence of wind-driven circulation on which the integrated atmospheric variability is projected, the SO winds have an indirect influence on the ocean via the buoyancy-driven circulation associated with formation/melting and advection of sea ice. The seasonal evolution of sea ice is, among others, associated with brine rejection and fresh water release. Together with surface cooling, brine rejection determines the formation of dense water. Once dense water is formed at the surface, it can trigger deep convection and affect the global thermohaline circulation. During winter, ice-free ocean among sea ice, such as leads and polynyas, plays a key role of a gateway in the enormous ocean-to-atmosphere heat loss, leading to new ice formation and thus brine rejection. The wind-driven ice drift is essential for creating leads and polynyas. Using a coupled climate model of intermediate complexity, Saenko et al. (2002) showed that the wind-driven ice drift plays a key role in determining where and how much buoyancy fluxes are supplied to the ocean, and thus in controlling the sites and rates of deep- and intermediate-water formation in the SO. The impact of high frequency wind variability upon ice dynamics also appeared to increase the ice growth rate via increasing the sensible heat flux and widening the ice-free ocean, ultimately leading to an increase in dense water formation, convection, and the SH overturning cell (Stössel et al. 1998).

On the other hand, in the experiment of enhancing the resolution of sea-ice model coupled to a global ocean general circulation model (GCM), Stössel et al. (2006) showed that an incorporation of the coastal winds with well-reproduced coastal polynyas turn out to play a vital role in the formation of AABW.

The AABW has been known to occupy the abyssal basins of the world ocean with its relative cold and fresh waters, to form the southern sinking limb of ventilation in the SO, and to be in anti-correlation with the formation rate of NADW (Broecker 1998). The anti-correlation between the AABW and the NADW, known as the so-called “bipolar seesaw” balance, was recently extended even to the Pacific Ocean, showing an anti-correlation between ocean ventilation in the North Atlantic and ocean ventilation in the SO and the North Pacific (de Boer et al. 2007). Moreover, Stössel and Kim (2001) showed that an anomalous convection in the Weddell Sea modify the outflow of NADW in the sense that stronger AABW intrusion leads to weaker NADW outflow and vice versa. Therefore, it is to note that an anomalous climatic signal originated from the SO wind fields can be transmitted to the global ocean not only through the Atlantic Ocean conveyor belt perturbed by the wind-driven northward Ekman transport anomalies, but also through the northward intrusion of AABW perturbed by the wind-driven sea-ice – ocean interaction anomalies. Regardless of each route of change, a long-term adjustment by the baroclinic transports is supposed to change the meridional density gradient connected with the ACC, the thermal wind shear, and thus the intensity of ACC.

According to the recent Intergovernmental Panel on Climate Change (IPCC) Fourth Assessment Report, the Southern Annular Mode (SAM) that drifts toward a high index polarity gives rise to the poleward shifted and intensified SWWs as a result of the

greenhouse gas (GHG) warming in the SH. It indicates an intensification of the magnitude of the negative wind stress curl over the sea-ice – ocean system at the SH high latitudes, which is expected to vivify the sea-ice – ocean interaction. As stated earlier, the wind-driven sea-ice divergence plays a key role in determining the thermohaline flux forcing decisive of the sea-ice – ocean interaction, and besides the atmospheric momentum stress driving sea-ice drift is, basically, dependent on the heterogeneous atmosphere surface layer (ASL) condition over sea ice. Therefore, in the framework of sea-ice – ocean coupled GCM used in this study, a physically reasonable transmission of the atmospheric momentum to the sea-ice system, based on the ASL condition estimated by the simulated sea ice, is a prerequisite step toward investigating the sea-ice – ocean interaction and its associated impact on the global ocean circulation.

In coarse-resolution global ocean GCMs available for the long-term integration, an artificial treatment, e.g. increasing restoring salinity near the Antarctic continent during austral winter (Oke and England 2004), is still necessary to reproduce reasonable ventilation in the SO regardless of being used alone or being coupled to the sea-ice model and/or the atmosphere model. Therefore, many climatic studies associated with the SO winds and/or carbon cycle feedbacks have exhibited a tendency to focus their attention too much on the Ekman flux driving the AO conveyor belt (e.g. Gnanadesikan 1999; Gnanadesikan and Hallberg 2000; Brix and Gerdes 2003; Oke and England 2004; Russell et al. 2006; Toggweiler et al. 2006). In other words, the impact of the complex SH atmosphere – sea-ice – ocean interaction on AABW has been ignored, and moreover the AABW has been regarded as playing a passive, secondary role in the global ocean

circulation, compared to that of NADW, even though the SO winds play a key role in the formation of AABW.

The study presented here is composed of four steps: 1) to investigate the sensitivity of SO sea ice to the strength of the atmospheric interactive momentum flux (IMF) forcing via applying the ASL parameterizations to sea-ice model, 2) to investigate the long-term oceanic response to the application of the IMF, 3) to investigate the long-term oceanic response to the poleward shifted SWWs, and finally 4) to synthesize the impacts of the poleward shifted and intensified SWWs and the IMF on the SH sea-ice – ocean interaction and global ocean circulation. This thesis has the following structure. Details of numerical model, the linkage between the SO winds and the global ocean circulation, and the conceptual background of the IMF are described in the next chapter. The first, second, third, and fourth steps are in order described in chapter III, IV, V and VI. Chapter VII is composed of final discussion and conclusions.

CHAPTER II

PREPARATION

A. Model description

The basic tool for this investigation is a global coarse-resolution version of the Hamburg Ocean Primitive Equation (HOPE) model (Wolff et al., 1997) which is coupled to a sea-ice model. A full detail of model physics for the ocean and the sea ice part is given in appendix I. The thermodynamics of the sea-ice component follow Owens and Lemke (1990), and Parkinson and Washington (1979), and the viscous-plastic dynamics are based on Hibler (1979). The model is run on a $5^\circ \times 5^\circ$ global E -grid (Arakawa and Lamb 1977), yielding an effective grid point spacing of 3.5° . In vertical, 11 vertical layers are used. Horizontal velocity, temperature, and salinity are defined at depth levels 25, 75, 150, 250, 450, 700, 1000, 2000, 3000, 4000, and 5000 m , and vertical velocity and pressure at intermediate levels. This model includes a realistic smoothed topography-following bottom-layer depth, and a prognostic free sea surface. The resolution of the southern hemisphere sea-ice component of this model is 9-fold higher in both principle horizontal directions, yielding a grid spacing of about 22km (Stössel et al., 2007). Furthermore, the model includes a plume-convection parameterization following Paluszkiwicz and Romea (1997), as introduced by Kim and Stössel (2001).

The overall atmospheric forcing employs climatologic monthly winds and air temperatures following Drijfhout et al. (1996). In order to mimic the freshwater flux,

upper-ocean salinities are restored to the Levitus (1982) climatology, unless there is sea ice, in which case this is determined by the freezing and melting rates. Daily wind fields of the European Centre for Medium-Range Weather Forecasts (ECMWF) operational analyses of a year (1986) with average sea-ice condition according to Gloersen et al. (1992) are employed south of 50°S, in particular to drive Southern Ocean sea ice dynamically as well as thermodynamically, because high-frequency wind variability was identified to play a decisive role in simulating the first-order characteristics of Southern Ocean sea ice (e.g., Stössel, 1992). For simplicity, the albedo and insulation effect of snow on sea ice has been approximated, by specifying the snow depth to be 0.1 *m* where the sea-ice thickness is larger than 0.1 *m*.

In all experiments, the thermodynamic ice growth and decay are determined by separate heat-balance calculations over the subgrid ice-covered and ice-free part. For each part, the local heat flux is calculated from solar radiation, long wave radiation, sensible and latent heat flux by empirical formulas. In addition, the ice-covered part requires a conductive heat flux through ice (and snow).

As described in Stössel et al. (2008), following Louis (1979), south of 50°S, in particular over the high-resolution sea ice, the turbulent heat fluxes are modified by the ASL processes that are determined on the basis of the Monin-Obukhov similarity theory. The following stability functions are used for momentum, heat and moisture:

$$F = 1 - \frac{9.4 Ri}{1 + c |Ri|^{0.5}}, \quad \text{if } Ri < 0, \quad (2.1a)$$

$$F = \frac{1}{(1 + 4.7 Ri)^2}, \quad \text{if } Ri \geq 0, \quad (2.1b)$$

with $c = C^* (\kappa / \ln(z_a / z_0))^2 9.4 \sqrt{z_a / z_0}$, where κ is the von Karman constant, z_a is the height of the forcing level (assumed to be 30 m), in which subscript ‘a’ refers to the atmosphere, z_0 is the local roughness length, and the coefficient $C^* = 7.4$ for momentum flux, and 5.3 for heat and moisture fluxes. Note that (2.1a) follows the original Louis (1979) form rather than the modification introduced by Claussen (1991a) as used in Stössel & Claussen (1993, hereafter denoted as SC93). That form turned out to make the stratification too stable, and the drag coefficient (see section III.B.2) too small compared to what is generally derived from observations (e.g., Uotila et al., 2000). For each surface condition, i.e. for the ice-covered (index i) and ice-free (index o) part, respectively, the local Richardson number (Ri) of the surface layer is

$$Ri_{i,o} = \frac{gz_a}{\theta_{i,o}} \cdot \frac{[(\theta_a - \theta_{i,o}) + 0.61\theta_{i,o}(q_a - q_{i,o})]}{|\vec{V}_a|^2} \quad (2.2)$$

with potential temperature θ , specific humidity q , and wind velocity $|\vec{V}_a|$. The corresponding local sensible heat flux (Q_{SE}) is computed following Louis (1979) and Claussen (1991a and b):

$$Q_{SEi,o} = \frac{\rho_a c_{pa} \kappa^2 |\vec{V}_a| (\theta_a - \theta_{i,o}) F_{i,o}}{\ln(z_a / z_{0i,o}) \ln(z_a / z_{Ti,o})} \quad (2.3)$$

where ρ_a is air density, c_{pa} is specific heat of air at constant pressure, and z_T is the roughness length for heat. The latent heat flux is calculated similarly, with $c_{pa}(\theta_a - \theta_{i,o})$ being replaced by $L_v(q_a - q_{i,o})$, where L_v is the latent heat of evaporation. The roughness lengths for heat and moisture are considered to be the same, which is a reasonable assumption referring to recent findings from measurements (e.g., Andreas et al., 2005).

Following Claussen (1991a) and Brutsaert (1979), they are calculated as a function of the local roughness lengths and the local friction velocities ($u_{*i,o}$), which in turn are determined by

$$u_{*i,o}^2 = \left[\frac{\kappa}{\ln(z_a/z_{0i,o})} |\vec{V}_a| \right]^2 F_{i,o} \quad . \quad (2.4)$$

The experiments described in the following section differ only in the way the momentum flux is modified by the simulated sea-ice conditions. Note that even though this parameterization allows for a more detailed representation of ASL processes, the air temperature field is derived from a monthly climatology (see above), while the relative humidity and cloudiness are specified to be constant in time and space (80% and 70%, respectively). This has been assumed for simplicity, and to make the Southern Ocean forcing fields more consistent with the global forcing fields, and less dependent on individual years, while allowing for real-time daily wind variability over the high-resolution Southern Ocean sea-ice pack.

B. Review of the linkage between the SO winds and global ocean circulation

Part of this study aim at investigating the impact of the SO winds on the global ocean circulation. The SO winds can generate two large external forces affecting the global ocean circulation in the SH: 1) a wind-driven northward Ekman transport and 2) a wind-driven sea-ice – ocean interaction. Most previous studies have laid emphasis on the impact of the northward Ekman transport on meridional overturning circulation (MOC) in the Northern Hemisphere (NH), which is representative of the NA overturning, and its

corresponding changes in the global ocean circulation. On the other hand, the wind-driven SH sea-ice – ocean interaction is essential for the SH overturning, and thus is expected to also have a significant influence on the global ocean circulation. In this section, a historical review of the linkage between the SO winds, northward Ekman transport, and NA overturning is described in detail below. Then, new proposal for the possible linkage between the SO winds, northward Ekman transport, and SH overturning is followed.

The idea about the ocean ‘conveyor belt’ (Broecker 1987) constitutes an important milestone toward understanding the linkage between the SWWs and the global ocean circulation. The northern part of the SO is under the strong influence of the yearlong prevailing SWWs, which are a major driving force for an enormous northward Ekman transport. The Ekman divergence associated with the westerly winds is virtually causing the widespread upwelling of deep water from the interior of the ocean. Here the so-called “Drake Passage effect” (TS93) applies. Drake Passage is the one place in the world ocean where a meridional continental barrier up to the surface does not exist, so that no zonal pressure gradient to balance the Coriolis force exists, which means no net meridional geostrophic flow across the latitude band of Drake Passage in the upper ocean. This also implies that there is no shallow returning southward geostrophic flow that feeds the water pushed north in the Ekman drift by way of upwelling. However, at depths below the sill connecting the southern flank of South America with the Antarctic peninsula, or at depths below the tops of mid-ocean ridges spanning the latitude band of Drake Passage, east-west pressure gradient can exist, so that geographically balanced southward flow comes across the latitude band of Drake Passage below the ridge depth.

Then, where is the place for that large amount of deep water to form? TS93 and TS95 argued that the water pushed north in the Ekman drift must sink in the NA as NADW because anywhere else the ocean is too stratified for deep downwelling to occur. Using a coarse-resolution ocean GCM, they showed a linear relation between northward Ekman flux at the tip of South America and the NADW outflow. That is, net northward Ekman transport across the open circumpolar zone is provided by upwelling south of the zone, which in turn is supplied by a net southward geostrophic flow of deep water below the crests of major ridges in the zone. It implies that an anomalous climatic signal originating from changes in the intensity of SWWs has a strong influence on the AO conveyor belt, passing through three choke points, i.e. northward Ekman Flux, the NADW formation, and the NADW outflow.

The mechanism that can explain the remote connection between northward Ekman transport under the influence of the SO winds and NA overturning is as follows. In general, the sea surface height is higher at the equator than in high latitudes, and thus this sea surface height difference will cause a meridional pressure difference. In the NH, the pressure decreases northward along the western boundary as long as the interior stream function ψ_I is positive just outside the western boundary current, that is:

$$\frac{1}{\rho} \left(\frac{\partial p}{\partial y} \right)_{wall} = -\beta \psi_I(x_w, y), \quad (2.5)$$

where β is the northward spatial derivative of Coriolis force f and x_w indicates the western boundary. According to classical boundary layer theory, the governing equation can be written as:

$$u \frac{\partial v}{\partial x} + v \frac{\partial v}{\partial y} = \beta \psi_I(x_w, y) + A_H \frac{\partial^2 v}{\partial x^2}. \quad (2.6)$$

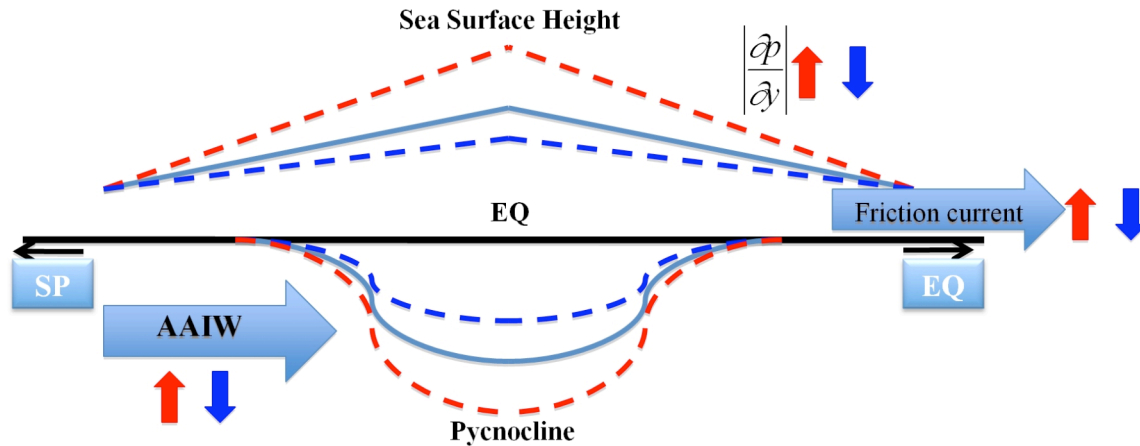


Fig. 2-1. Schematic diagram illustrating how the climate signal associated with the northward Ekman transport anomaly is transmitted into the northern North Atlantic.

Solutions for northward flow in the boundary layer exist as long as $\beta\psi_l$ is positive, as it is in the subtropical gyre. That is, the effective pressure gradient due to the sea surface height difference will produce a frictional flow near the western boundary, which plays an important role in transmitting climatic signals resulting from anomalous SO winds to the northern NA where dense water forms to sink (G99). A simple schematic diagram in Fig. 2-1 illustrates how this climate signal is transmitted into the northern NA. If the SO winds increase suddenly, an increased northward Ekman transport increases the AAIW, and thus the amount of cold and fresh water sinking along the isopycnal layer. It results in deepening of the pycnocline because more water is being added to these isopycnal layers than is being removed to the Northern Hemisphere. As the pycnocline deepens, the sea surface in low latitudes elevates, and thus a meridional pressure gradient increases, leading to increases in the northward frictional flow near the western boundary, the formation rate of NADW, and the southward outflow of NADW.

RE97 developed a somewhat different hypothesis, against the dominance of the SO winds on the Atlantic conveyor belt proposed by TS93 and TS95. Their major point is, as mentioned earlier, the role of SSWs in the NA overturning as a modulator, not as a controller. They showed that the NADW outflow does not vary in direct proportion to the amount of northward Ekman flux when a hybrid model was used instead of an ocean-only GCM forced by a thermal restoring boundary condition. According to their argument, the use of thermal restoring boundary conditions leads to a neglect of temperature feedback, which was identified by Rahmstorf (1995) as the major negative feedback regulating the overturning strength in the NA. That is, when an increased (decreased) northward Ekman drift due to strengthened (weakened) SO winds increases (decreases) the formation of NADW and NADW outflow, the strengthened (weakened) NA overturning plays a role in increasing (decreasing) northward heat transport, and then an increased (decreased) upper-ocean temperature in high latitudes of the NA leads to an increase (decrease) in stratification of the water column in high-latitude, which finally counteracts the previously strengthened (weakened) overturning. Moreover, changes in SO winds appeared to have an influence on the Deacon cell, the Antarctic cell, and bottom cell overturning.

As explained in the first chapter, the AABW is known to be in anti-correlation with the NADW (Broecker 1998), which is to a large extent affected by SO convection (Stössel and Kim 2001). Moreover, the wind-driven sea-ice divergence plays a key role in providing the SO with a realistic thermohaline flux forcing (Saenko et al. 2002), because the detailed sea-ice textures, such as leads and polynyas, are mainly driven by winds (Wadhams 2000), and those ice-free areas exposed to cold high-latitude

atmospheric conditions thus are most decisive for the heat and freshwater flux for the ocean, and thus a realistic representation of the long-term deep-ocean properties (Stössel and Kim 2006; Stössel et al. 2007).

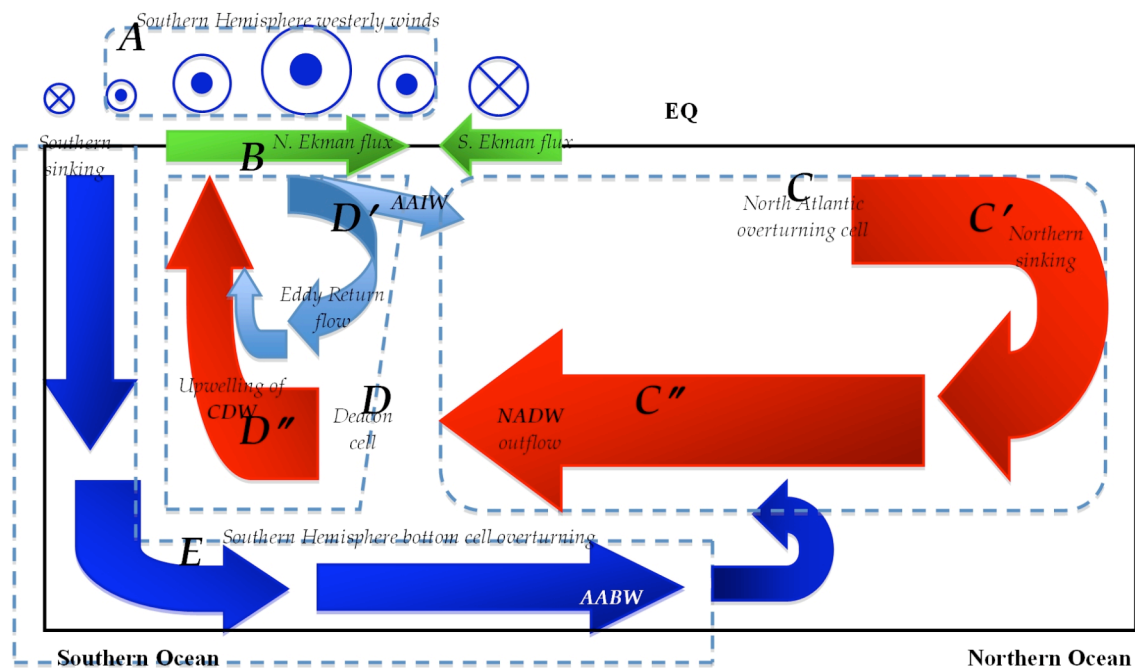


Fig. 2-2. Schematic diagram illustrating three representative cells that can transport anomalous climatic signals originating from changes in the SO winds to the global ocean, and major correlations with one another.

A simple schematic diagram illustrated in Fig. 2-2 synthesizes major paths that transport climatic signals originating from the change in SO winds to the global ocean and major correlations with one another, as described in the previous four paragraphs. The most direct and simplest linkage is the northward Ekman transport due to the SWWs, i.e. a momentum transmission from A to B, which as a whole leads D denoting the Deacon cell. The Ekman drift has the effect of both building divergent fields, and thus driving the upwelling of CDW denoted as D'', and of controlling the AAIW and eddy-

return flow denoted as D' with its dynamic and thermodynamic components. The eddy-return flow can act not only to take a substantial amount of northward Ekman transport to send back to the south with no density change but also to feed the northward Ekman transport (Marshall and Radko 2003, Hallberg and Gnanadesikan 2006), which therefore, together with the negative temperature feedback (Rahmstorf 1995), can impose restrictions on the linkage between B and C proposed by TS93 and G99. E , denoting AABW, was previously described to be in anti-correlation with C . The following two chapters focus on exploring the linkage between A and E , and its impact on the global ocean circulation.

C. Conceptual background of interactive momentum flux

A concrete way of applying the interactive momentum flux (IMF) to the sea-ice model is described in the next chapter, while this section is going to deal with its conceptual background. In the planetary boundary layer (PBL), heterogeneous features, such as surface heat flux and surface topography, to a large degree affect the characteristics of turbulence structure, which determines the vertical transfer of heat, momentum, and humidity. The limitation of resolution in numerical models causes the flow to be divided into the resolved (grid-scale) part and the unresolved (sub-grid scale) part. In the coarse-resolution GCMs capable of long-term integrations required in climate studies, the flow driven by the surface heterogeneities belongs to the category of the unresolved part, which necessitates applying suitable parameterizations to the numerical

model in order to resolve the effect of fractional sub-grid scale heterogeneities. The surface of sea ice is also characterized by strong surface heterogeneities.

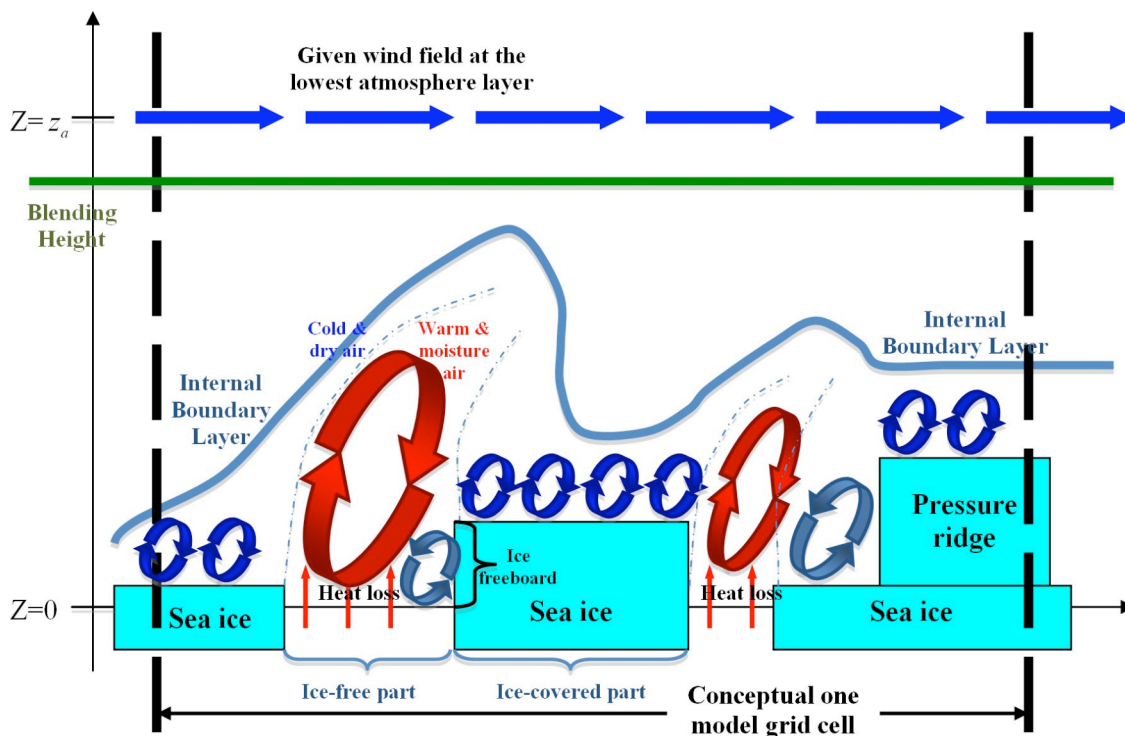


Fig. 2-3. Schematic diagram of heterogeneous condition of sea ice and its interaction with the atmosphere in one grid cell of a general circulation model (buoyancy-driven turbulence: red arrow circle, shear-driven turbulence: blue arrow circle, form drag: dark blue arrow circle). Upward red arrows indicate the ocean-to-atmosphere heat loss via exposure of relatively warm ocean surface waters (-1.8°C) to extremely cold air (typically -30°C). The vertical scale of this figure is exaggerated.

During winter, large differences between the surface temperatures of ice-free part and ice-covered part result in large horizontal gradients of the near-surface stability, while heterogeneous surface topography, characterized by ice floes of various sizes with different ice freeboard, different distances of each other, and wind-induced pressure ridges, results in large heterogeneities of the surface roughness. A simple schematic

diagram illustrated in Fig. 2-3 directly indicates the complex heterogeneities occurring over sea ice, and provides hints on how these small-scale features can be resolved within one grid cell of a large-scale model. The atmospheric momentum flux not only determines sensible and latent heat flux with its high frequency variability, but also controls wind-driven sea-ice motion and thus divergent or convergent patterns of ice drift with its integrated effect, both of which play a key role in determining where and how much thermohaline flux forcing is fed to the ocean. A transmission of physically reasonable momentum stress from the atmosphere layer to the ice-ocean surface, i.e. atmospheric momentum flux, is to that extent essential, and the amount of flux depends on how strongly the two spheres are coupled. As illustrated in Fig. 2-3, turbulences of various origin, mainly determined by the surface condition and the wind, are major driving forces of the coupling, while in case of no turbulence, albeit not illustrated here, the two spheres can get entirely decoupled, which means no exchange of momentum. In general, the turbulent exchange of atmospheric momentum to the earth's surface is determined by the frictional drag exerted by the surface roughness, wind speed at certain height, and surface stratification, which is well described in the following equation. The friction velocity (u_*) is defined from the vertical eddy flux of momentum ($\overline{w'u'}$):

$$\overline{w'u'} \equiv u_*^2 = \left(C_d \left| \vec{V}_a \right| \right)^2 F_M, \quad (2.7)$$

where C_d is the drag coefficient, \vec{V}_a is the wind speed at the lowest atmosphere layer in the numerical model, and F_M is the stability function for momentum. Therefore, ice dynamics based only on the given wind, i.e. \vec{V}_a , does not seem to be physically reasonable.

Then, for the given wind fields in the GCMs, how can we provide the surface of sea ice with the physically reasonable atmospheric momentum stress that feels these heterogeneous features, the scales of which are smaller than what the model can directly resolve? A straightforward procedure that parameterizes sub-grid scale features over the heterogeneous sea ice is to divide each model grid cell in an ice-free part and an ice-covered part by way of calculating individual local properties separately, and then combine them by a weighted average due to each fraction. Two basic types of parameterization have been studied: the so-called 1) parameter- aggregation method and 2) flux-aggregation method. In the parameter-averaging method, the local surface properties such as surface temperature, surface humidity, and roughness length at each surface condition are averaged first in the grid cell by fractionally weighted function, and then fluxes are calculated. In the flux-averaging method, fluxes over ice and over open water are calculated separately, and the entire flux is the concentration weighted average of both fluxes (Claussen 1990, 1991b). An advantage of using the flux-aggregation method in the GCM is that the nonlinear dependence of the heat flux on ice concentration that emerges with the parameter- aggregation method can be avoided. As evaluated by the comparison of the two methods in Grötzner et al. (1996), for a fractional sea-ice cover the resulting sensible heat flux shows a simple linear increase from minus few hundreds Wm^{-2} in the case of open water to zero in the case of compact sea ice of 100% when the flux-averaging method is applied, while it rapidly reaches almost zero for a sea-ice cover of more than 70% when the parameter-aggregation method is applied. Even below this ice concentration, the ocean-to-atmosphere heat loss is underestimated. The problem of this nonlinearity is that even very small percentage of open water among sea ice pack,

conditionally, can exert a large effect on stratification in the whole grid cell, implying that the parameter-aggregation method is likely to miss the effect of this heterogeneity. Therefore, the flux-aggregation method is employed in this study, instead of the parameter-aggregation method.

Here is another concept to be considered in order to apply the flux-aggregation method to the numerical model used in this study. When air flows over heterogeneous terrain, the boundary layer can no longer be treated as in a steady state and as horizontally homogeneous. The flow has to adjust to the varying surface characteristics, and internal boundary layers develop. The surface exchange processes inside those internal boundary layers depend on local properties of the surface and the overlaying air. Below the internal boundary layer, surface exchange processes are, as illustrated in Fig 2-3, to a large extent dependent on local surface condition, while further away from the surface, these internal boundary layers merge, and individual differences of the surfaces are no longer visible. The “blending height” concept is a useful approach for the parameterization of spatially averaged turbulent fluxes over heterogeneous terrain. Mason (1988) defines the blending height as the scale height where the flow changes from the equilibrium state dependent on the local surface condition to that independent of horizontal distribution of heterogeneous surface condition. I.e., individual local “small-scale” atmospheric properties below the blending height (or internal boundary layer) are expressed as one “large-scale” atmospheric property representing the entire grid cell by a weighted average of the small-scale properties of each fraction.

Through the inclusion of the ASL parameterizations described above, it becomes possible to provide the sea ice with the realistic atmospheric momentum stresses based

not only on the wind fields at the lowest layer but also on the heterogeneous surface condition of sea ice, which is the concept of the “interactive momentum flux” (IMF). This section reviewed the overall concept of the IMF, and a more detailed theory of this is described in the following chapter.

CHAPTER III

INTERACTIVE MOMENTUM FLUX FORCING OVER SEA ICE
IN A GLOBAL OCEAN GCM *

A. Introduction

While the ice-free part largely enhances heat and moisture flux, it is mainly opened or closed by dynamical processes. The coastal polynyas are most commonly produced and kept free of a continuous ice cover in winter by powerful katabatic winds (e.g. Pease, 1987), and leads form as a result of divergent or shearing ice motion rather than local ice melting (e.g., Wadhams, 2000). Therefore, in coupled sea-ice - ocean modeling studies, the dynamic part of a sea-ice model has been found to play a major role in describing the evolution of sea ice. Hibler and Ackley (1983), Stössel et al. (1990), Pollard and Thompson (1994) and Wu et al. (1997) revealed a significant impact of sea-ice dynamics on ice thickness and ice extent in the Southern Ocean, and found that its inclusion made the simulated sea ice far more realistic. Using a global sea-ice - ocean model, Fichefet and Morales Maqueda (1997) showed that the omission of sea-ice dynamics induces a decrease in the ice extent and an increase in the total ice volume all year long in both hemispheres. The impact of sea-ice dynamics on the interaction between atmosphere and ocean was recently investigated in a coupled ocean – sea-ice - atmosphere general circulation model (GCM) (Ogura et al, 2004). When atmosphere –

* Reproduced by permission of American Geophysical Union. Stössel A., W.-G. Cheon, and T. Vihma, Interactive momentum flux forcing over sea ice in a global ocean GCM, *Journal of Geophysical Research*, **113**, C05010, doi:10.1029/2007JC004173, 2008.

ocean interaction is considered, the inclusion of sea-ice dynamics yields a significantly reduced summer ice extent and, in addition, a negative feedback associated with cloud increase. They showed that also in a framework that is coupled to the atmosphere, sea-ice dynamics leads to a reduction of sea-ice thickness. Besides ice dynamics, the oceanic heat flux is a major contributor limiting ice thickness and extent in the Southern Ocean (e.g., Winton, 2003; Bitz et al., 2005).

A key to a realistic sea-ice simulation is that the fluxes of momentum, heat and moisture be influenced by the large horizontal variations of the near-surface stability, which is mainly determined by the large difference in surface temperature between the ice-covered and ice-free part. It is also affected by heterogeneous surface roughness, which is characterized by the wide range of ice floe, lead and pressure-ridge sizes (e.g., Lüpkes and Birnbaum, 2005). Turbulent exchange of atmospheric momentum to the earth's surface is a consequence of the frictional drag exerted by the surface roughness. Both the low-level wind shear and the surface drag increase with increasing surface roughness, as well as with increasing wind speed at some reference height (Arya, 1999). The exchange of momentum between atmosphere and sea ice plays an important role in feedbacks, e.g. in terms of the size of leads and polynyas, and the height of pressure ridges, because both are directly influenced by the momentum flux. There are numerous studies on the determination of the total wind drag over the ice pack using observational data. Hanssen-Bauer and Gjessing (1988) proposed total drag over an area of sea ice as a function of ice concentration, mean height of ice freeboard, length of ice floes, and typical roughness of ice and sea surface on the basis of the drag-partition theory of Arya (1973, 1975). Garbrecht et al. (2002) and Vihma et al. (2005) improved the

parameterization of the drag coefficient using Monin-Obukhov similarity theory on the basis of their observational data from ice-covered regions.

On the other hand, Claussen (1990) presented average surface fluxes over heterogeneous surface conditions leading to the concept of the blending height over heterogeneous sea ice (Claussen, 1991a, 1991b; Vihma, 1995). This concept is associated with the flux-averaging method (Claussen, 1990) or the mosaic method (Vihma, 1995). With this method, the individual fluxes over the sub-grid scale ice-covered and ice-free part are composed by a linearly weighted function of ice concentration to arrive at a “large-scale” flux that is valid for the whole grid cell. This is considered to be a more physical approach than deriving the large-scale flux as a function of the averaged surface parameters (e.g., Grötzner et al., 1996). Birnbaum and Lüpkes (2002) additionally accounted for the momentum flux due to form drag in the calculation of the blending height. This was recently compared with prior parameterization schemes, slightly modified by additional consideration of a form drag contribution over open ocean (Lüpkes and Birnbaum, 2005).

Using a large-scale sea-ice – oceanic mixed-layer model for the Southern Ocean, Stössel and Claussen (1993) (SC93) applied the flux-aggregation and blending-height concepts in an ASL parameterization to modify the strength of the atmospheric forcing as a function of the simulated sea ice. In this approach, the momentum flux driving the sea ice was computed as a function of a large-scale stability function and a large-scale roughness length including the effect of form drag. Additionally, a large-scale friction velocity and the blending height were calculated to determine a large-scale drag coefficient, which ultimately modified the wind stress as a function of the simulated

heterogeneous sea-ice conditions. This work resulted in an overall enhancement of the momentum flux associated with both a reduction of the ASL stratification and an increase of the roughness length.

Complementary to this study, Grötzner et al. (1996) presented the impact of sea-ice in-homogeneity in an atmospheric GCM, using the same ASL parameterization, but without interactive sea ice. Several other studies have addressed the effects of heterogeneous sea-ice cover on the atmosphere (e.g., Andreas et al., 1984; Alam and Curry, 1997; Vihma and Brümmer, 2002; Pinto et al., 2003; Drusch, 2006). Losch et al. (2006), on the other hand, constitutes a study on the effects of the subgrid-scale heterogeneity of sea ice on vertical mixing in the ocean.

In this study, the impact of the interactive momentum-flux parameterization for heterogeneous sea-ice surface conditions of SC93 is re-evaluated in the framework of a global ocean GCM. For this purpose, three basic experiments were carried out, all of which include the same ASL parameterization, but differ in the way it affects the momentum flux over ice. In the first experiment (the reference case), the momentum flux is independent of the simulated sea-ice conditions. In the second experiment, the momentum flux over ice will be affected by the local ice thickness. In the third experiment, following SC93, the heterogeneity of the simulated ice pack is taken into account when calculating the momentum flux over ice by making it a function of the simulated ice thickness and concentration.

An at least equally important counterpart to the interactive momentum transfer between sea ice and atmosphere is that between sea ice and ocean (e.g., McPhee and Stanton, 1996). While one could argue that this is to some extent included by the fact that

in our model the sea ice is interactively coupled to the ocean (in contrast to the atmosphere), modifications of the ice – ocean drag possibly arising from processes such as melting or (subgrid-scale) instabilities in the oceanic boundary layer are not considered in this study (see section D).

The rest of this chapter is organized as follows. The way the experiments differ in their momentum-flux forcing is presented in section B. The impact of these modifications is presented in section C. A discussion and conclusions are given in section D.

B. Experiments

1. Reference experiment (REF)

Even though in REF a friction velocity is calculated, based on (2.4), it is not being used to modify the momentum flux. The wind stress affecting the sea-ice drift is thus independent of the simulated surface conditions. It has been derived from the standard 1000 *hPa* wind fields of daily operational ECMWF analyses (see section 2.A) assuming a constant drag coefficient of $C_{dr} = 0.0012$. To some extent, the 1000 *hPa* wind field will depend on the surface and atmospheric boundary layer conditions of the ECMWF model. In 1986, the year from which the current wind data was extracted, the sea-ice boundary condition of that model was specified to be climatologic with the ice concentration in an atmospheric grid cell of the order of 120 km being either 100% or 0%, and in the former case 1 *m* thick in the Southern Ocean (e.g., Vihma et al., 2002; Connolley and Harangozo, 2001). Except for the ice edge, this coarse assumption implies homogeneous

surface conditions over sea ice in winter time, thus providing ideal conditions for modifying the momentum flux as described in the following experiments.

2. Momentum flux affected by local sea ice (MFL)

The exterior dynamical forces affecting an area of pack ice are the drags from ocean currents and winds. The wind stress on ice is determined by the friction velocity, which in turn depends on the wind speed, ice roughness, and stability of the ASL (see (2.4)). In MFL, a local drag coefficient, C_{di} , is calculated as

$$C_{di} = \left[u_{*i} / |\vec{V}_a| \right]^2 . \quad (3.1)$$

It represents the transition between momentum in balance with the underlying surface and momentum at z_a , and is used to modify the wind-stress components over ice by

$$\tau_{ix}^{MFL} = C_{di} \tau_{ix}^{REF} / C_{dr} = \rho_a C_{di} u |\vec{V}_a| = \rho_a u u_{*i}^2 / |\vec{V}_a| , \quad (3.2a)$$

$$\tau_{iy}^{MFL} = C_{di} \tau_{iy}^{REF} / C_{dr} = \rho_a C_{di} v |\vec{V}_a| = \rho_a v u_{*i}^2 / |\vec{V}_a| . \quad (3.2b)$$

Accordingly, $|\vec{\tau}_i|^{MFL} = \rho_a u_{*i}^2$, with u_{*i} following from (2.4). Thus, the wind stress is now a function of the local ASL stability, and thus a function of the simulated local ice (and snow) thickness affecting the surface temperature, but not directly a function of ice concentration. To focus entirely on the momentum flux, the wind speed used to calculate the turbulent heat fluxes is the same in all experiments.

3. Momentum flux affected by heterogeneous sea ice (MFH)

For large-scale modeling, sub-grid scale effects due to heterogeneous compositions of the surface may be considered by weighting the local surface properties linearly with the surface composition. Observations, however, imply that certain surface features, e.g. leads in the case of sea ice, may dominate the large-scale characteristics, even when their fraction is rather small (Claussen, 1991b). The flux-aggregation scheme (Claussen, 1995) or mosaic method (Vihma, 1995) was introduced to account for such nonlinearities arising from sub-grid stratification changes. Locally, i.e., separately computed surface fluxes are aggregated by weighting the individual local flux contributions by their fractional area (Grötzner et al., 1996). In our set of experiments, only MFH uses a sea-ice driving momentum flux that is affected by the heterogeneity of the sea-ice pack, whereas this flux is independent of the surface characteristics in REF, and only dependent on the local sea-ice properties and stratification in MFL.

Adopting the blending-height concept, the aggregated flux is modified to become valid for large-scale, grid-cell averaged quantities, because at the blending height, the overall stress and energy fluxes change from a local equilibrium state to a state that is independent of the horizontal position (Mason, 1988). The prefix ‘large-scale’, therefore, refers to merged properties above the blending height. Using the flux-aggregation method in conjunction with the blending-height concept, a large-scale roughness length and a large-scale friction velocity are calculated to arrive at a large-scale wind stress. In sea-ice areas, the large-scale roughness length is, in general, determined by the freeboard of ice floes, by the size of the floes, by the height, angle, and spatial frequency of pressure

ridges, by the local skin frictions, and by the sea-surface roughness of the ice-free part (surface gravity and capillary waves). Except for the impact of pressure ridges, these factors are accounted for in determining the large-scale roughness length in MFH, following SC93. The ice freeboard (h_f) is given by

$$h_f = [h_i(1 - \rho_i/\rho_w) + h_s(1 - \rho_s/\rho_w)]/N_i, \quad (3.3)$$

where ρ_i is the density of sea ice, ρ_w is the density of water, ρ_s is the density of snow, h_i is the grid-cell mean ice thickness, h_s is the mean snow thickness, and N_i is the ice coverage per grid cell, i.e. the ice concentration.

The concept of the “relative length” β ($\beta = L_i/h_f$) introduced by Hanssen-Bauer and Gjessing (1988) requires an average floe size (L_i), which we parameterize as a function of the actual ice thickness \tilde{h}_i of the ice-covered part of a grid cell, i.e. $\tilde{h}_i = h_i/N_i$. Following SC93, $L_i = \tilde{h}_i \cdot 100$. A “horizontal scale of roughness variations” (\hat{L}), which is the sum of the (upwind) floe and lead size, i.e. $\hat{L} = L_i + L_o$, is used to estimate the blending height. Since the sea-ice model does not resolve individual floes and leads, the lead size (L_o) is being derived from the ice concentration. I.e., if the grid-cell mean ice thickness is 0.5 m and the ice concentration 90%, the floe size will be 56 m and the lead size 6 m. For the same mean thickness, but a concentration of 50%, the flow and lead sizes are equal at 100 m. Following Claussen (1991a,b), the blending height (z_b) is expressed as

$$z_b = \langle z_0 \rangle^{0.2} (\hat{L}/2)^{0.8}. \quad (3.4a)$$

and the aggregated roughness length $\langle z_0 \rangle$ reasonably represented by

$$\langle z_0 \rangle = z_{0i}^{N_i} \cdot z_{0o}^{(1-N_i)}. \quad (3.4b)$$

Note that this expression renders the blending height independent of the stability in the ASL, in contrast to nature. According to Claussen (1991b), this assumption can be made, because the large-scale momentum flux does not vary significantly with z_b for the range of \hat{L} and $\langle z_0 \rangle$ considered here. For the two cases mentioned above, this will yield a blending height of about 4 m in the former case, and 10 m in the latter.

The next step is to calculate the large-scale roughness length. This is derived combining the blending-height concept with the drag-partition theory. In accordance with Arya (1975), wakes behind downwind obstacles blend at z_b . Thus, for heights $z_a < z_b$, the flow is in equilibrium with the local surface, and can be parameterized with the local roughness lengths and local friction velocities. For heights $z_a > z_b$, on the other hand, wakes are considered not to be identifiable individually; thus, the flow just ‘feels’ the roughness of the surface (SC93). In that case, the wind profile is a function of a large-scale roughness length (\tilde{z}_0) and a large-scale friction velocity. The former is derived from

$$\ln(\tilde{z}_0/z_{0o}) = \ln(z_b/z_{0o}) \left[1 - (\tilde{\tau}_a/\tau_{so})^{-0.5} \right], \quad (3.5)$$

where z_{0o} is the local roughness length over the ice-free part, $\tilde{\tau}_a$ is the total wind drag over the heterogeneous area of sea ice, and τ_{so} is the local skin drag over the ice-free part. According to Arya (1975), the total wind drag $\tilde{\tau}_a$ is composed of the mean skin drag and the form drag. These drags depend on the surface roughness and the roughness elements, and thus on the ice (and snow) freeboard (h_f ; (3.2)), the lead size (L_o), the horizontal scale of roughness variations (\hat{L}), and even sheltering effects when ice floes lie close together. For our sea-ice cases, all assumptions regarding the drag have been

derived according to Hanssen-Bauer and Gjessing (1988) and Marshall (1971) (for details see SC93), and the roughness features just mentioned are taken into account. Since our sea-ice model does not include a measure for the amount of ridging, as opposed to e.g. Haapala et al. (2005), the roughness of pressure-ridge sails is not accounted for.

Once the large-scale roughness length is determined, the large-scale friction velocity \tilde{u}_* follows from

$$\tilde{u}_*^2 = \left[\frac{\kappa}{\ln(z_a/\tilde{z}_0)} |\vec{V}_a| \right]^2 \tilde{F} \quad (3.6)$$

with the large-scale stability function for momentum

$$\tilde{F} = \frac{\langle u_*^2 \rangle}{\left[\frac{\kappa}{\ln(z_a/\langle z_0 \rangle)} |\vec{V}_a| \right]^2} \quad (3.7)$$

and

$$\langle u_*^2 \rangle = N_i u_{*i}^2 + (1 - N_i) u_{*o}^2 \quad . \quad (3.8)$$

The actual modification of the wind stress follows equations (3.1) through (3.2), with u_{*i} being replaced by \tilde{u}_* , C_{di} by \tilde{C}_d (the large-scale drag coefficient), and $\tau_{ix,y}^{MFL}$ by $\tau_{ix,y}^{MFH}$.

The large-scale Richardson number, which only serves as a diagnostic to indicate the stability of the ASL, is derived from equation (2.1) by substituting F by \tilde{F} , and by substituting z_0 in c by $\langle z_0 \rangle$, and resolving for Ri .

The turbulent heat fluxes are in general not directly affected by the form drag, so they are estimated using the local roughness length (Claussen, 1992). Their calculation is identical to that in REF and MFL.

C. Results

Over Antarctic sea ice, the major impact of the strength of the momentum forcing over sea ice on dense-water formation is expected to occur in winter, when the ice concentration varies between 90% and 100%. In such conditions, small size coastal polynyas and leads can potentially affect the momentum flux over ice, and lead to positive feedbacks that can alter the open-water fraction. Therefore, the dynamic forcing of a sea-ice model should include a feedback that modifies the wind forcing as a function of the simulated (heterogeneous) surface conditions. This is how experiments MFL and MFH differ from REF, where MFL is designed as an intermediate step toward investigating the impact of surface heterogeneity on the momentum flux. In MFH, the effect of heterogeneity due to form drag and unstable stratification over adjacent ice-free parts is expected to increase the momentum forcing over sea ice in comparison to MFL. In the following, we will first concentrate on the differences between MFL and REF (section 3.C.1), and then on the differences between MFH and MFL (section 3.C.2). In section 3.C.3, the sensitivity of MFH to surface parameters that affect the form drag will be investigated.

1. MFL experiment

According to observations (e.g., Andreas et al., 2005), the wintertime atmospheric boundary layer over Southern Ocean sea ice is mostly statically stably stratified. For determining the strength of the momentum forcing, it is thus crucial to know the amount

of shear-driven turbulence. The criteria for its presence or absence is given in form of the gradient Richardson number (2.2), which is estimated as the ratio of buoyancy to shear forces.

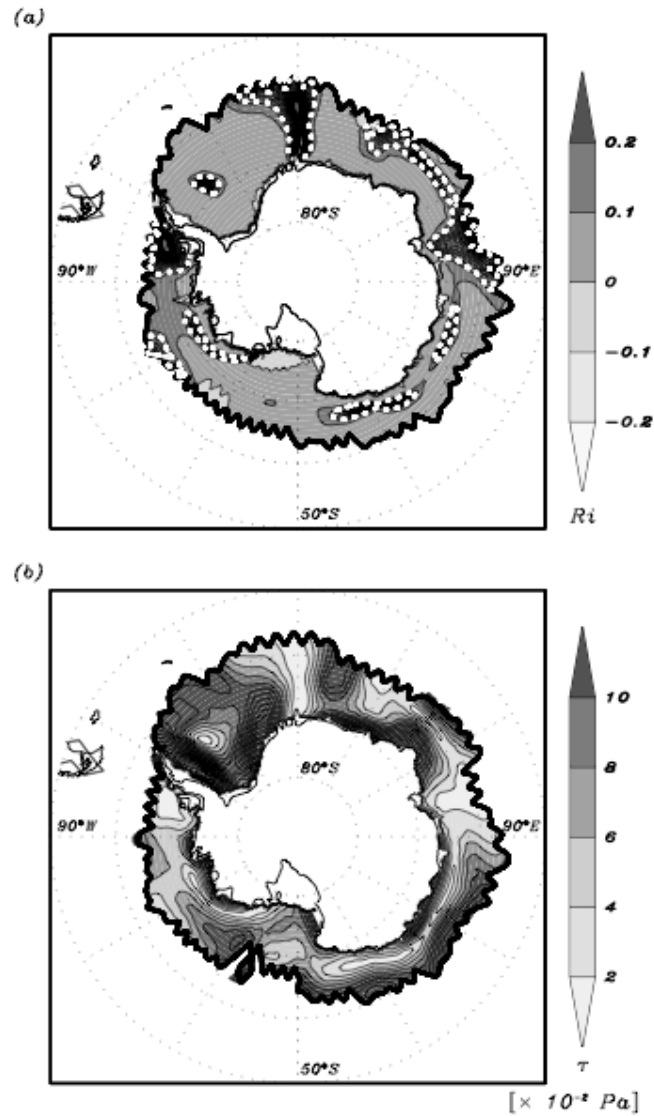


Fig. 3-1 Mid-winter snapshot of (a) local Richardson number over the ice-covered part, and (b) wind stress of REF. The thick black solid line represents the contour line of 20% ice concentration of the respective experiment. The white dashed line denotes the threshold toward dynamically stable stratification ($Ri = 0.25$). The isoline intervals are identical to the grey-scale intervals.

As a gravitational instability mechanism, the buoyancy force is dependent on the surface heat flux. The relatively warm water below sea ice significantly affects the surface temperature over thin ice, while over thick (or snow-covered) ice, cold surface temperature will prevail due to the low thermal conductivity of ice (and, in particular, that of snow). Therefore, ice (and snow) thickness has an inverse correlation with its surface temperature, and plays a decisive role in estimating the stratification over sea ice.

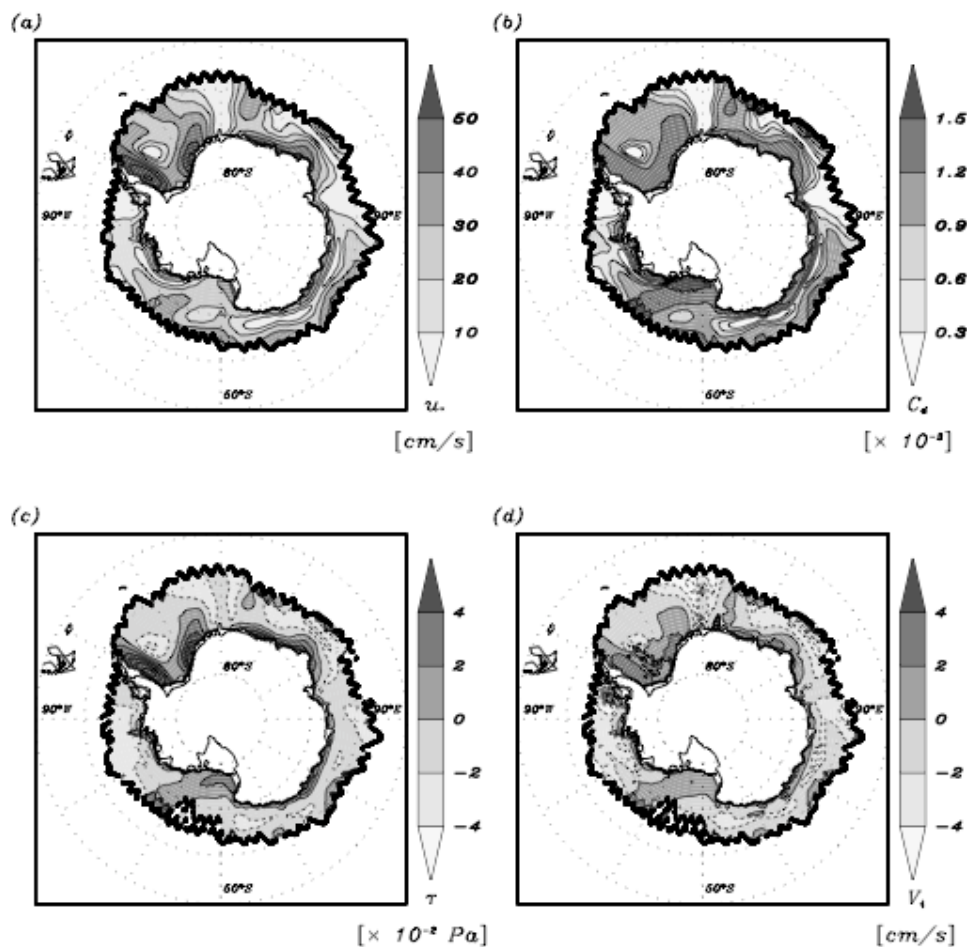


Fig. 3-2 Mid-winter snapshot of (a) local friction velocity of MFL, (b) local drag coefficient of MFL, (c) wind-stress difference MFL minus REF, and (d) sea-ice velocity difference MFL minus REF. The black solid line represents the contour line of 20% ice concentration of the respective experiments. The isoline intervals are identical to the grey-scale intervals.

Figure 3-1a shows a mid-winter snapshot of the local Richardson number over ice of experiment MFL, whereas Fig. 3-1b shows the original wind stress field for that date as used to drive sea ice dynamically in the reference experiment (REF). According to theoretical and laboratory studies, a necessary condition for dynamic instability in a statically stably stratified flow to occur is $0 < Ri < Ri_c = 0.25$.

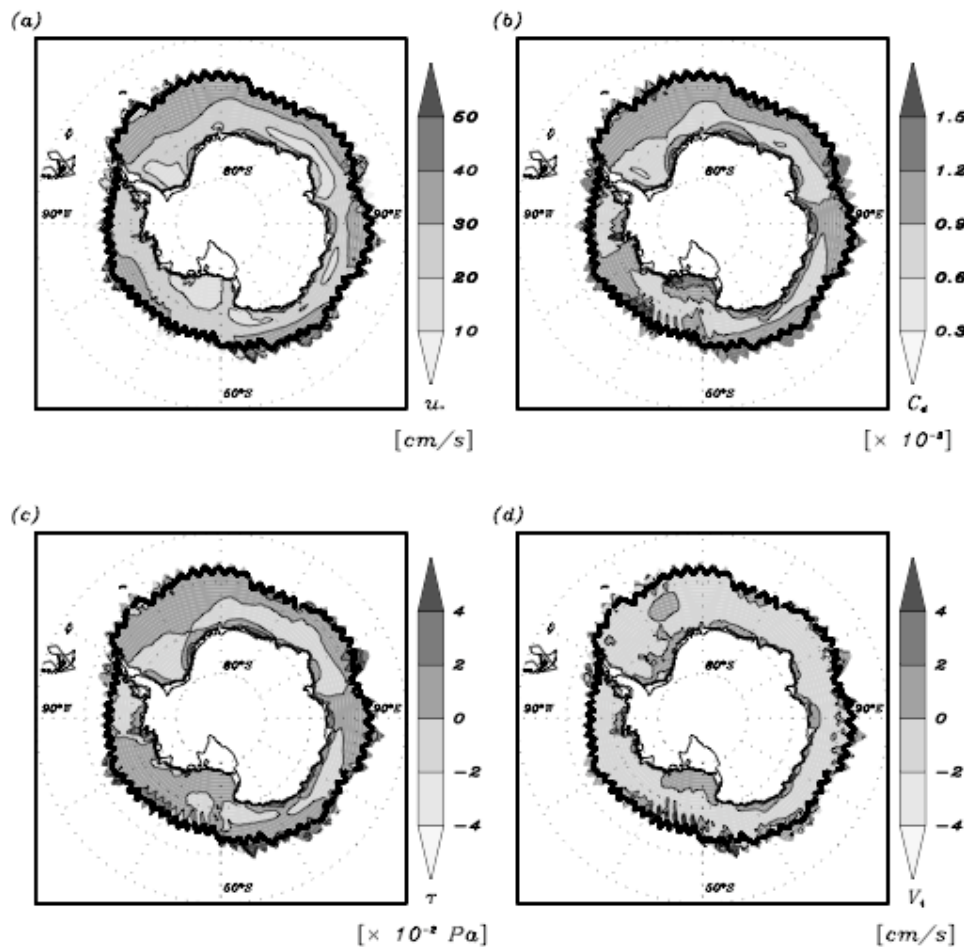


Fig. 3-3 Same as Fig. 3-2, but for winter mean rather than mid-winter snapshot.

When Ri is larger than the critical Richardson number Ri_c , turbulent flow turns into laminar flow, and the surface gets essentially decoupled from the atmosphere. Figure 3-

1a reveals that the ASL is statically stably stratified over most of the regions that contain sea ice with a concentration of at least 20%. Statically unstable regions occur only locally along parts of the coast- or ice-shelf line. About 20% of the area is dynamically stable and coincides with regions of near-zero wind stress (Fig. 3-1b). Enhanced vertical exchange between the surface and the lower atmosphere due to dynamic instability (shear-driven turbulence or background turbulence due to dynamic features such as gravity wave breaking) is thus prevailing.

In contrast to buoyancy, turbulence is generated by wind shear, causing turbulent exchange and mixing in the boundary layer. The associated momentum flux is a function of the friction velocity. Figure 3-2a shows that the friction velocity pattern is consistent with that of the Richardson number, i.e. 20% of the sea-ice surface is dynamically relatively decoupled from the atmosphere. On the other hand, the regions of large friction velocities are clearly correlated with those of large wind stress (Fig. 3-1b). The local drag coefficient (Fig. 3-2b) not only follows the pattern of the friction velocity, but also that of the Richardson number through the stronger impact of the stability function F_i where winds are weak. The modified wind stress is proportional to the original wind stress times the drag coefficient (Eqn. 3-2), its departure from the original wind stress (Fig. 3-2c) thus closely following both patterns. As a result, the original wind-stress pattern is mostly getting reinforced, i.e. where wind stresses were originally weak (strong) they become weaker (stronger) in MFL versus REF. The sea-ice velocity responds instantaneously in this predominantly divergent ice drift environment, its difference pattern (Fig. 3-2d) closely following that of the wind stress (Fig. 3-1b). The instantaneous patterns of all variables shown thus far move swiftly eastward following the synoptic wind field. Since

only the sea-ice component has high resolution (see section II.A), the coarse ocean grid pattern emerges where the upper-ocean temperature has a large impact on sea ice, such as along the ice edge (see Stössel et al., 2007).

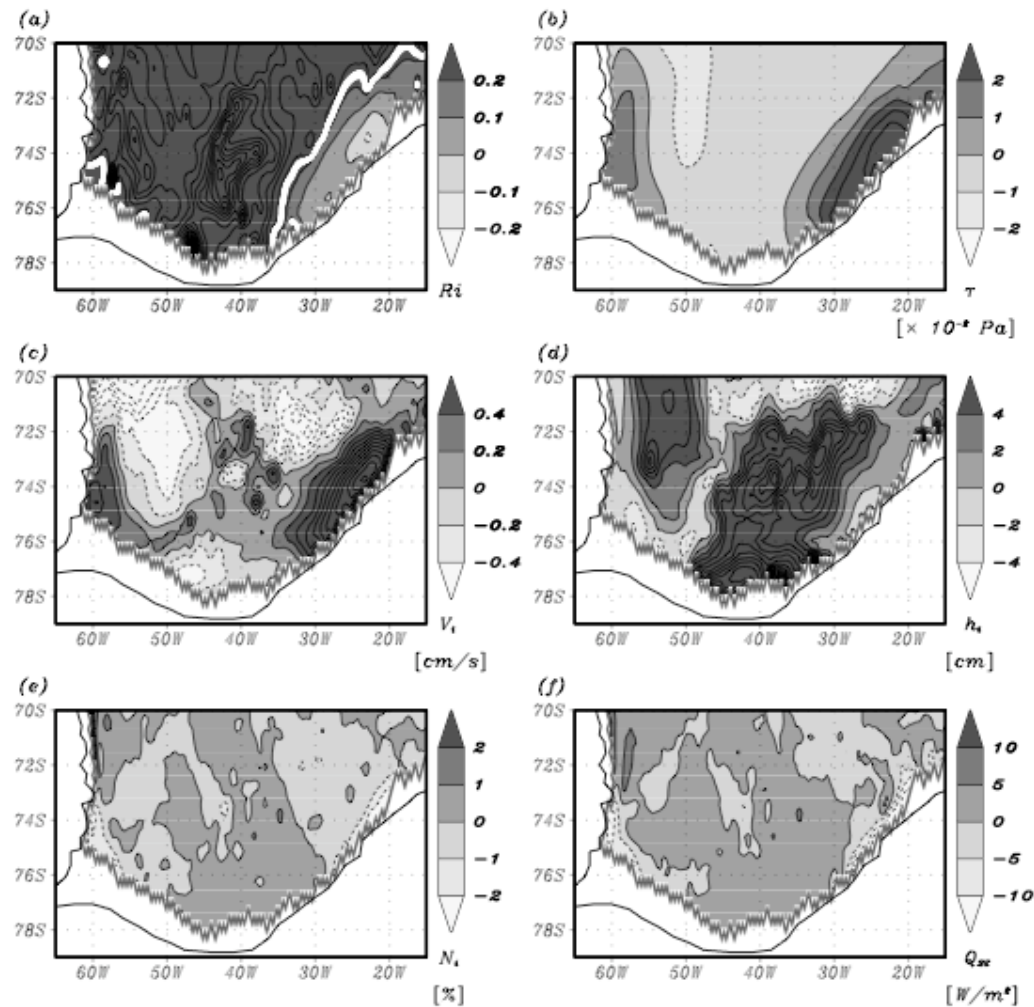


Fig. 3-4 Western Weddell Sea winter-mean of (a) local Richardson number. MFL minus REF differences of (b) wind stress, (c) ice velocity, (d) ice thickness, (e) ice concentration, and (f) sensible heat flux. The white line denotes the threshold toward dynamically stable stratification ($Ri=0.25$). The isoline intervals are identical to the grey-scale intervals.

The variables of Fig. 3-2 shown as winter (JAS) means (Fig 3-3) do not show much of a distinct pattern when plotted for the same isoline intervals as in Fig. 3-2. The most significant difference of wind stress between MFL and REF emerges along the coast of

East Antarctica. Differences along the ice edge are mostly due to shifts of the ice edge itself, and shall not be subject of discussion here.

A closer examination of the winter-mean differences, e.g. in the Weddell Sea (Fig. 3-4), illustrates the longer-term effects occurring due to the introduced change in the atmospheric feedback in MFL. First of all, it is interesting to note that when taking the winter mean of the Richardson number over the ice-covered part, i.e. Ri_i according to equation (2.2), most of the region emerges as being dynamically stably stratified (Fig. 3-4a). This follows from the highly nonlinear behavior of the Richardson number in that it becomes very large when winds are weak. Most regions being affected by weak winds at some stage while low- and high-pressure systems pass through the area, Ri_i averages out as dynamically stable. This is clearly meaningless, and emphasizes the importance of resolving air - ice interactions on the atmospheric synoptic time scale. A more meaningful feature in Fig. 3-4a, however, is the fact that certain regions along the coast remain dynamically unstable even in the winter mean, a clear indication for persistent strong winds, in this case strong katabatic winds between 30°W and 20°W, and somewhat weaker (barrier) winds along the Antarctic Peninsula along 60°W. This feature leads to a noticeable amplification of the wind stress over ice (Fig. 3-4b) in MFL. The change in magnitude of the ice velocity follows the change of wind stress fairly consistently (Fig. 3-4c). This difference between MFL and REF leads to substantial differences in the winter-mean ice-thickness distribution (Fig. 3-4d). In particular, where the coastal ice-velocity differences are largest, there is a reduction of ice thickness and concentration (Fig. 3-4e), while further west along the coast and further offshore, ice

thickness increases (up to 0.2 m). Where ice became less compact along the coast, the heat loss due to sensible heat flux increased up to 10 W/m^2 (Fig. 3-4f).

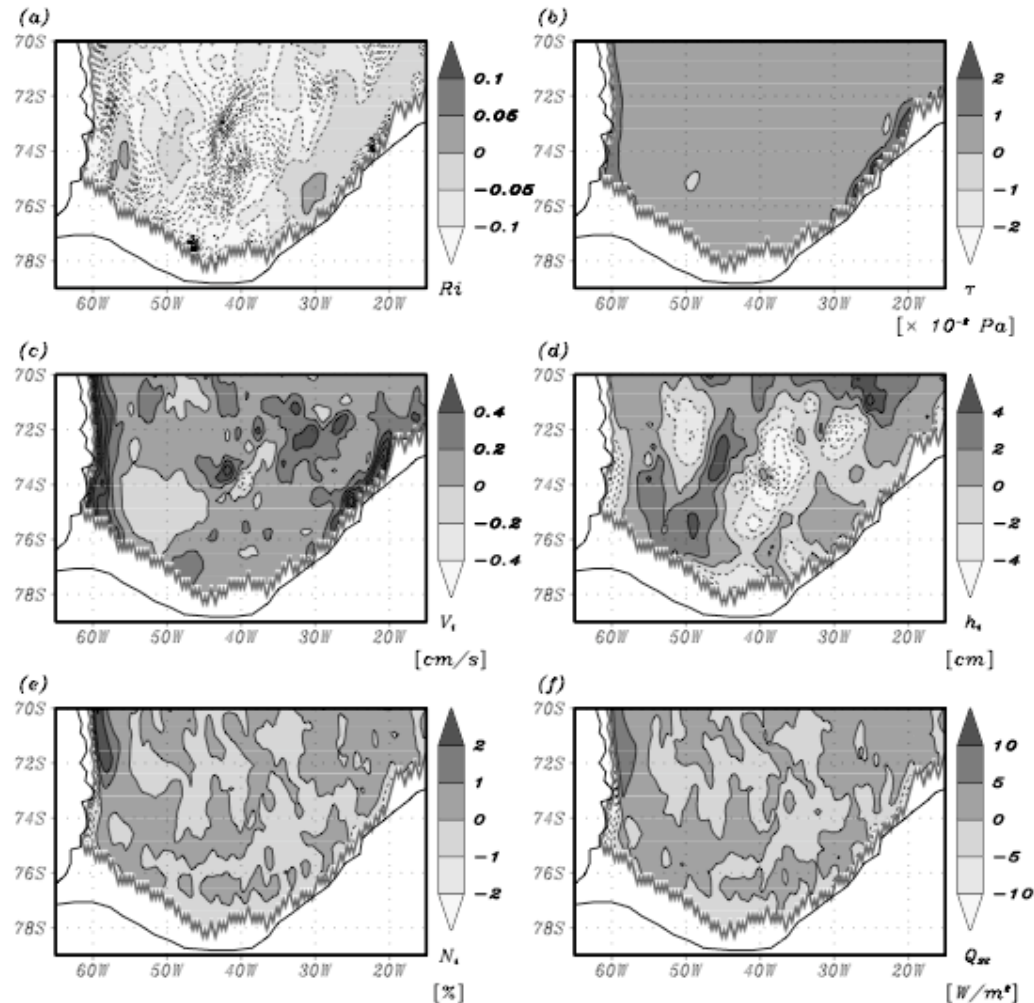


Fig. 3-5 Western Weddell Sea winter-mean MFH minus MFL differences of (a) Richardson number. Otherwise as Fig. 3-4. The isoline intervals are identical to the grey-scale intervals.

2. MFH experiment

Since experiment MFH considers the heterogeneous nature of the sea-ice cover, it is expected to yield weaker stratification than MFL, in particular due to the influence of the ice-free part, thereby enhancing the momentum flux. Comparing the instantaneous

spatial distribution of the large-scale Richardson number of MFH with the local one of MFL, we notice that the dynamically stratified regions have shrunk only slightly, so that the patterns of the variables shown in Fig. 3-2 and Fig. 3-3 for MFL are similar for MFH (and thus not shown). This suggests that under the prevailing, relatively high wintertime ice concentration, effects due to surface heterogeneities are generally negligible.

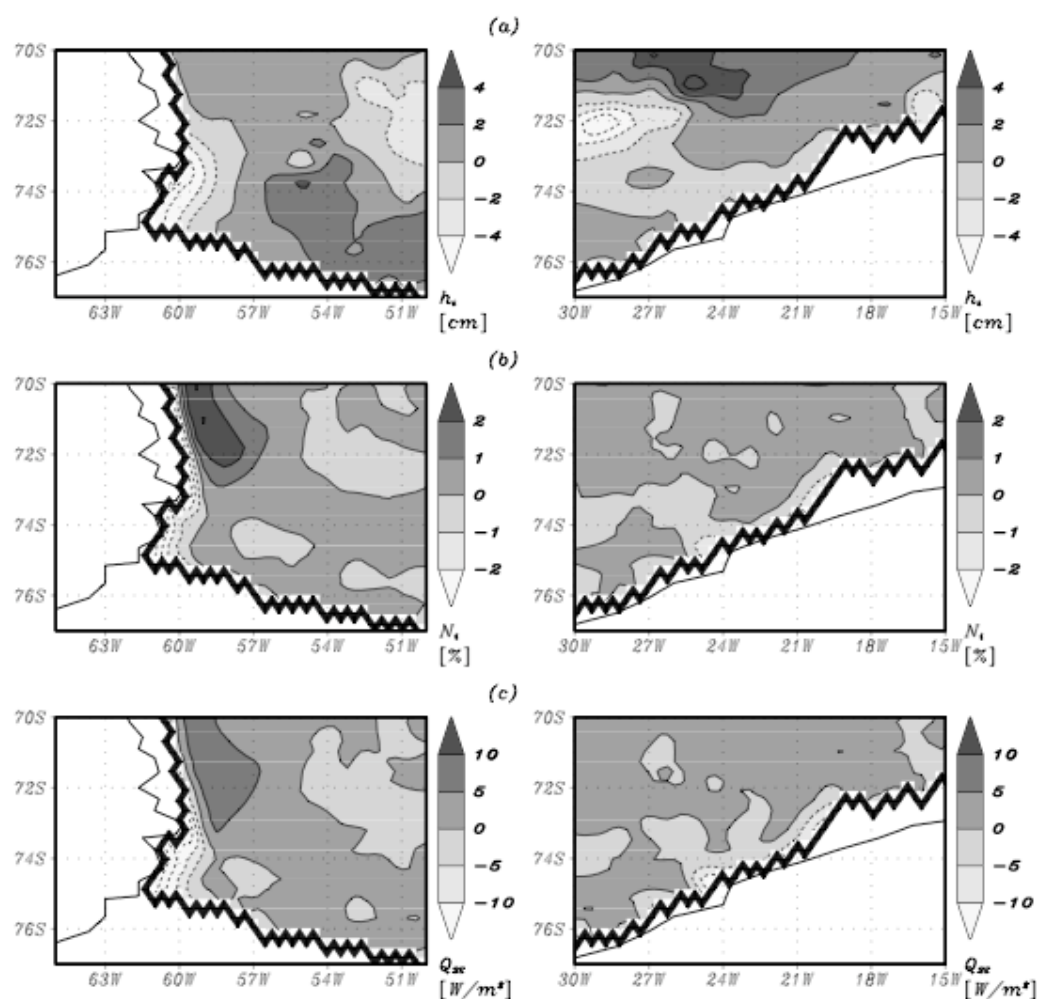


Fig. 3-6 Enlargement of the two critical coastal regions of Fig. 3-5d: (a) ice thickness, Fig. 3-5e: (b) ice concentration, and Fig. 3-5f: (c) sensible heat flux. Otherwise as Fig. 3-5d-5f.

Investigating the western Weddell Sea more thoroughly (commensurate with Fig. 3-4 for MFL versus REF), however, reveals an additional increase of the winter-mean wind stress in MFH versus MFL (Fig. 3-5b).

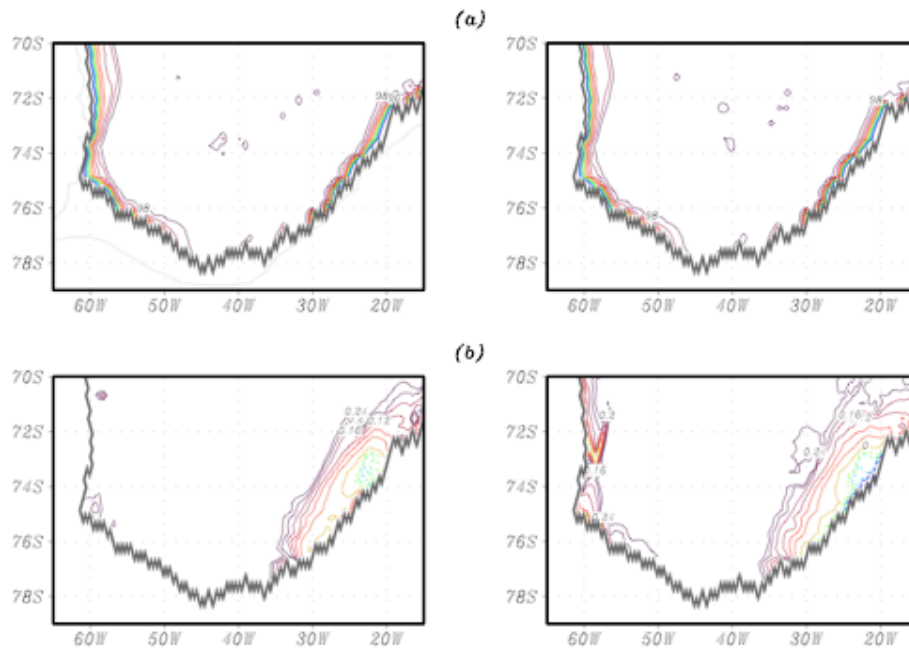


Fig. 3-7 Winter-mean of (a) ice concentration (isoline interval: 2%) and (b) Richardson number (isoline interval: 0.04×10^{-3}) of MFL (left) and MFH (right).

The large-scale Richardson number is everywhere reduced versus the local Richardson number (Fig. 3-5a), though with varying magnitude, closely following the absolute local Richardson number pattern (Fig. 3-4a). As in MFL versus REF, there is an additional pronounced increase of wind stress in the coastal regions between 35°W and 20°W, and along the Antarctic Peninsula in MFH versus MFL, though much more confined along the coast than in MFL versus REF. The ice velocity is consistently enhanced (Fig. 3-5c). A corresponding decrease of the coastal ice thickness (Fig. 3-5d), ice concentration (Fig. 3-5e), and downward sensible heat flux (Fig. 3-5f) can only be detected in an enlargement of the two critical coastal regions for these three variables (Fig. 3-6a ~ 6c).

In particular, since ice concentration has a direct impact on the momentum flux in MFH, one can conclude that this feedback enhances the momentum flux where the ice concentration is lower. The regions of lower winter-mean ice concentration are clearly visible in Fig. 3-7a. Except for most of the coastal region, the winter ice concentration is larger than 98%. This pattern is about the same in all three experiments. In terms of the Richardson number (Fig. 3-7b), however, the large-scale Richardson number of MFH shows a larger area of weaker stratification than the local Richardson number over ice of MFL. The associated enhanced wind stress in MFH is precisely the kind of effect to be captured by including the surface heterogeneity in the calculation of the momentum flux over sea ice.

3. MFH sensitivity experiments (MFHS)

The large-scale roughness length introduced in MFH is derived from estimating the total drag as a composite of surface skin drag of ice floes and leads, and form drag due to the obstacles to air flow, e.g. due to ice-floe edges. Together with the large-scale stability function, these factors play a decisive role in the modification of the momentum flux in MFH. One way to investigate the sensitivity of the momentum flux to the sea-ice surface conditions would be to change the oceanic conditions or the ice rheology to possibly change the response of the sea-ice pack to a modified momentum forcing, and vice versa. A more tractable way is to change the sea-ice boundary conditions as far as they affect the surface heterogeneity. Besides investigating the behavior of the sea-ice pack, these sensitivity experiments were also conducted to investigate the impact of the

momentum-flux parameterizations on the long-term deep-ocean properties of the global ocean GCM, realizing that compared to REF neither MFL nor MFH induced a noticeable change of these properties. For these purposes, the following four sensitivity experiments were conducted:

MFHS1: N_i in any of the equations of section 3c set to a maximum of 90%,

MFHS2: same as MFHS1, but N_i set to a maximum of 80%,

MFHS3: ice freeboard (Eqn. (7)) set to a minimum of 0.5 m,

MFHS4: MFHS1 + MFHS3.

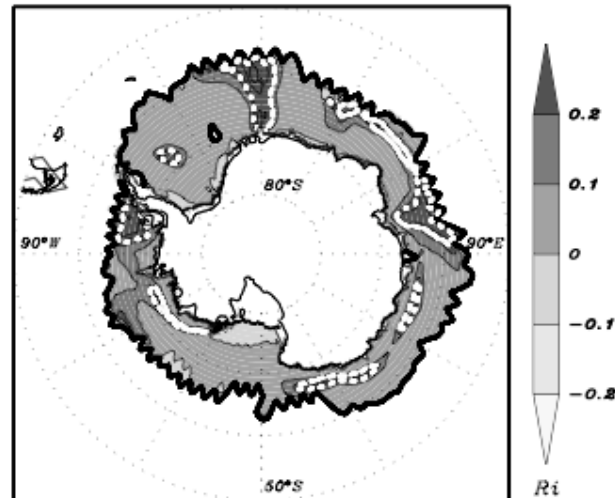


Fig. 3-8 Mid-winter snapshot of large-scale Richardson number of MFHS4. Otherwise as Fig. 3-1a.

The results of the first three experiments are not shown but summarized as follows. MFHS1 led to a noticeable increase of the wind stress over the interior ice pack, yet with relatively little change of ice thickness and ice concentration, and no significant change of the long-term deep-ocean properties. MFHS2 produced about the same result, suggesting that once the ice concentration is substantially lower than 100%, any further reduction doesn't make a big difference.

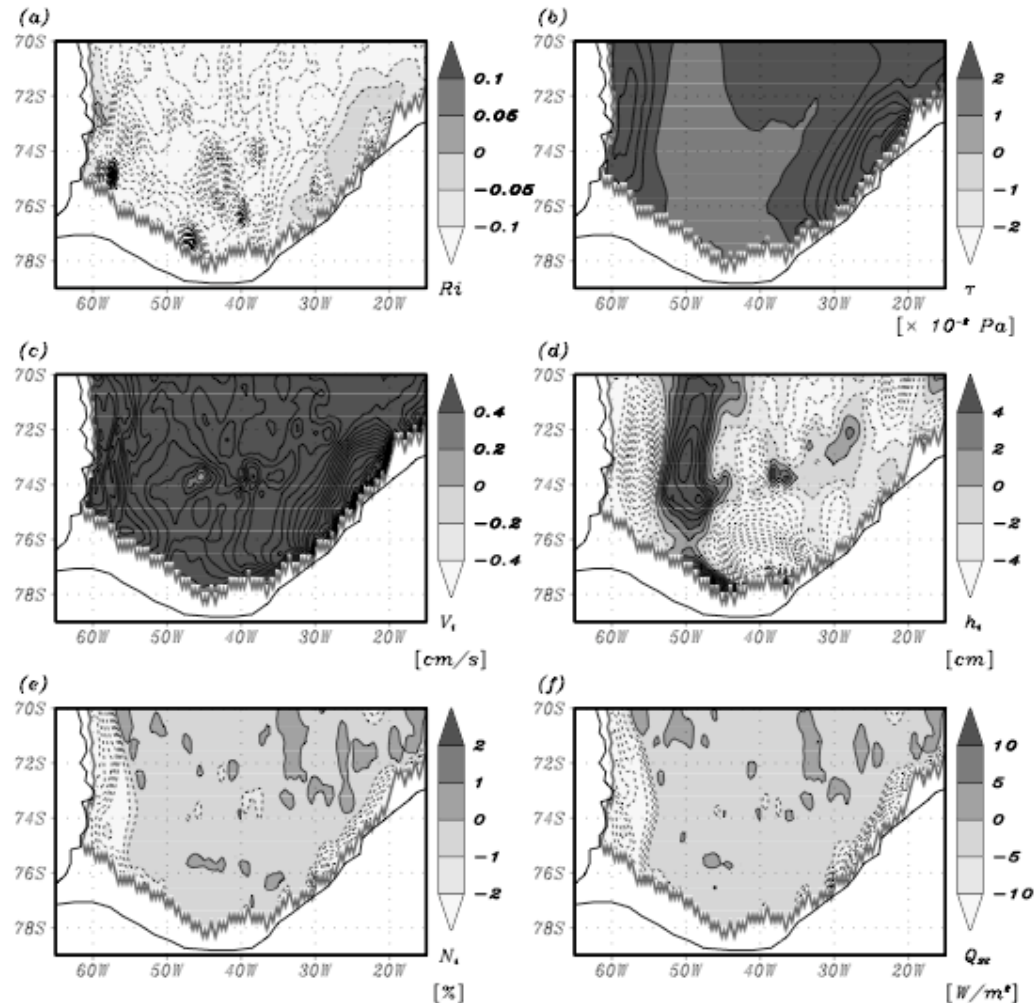


Fig. 3-9 Western Weddell Sea winter-mean MFHS4 minus MFH differences. Otherwise as Fig. 3-5.

The outcome of MFHS3 was not much different from MFH, suggesting that as long as the ice concentration is very high (98-100%), the ice freeboard is relatively unimportant (as one might expect). Combining a higher freeboard with a lower ice concentration (Exp. MFHS4) yielded the largest impact, results of which are discussed below.

A mid-winter snapshot of MFHS4 (Fig. 3-8) reveals a further shrinkage of the dynamically stably stratified area versus MFH (or, since the difference of MFH versus REF was very small, versus REF, i.e. Fig. 3-1a), an overall decrease of the stratification

in that area, and an increase of the statically unstable regions along the coast. Comparing Fig. 3-9 with Fig. 3-5, one finds a substantial additional increase of the wind stress (Fig. 3-9b) along the previously discussed coastal regions, overall consistent with a further reduction of the large-scale Richardson number (Fig. 3-9a).

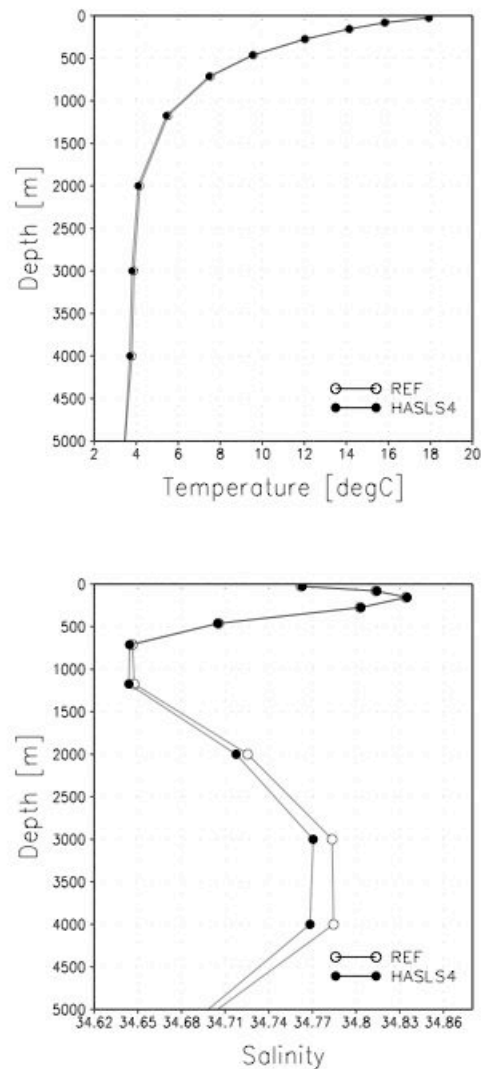


Fig. 3-10 Global and annual-mean profiles of potential temperature (upper panel), and (b) salinity (lower panel) of REF (lines with open circles) and of MFHS4 (lines with filled circles), at quasi equilibrium after 1000 years of model integration.

The winter-mean ice velocity (Fig. 3-9c) increases along these coastal regions (up to 2 cm/s), with a concomitant decrease in coastal ice concentration (Fig. 3-9e), and an

increase in sensible heat loss (Fig. 3-9f) of up to $50 W/m^2$. The substantially modified wind stress leads to a substantial change in the ice divergence field, and thus a considerable reorganization of the ice- thickness distribution (Fig. 3-9d).

Fig. 3-10 shows the annual- and global-mean profiles of temperature and salinity of REF, and those of MFHS4 after steady-state conditions have been reached (after 1000 years of model integration starting from REF). The profiles of MFHS4 show cooler and markedly fresher conditions in the deep ocean below 2000 m, which is a clear indication of more AABW formation and more AABW spreading in the world's ocean.

Corresponding model integrations of MFL, MFH, and MFHS1~3 did not reveal any noticeable differences to REF (and are thus not shown). This is just to indicate that under conditions of extreme sea-ice roughness the consideration of a sea-ice feedback on the momentum forcing can make a difference in the global volume of AABW. A more detailed investigation on the possible long-term, large-scale impacts under different model and wind forcing scenarios is underway.

D. Discussion and conclusions

This study was to investigate the response of the Southern Ocean sea-ice pack to an interactive momentum-flux forcing in the framework of a global ocean GCM. The way the momentum flux is modified by the simulated sea ice, particularly its sub-grid scale surface heterogeneity, follows the approach of SC93. Following Stössel et al. (2007), the Southern Ocean sea-ice component of the ocean model has a horizontal resolution of about 22 km, while the ocean model is coarse resolution (on the order of

200 km). This setup allows for detailed investigations of atmosphere – sea-ice – ocean interactions, in particular along the Antarctic coast- or ice-shelf line, which is critical for a realistic representation of coastal polynyas, thermodynamic sea-ice growth, and ultimately AABW formation. Simultaneously, this setup allows for the long-term response of the global thermohaline circulation to a possible change in the formation of AABW to be studied.

Three basic experiments have been considered: one in which the momentum flux driving sea ice is not affected by the simulated surface (i.e., sea-ice) conditions (REF), one in which it is only affected by the local, simulated subgrid-scale surface condition (MFL), and one in which it is also affected by the simulated surface heterogeneity (MFH). The momentum flux in MFH is thus modified by the simulated ice thickness and ice concentration, while in MFL it is only modified by the simulated ice thickness through its effect on the surface temperature. Though without impact on the momentum flux in REF, all experiments employ ASL physics based on similarity theory. MFH builds additionally on the concepts of flux aggregation and blending height (Claussen, 1995; Vihma, 1995). MFH has also undergone sensitivity experiments (MFHS), to investigate the impact of an enhanced form drag.

The model results demonstrated the importance of resolving air – ice interactions on the atmospheric synoptic scale. At any instant during winter, MFL yields predominantly statically stable but dynamically unstable ASL conditions. Dynamically stable regions emerge where the winds are weak. The spatial and temporal stratification pattern follows the synoptic wind forcing. Persistent differences between MFL and REF occur along the Antarctic coastline. In MFL, the latter domain is characterized by a

positive feedback, in which coastal polynyas tend to weaken the stratification, enhance the momentum flux and thus the ice velocity, lead to regional divergences and convergences, with corresponding substantial regional changes of ice concentration and thickness. Commensurate with what is derived from observations (e.g., Markus et al., 1998; Renfrew et al., 2002), the winter-mean heat loss due to sensible heat flux over coastal polynyas reaches up to 400 W/m^2 in our simulations. The maximum sensible heat loss increase in MFL, however, is only 10 W/m^2 . It has no noticeable effect on the rate of AABW formation, and thus the long-term global deep-ocean properties.

Although the momentum flux is overall somewhat higher in MFH than in MFL, there is no significant difference between the two except for coastal regions that have lower ice concentration in association with coastal polynyas. There, the wintertime ASL is regionally also statically unstable. Since the simulated ice concentration has a direct impact on the momentum flux in MFH, as opposed to MFL, this situation yields a locally reinforced positive feedback between ice concentration and momentum flux. The difference between MFH and MFL, however, is overall smaller than between MFL and REF, suggesting that the simulated high wintertime ice concentration, and the form drag specifications described in section 3c (ice freeboard, horizontal scale of roughness variations, etc.) do only lead to local discrepancies, namely along the coast where the ice concentration is markedly lower. In terms of global deep-ocean properties, there is again no noticeable change.

A slight cooling and substantial freshening of the global deep-water masses are obtained when the maximum ice concentration affecting form drag is reduced and the ice freeboard simultaneously increased (MFHS4). Only one of these modifications at a time

does not cause a noticeable change in the deep-ocean properties. This is understandable, since a higher ice freeboard will not have any effect if the ice concentration is 100%, while the effect of a lower ice concentration itself does not seem to enhance the form drag when sea ice is relatively thin, as observed over most of the Southern Ocean sea-ice pack (e.g., Harms et al., 2001) and as simulated here. The question of whether a heterogeneous ASL parameterization causes long-term changes in the deep ocean thus seems to narrow down to the question which of the form-drag assumptions, those of MFH or MFHS4 are more realistic. Depending on which satellite passive microwave algorithm to believe (e.g., Markus and Cavalieri, 2000), our simulations lie in the highest range (Stössel et al., 2007), implying that a somewhat lower (3-6%) ice concentration than simulated may be more realistic. While a minimum ice freeboard of 0.5 m is too high for typical Southern Ocean sea ice, it could be justified due to the fact that we did not account for the form drag due to pressure ridges and sastrugi. Pressure ridges of 1 m and higher are very common in Southern Ocean sea ice (e.g., Dierking, 1995), especially in the southernmost regions where MFHS4 differs most from MFH. According to detailed measurements in the Weddell Sea by Andreas and Claffey (1995), the sastrugi effect on the form drag can even be larger than that of pressure ridges. The simplest way of representing such contributions in an ice model that only simulates ice (and snow) thickness and concentration is to increase the ice freeboard. Furthermore, our assumption of the snow depth being 10 cm (see section II.A) is in the lowest range of what is locally observed (e.g., Massom et al., 2001), or satellite-derived (e.g., Powell et al., 2005). Accordingly, we do not think that the total form drag is overestimated in MFHS4. The sensible heat loss over coastal polynyas in MFHS4 reaching about 15% higher than REF

rather than 2~5% as in MFL and MFH, seems to pass a threshold beyond which the AABW formation rate is getting significantly affected.

While there are a series of open questions that need to be addressed in more detailed investigations, a comparison with estimates of surface and ASL parameters retrieved from airborne or local in-situ measurements over sea ice (Andreas and Claffey, 1995; Andreas et al., 2005; Dierking, 1995; Uotila et al., 2000) reveals that the stratification and momentum flux of experiment MFHS4 delivers the most reasonable figures of all experiments. The spatial and temporal pattern, however, is highly variable, making a direct comparison rather difficult. Therefore, a more thorough analysis of how the simulated ASL parameters compare with the available observations under various wind and surface-property conditions is still in need. It should be noted that the parameterized effects of surface heterogeneity are different from the viewpoints of atmosphere, ocean, and sea ice. From the viewpoint of the ocean and atmosphere the grid-averaged surface fluxes are (for the ocean) or would be (for the atmosphere, which is not simulated in the present model) affected by surface heterogeneity already in REF and MFL because of the separate treatment of the ice-covered and ice-free parts of a grid cell, but from the viewpoint of sea ice, which is only affected by the fluxes over the ice-covered part, only MFH takes into account the effects of heterogeneity on the momentum flux.

Another related issue, which is beyond the scope of the current study, is the correspondence to the oceanic boundary layer (OBL) in heterogeneous sea ice. The processes are similar in the sense that freezing in leads and polynyas implies brine rejection, which destabilizes the OBL, thus increasing turbulent mixing (e.g., McPhee

and Stanton, 1996), and therefore the ice–ocean drag. Furthermore, ridge keels enhance the ice–ocean drag proportionately more than ridge sails do the ice–atmosphere drag, because of the reduced scales in the OBL (comment from anonymous reviewer). In the simulations presented here, the ice-ocean drag has been kept constant, i.e. does not change with ocean stratification, with ice-ocean form drag, or with ice concentration. In particular, the ice-ocean drag coefficient is 0.0055 following e.g., Hibler (1979). According to Leppäranta (2005), such relative high drag coefficient is more suitable for multiyear Arctic sea ice than for the generally thinner and smoother Antarctic sea ice, where ice-ocean drag coefficients as low as 0.0016 have been derived from measurements (Martinson and Wamser, 1990). Furthermore, Leppäranta (2005) suggests that the ratio of the air-ice and ice-ocean drag coefficient should remain relative constant, since “the geometries of top and bottom ice surfaces are well correlated”. Keeping the ice-ocean drag coefficient constant, but varying the air-ice drag coefficient as a function of the ASL stratification and the heterogeneity of the sea-ice pack, ignores this suggestion completely. On the other hand, the constant ratio issue is probably not valid on the daily time scale and in conjunction with stratification, since an oceanic instability will not necessarily occur at the same time and location as an atmospheric instability, due to different preconditioning, among others. One could also argue that in contrast to the interface between sea ice and the atmosphere, that between sea ice and the ocean is interactively coupled in our model. However, there is no mechanism included that allows for changes of the ice–ocean drag due to (subgrid-scale) processes of the kind mentioned above. Except that the momentum transfer between ice and ocean depends, besides on the upper-ocean current, also on the sea-ice velocity (which is generally negligible for the

momentum transfer between ice and air), the fact that the sea-ice (model) is coupled to the ocean (model) does in this regard not differ from an uncoupled model. Responses of global sea-ice – ocean GCMs to processes that might change the ice – ocean drag in addition to such affecting the ice – air drag certainly merit additional research.

This study showed that including atmospheric feedback over heterogeneous sea ice in a sea-ice – ocean GCM is worth pursuing. With an adaptation of the form drag toward more commonly observed sea-ice conditions in the Southern Ocean, the model produces a noticeable impact on the long-term global deep-ocean. Even though the atmospheric variables at the top of the ASL are prescribed, what counts for the ocean and the sea ice are the fluxes, which themselves are highly dependent on the (simulated) surface conditions. The current setup is an alternative and a much more economic approach toward understanding the feedbacks between the deep ocean, sea ice, and the high-latitude atmospheric boundary layer than experiments with a coupled atmosphere - sea-ice - ocean GCM.

CHAPTER IV

RESPONSE OF SOUTHERN HEMISPHERE OVERTURNING TO THE INTERACTIVE MOMENTUM FLUX OVER SEA ICE AND ITS IMPACT ON THE GLOBAL OCEAN CIRCULATION

A. Introduction

In the previous chapter, the fraction of leads and polynyas within SO sea ice appeared to increase when the momentum flux between the atmosphere and the sea ice is allowed to vary instantaneously in response to the simulated sea-ice conditions. The application of the IMF resulted in an increase of the ocean-to-atmosphere heat loss, brine rejection due to new ice formation, and thus the formation rate of dense water, in particular along the coastline, which finally led to an increased amount of AABW formation. While chapter III was devoted to the impact of the IMF on SO sea ice, this chapter aims at an investigation of the long-term global-scale oceanic response to the application of the IMF. In particular, how the climatic perturbation originated from the IMF-induced changes exerts an influence on the transport of the ACC (a standard diagnostic of the SO circulation) via an anomalous baroclinic transport is a major issue in this chapter. That is, while the earlier study was to focus on investigating the regional response of sea ice to the IMF and its linked change in AABW, the focus of this study is to investigate the long-term oceanic response to the signal originating from the change of

SO sea ice. Its current application includes the aforementioned pragmatic method of raising the form drag, as has been justified in the previous chapter.

Along the northern edge of the pack ice, the persistent SWWs give rise to shear-driven turbulence, which acts to keep the ASL condition of the region dynamically unstable. This differs from the coastal region where the ASL is statically and dynamically unstable due to buoyancy-driven turbulence. The application of the IMF thus gives also rise to a strengthening of the wind stress over the northern ice regions. The changes of wind stress associated with the IMF in these two regimes can be connected to two types of polynyas, i.e. coastal polynya and open-ocean polynya, each of which possibly giving rise to near-boundary convection and open-ocean convection, respectively.

A coastal polynya, classified as a latent heat polynya (Smith et al. 1990), around Antarctica is maintained by strong persistent katabatic winds. During the austral winter, the katabatic winds constantly push sea ice away from the Antarctic continent rendering the ocean ice-free, i.e. creating coastal polynyas, exposing relatively warm ocean surface waters (-1.8°C) to extremely cold air (typically -30°C). There and then, the surface waters rapidly lose heat to the atmosphere and freeze, resulting in new ice formation such as frazil ice (Cotton and Michael 1994; Wadhams 2000). The winds constantly blow the newly formed sea ice off shore, leading to an equilibrium width of the wind-driven coastal polynya. Both the brine rejection via new-ice formation and the cooling of the surface water via heat loss are responsible for dense water formation, which acts to destabilize the water column and to trigger mixing of very cold and saline shelf water with the relatively warm and more saline Circumpolar Deep Water (CDW) along the continental slope. This process is referred to as ‘near-boundary convection’ (Killworth

1983). Therefore, the presence of coastal polynyas at certain well-defined sites around Antarctica has a direct impact on AABW formation.

An open-ocean polynya is classified as a sensible heat polynya (Smith et al. 1990), and is potentially also an important contributor to ocean ventilation and deep-water formation. While it is not clear whether the preconditioning mechanism is provided by atmospheric, oceanic, or ocean bottom topography conditions, the upwelling of warm water, which may cause sea-ice melting, plays a major role in maintaining open-ocean convection. Some studies, using numerical models, demonstrated that a wind-driven ice divergence plays a more decisive role in triggering the polynya opening than a strong local oceanic upwelling (Goosse and Fichefet 2001; Bailey et al. 2004). Moreover, the Weddell Sea polynya that occurred in the 1970s is thought to have contributed to AABW formation through open-ocean deep convection (Gordon 1982). Therefore, enhanced divergence in the wind field associated with the application of the IMF is expected to raise the possibility for initiating and sustaining open-ocean polynyas and associated open-ocean convection, ultimately leading to a change in the long-term global deep-water properties.

To investigate the robustness of the IMF impact, three different experimental frameworks were selected, all of which have the same sea-ice model, but differ in the way the ocean affects sea ice. In the first experiment (EXPA), following the experimental setup of the previous chapter, a higher vertical eddy diffusion in the SO acts to diminish the preconditioning for convection, so the oceanic impact of the IMF on sea ice is getting less perturbed by oceanic heat flux associated with convection. In the second experiment (EXPB), we removed the oceanic condition of constraining convection. In this

experiment, the effects of open-ocean polynyas and the associated freshwater flux (from melting sea ice) are thus by design most pronounced. In the third experiment (EXPC), the SO upper-layer ocean temperature is constrained by satellite-derived passive-microwave sea-ice concentration (Stössel, 2008), and therefore the sea-ice evolution thermodynamically independent of oceanic heat flux due to convection. This experiment makes it possible to eliminate the effect of the IMF on convection, while maintaining the most realistic sea ice cover.

A detailed description of the experimental setup follows in section B. Section C describes the reference experiments of the three experimental frameworks just mentioned. The long-term changes of the thermohaline circulation due to the IMF and their impact on the ACC are discussed in section D. A summary and conclusions are provided in section E.

Table 4-1. The hierarchy of model experiments (See main text for details)

	Interactive Momentum Flux (IMF)	Increased Vertical Diffusion ($10 \times K_v$)	Constrained Upper Ocean Temperature
AREF	·	√	·
AIMF	√	·	·
BREF	·	·	·
BIMF	√	·	·
CREF	·	·	√
CIMF	√	·	·

B. Description of experiments

Whereas chapter III was mostly concerned with the regional sea-ice response to the IMF, the present study is to investigate the oceanic responses in three different

settings. Control variables of the global thermohaline circulation, such as the magnitude of northward AABW intrusion, NADW outflow and the ACC, will be a major focus. The experiments discussed in this study are listed in Table 4-1.

In this study, the IMF version with enhanced form drag is used (experiment MFHS4: refer to section III.C.3), which was identified to reflect the most reasonable assumption given that the form drag due to pressure ridges is not explicitly accounted for. The experimental framework EXPA is identical to experiment MFHS4, except that glacial melt water due to melting under the pseudo ice shelves (see Stössel et al., 2007) has been excluded in all experiments discussed in this chapter. EXPA thus features a vertical eddy diffusivity that is increased by one order of magnitude from $0.8 \times 10^{-4} \text{ m/s}^2$ in the SO south of 50°S , which reduces the preconditioning for open-ocean convection (Stössel et al., 2007). Therefore, the enhanced dense-water formation due to the IMF is less perturbed by (mostly excessive) open-ocean convection. Whether the model allows for strong convection in the SO or not makes a large difference for the steady state properties and circulation of the ocean model, and may thus alter the response to the IMF. The experimental framework EXPB is free of the constraint to suppress oceanic convection. Open-ocean convection brings a large amount of heat to the upper ocean to give rise to sea-ice melt, and ultimately the formation of open-ocean polynyas. The freshwater flux associated with this melting tends to re-stratify the water column, while the buoyancy flux due to the heat loss through the polynyas has a destabilizing effect. The balance between the freshwater flux due to ice melting and heat loss gives rise to open-ocean polynyas in several stages (Goosse and Fichefet, 2001). To isolate the effect of convection from the multitude of feedbacks associated with the freshwater flux,

experimental framework EXPC does not allow oceanic heat to affect sea ice by means of constraining the upper ocean layer temperature to closely follow the satellite-derived sea-ice concentration (Stössel, 2008). The uppermost ocean temperature is designed to adopt the freezing point where and when the satellite-derived sea-ice concentration is 100%, and to increase linearly the influence of the simulated upper-ocean temperature with increasing satellite-derived lead fraction.

All results reflect near-equilibrium conditions after model integrations on the order of 1000 years. Each experimental framework yielding noticeably different equilibrium states helps assessing the robustness of the long-term oceanic response to the IMF over SO sea ice. In cases where experiments show noticeable inter-annual and inter-decadal internal variability, such has been removed by means of multi-year averaging.

Table 4-2. Equilibrium values of selected integrated quantities in respective reference and IMF applied case (NA overturning [Sv]: Maximum transport; NADW outflow [Sv]: NADW outflow across 30°S; ACC [Sv]: Drake Passage throughflow; $\theta_{z=4000m}$: global-mean potential temperature at 4000m depth; $S_{z=4000m}$: global-mean salinity at 4000m depth)

	AREF	AIMF	BREF	BIMF	CREF	CIMF
$\theta_{z=4000m}$ [$^{\circ}C$]	2.35	2.20	0.97	0.90	0.54	0.48
$S_{z=4000m}$ [psu]	34.635	34.622	34.678	34.678	34.776	34.778
NA overturning	38.1	37.9	28.6	28.1	23.3	22.2
NADW outflow	27.1	26.5	12.3	12.6	8.3	7.8
ACC	88.2	94.4	99.9	102.7	111.3	114.0

C. Results of reference experiments

The main results of the respective reference experiments are discussed here since they will constitute the starting point for each of the sensitivity experiments. Selected

integrated key variables of the thermohaline circulation are shown in Table 4-2. The by far strongest NA overturning and outflow of the NADW are simulated in AREF. The intensification of the overturning circulation with increased vertical diffusion in EXPA is consistent with earlier studies that investigated the effects of enhanced vertical mixing rates (Schmittner and Weaver 2001; Sijp and England 2006). EXPA shows a relatively large volume of AABW compared to other experiments. Of all reference experiments, EXPA yields also the weakest Drake Passage throughflow (ACC), which is attributed to the relative weak convective potential energy release, which in turn leads to overall less dense water south of the ACC, and thus a reduction of the meridional density gradient across the ACC (Stössel, 2008). To the contrary, CREF shows the largest ACC transport, owing to the most intense convection. The Antarctic sea-ice volume is largest in CREF because sea ice is not being affected by oceanic heat flux arising from convection. There is thus no negative feedback that would prevent thermodynamic ice growth other than ice thickness itself. The extreme differences between AREF and CREF are also reflected in the long-term global-mean deep-ocean properties, the almost 2°C colder temperature in CREF indicating much stronger AABW formation in CREF than in AREF. Experiment BREF lies roughly in between AREF and CREF in all control variables examined so far, and is in terms of deep-ocean temperature and NADW outflow closest to the observed estimates (1.08°C according to Levitus (1982) and 17 Sv according to Ganachaud and Wunch (2000), respectively). The increase in global-mean deep-ocean salinity from AREF via BREF to CREF indicates that the fraction of open-ocean convection is increasing versus that due to near-boundary convection (see next section), and/or that more of the relatively salty CDW is getting entrained into AABW, and/or that CDW

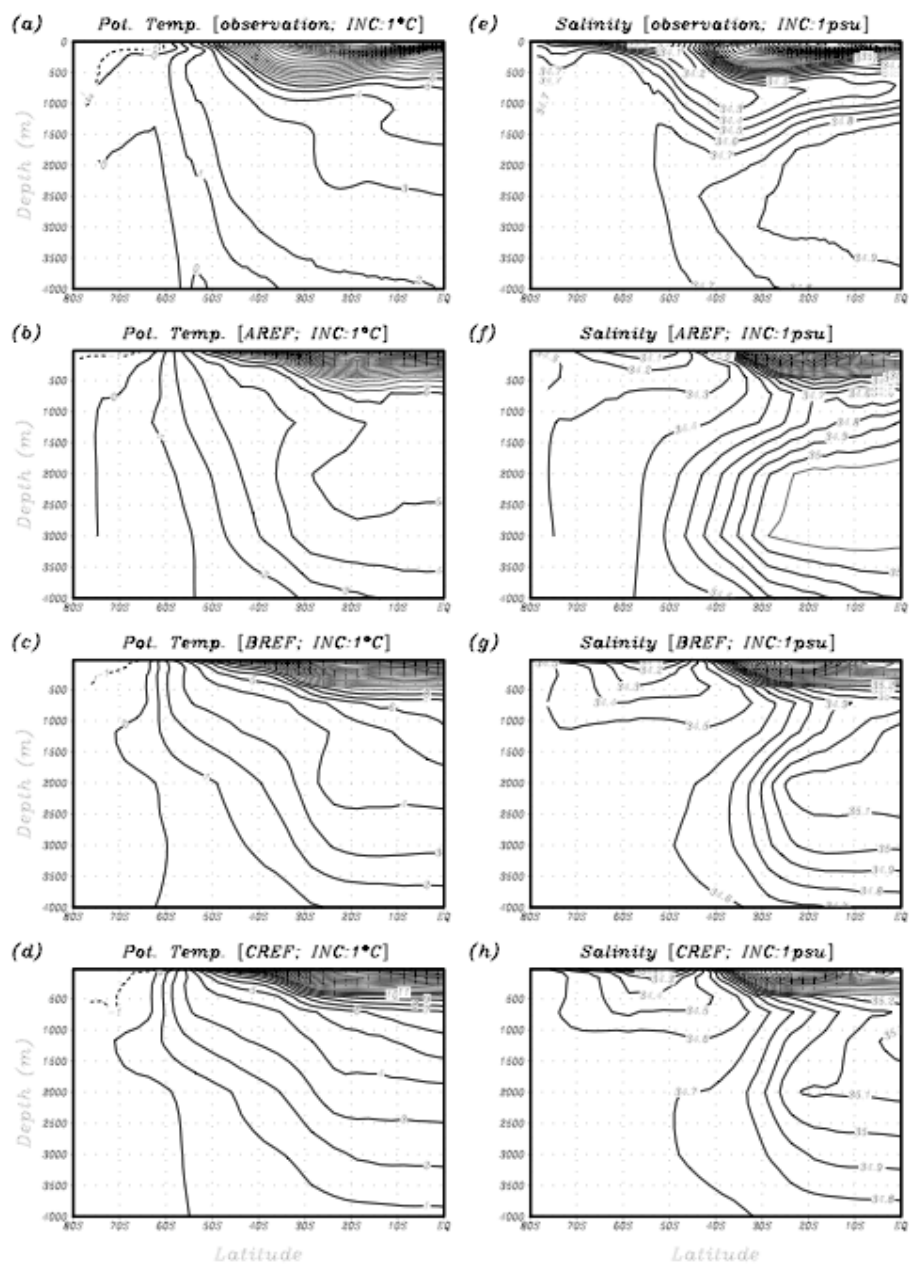


Fig. 4-1 Meridional sections of potential temperature and salinity fields in the south Atlantic Ocean.

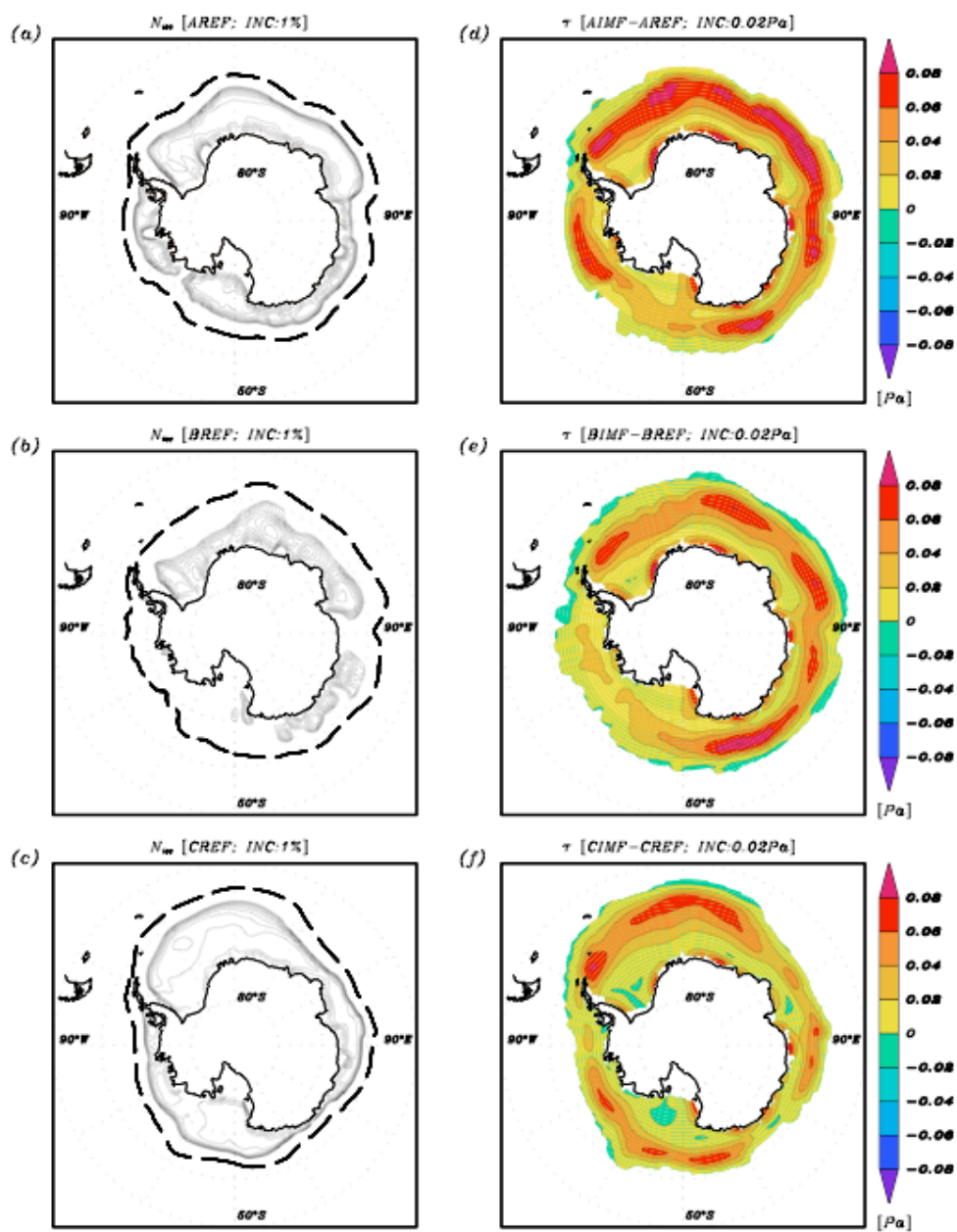


Fig. 4-2 Winter-mean ice concentrations and differences of wind stress over the SO sea ice.

itself becomes saltier. The largest volume of sea ice is simulated in EXPC because its upper-ocean temperature is constrained by the satellite-derived ice concentration, and therefore its sea ice is free from the influence of simulated oceanic heat flux.

Fig 4-1 shows meridional sections of annual-mean potential temperature and salinity in the Atlantic Ocean averaged from 10°W to 60°W for observed data (Locarnini et al. 2006; Antonov et al. 2006) and for the three reference simulations. Compared to the observational estimates, all reference experiments reflect a weak but noticeable northward intrusion of AAIW as well as a strong southward intrusion of NADW. Among the experiments, AREF shows the strongest intrusion of NADW as derived from its salinity pattern (Fig 4-1(f)), consistent with its NADW outflow being the strongest of all experiments (Table 4-2). In the SO south of 50°S, the salinity of AREF is nevertheless the lowest of all experiments, which is attributed to the higher vertical eddy diffusion in that region in AREF, i.e. fresh surface water spreads more effectively down the water column in AREF than in BREF or CREF. While CREF has the weakest NADW outflow, its SO salinity is largest. This arises from the surface salinity being larger because of the fact that there is essentially no sea-ice melt due to oceanic heat flux when satellite-derived sea-ice concentration is high (see section IV.B). The weak NADW outflow in CREF, in turn, is due to AABW occupying a larger part of the water column, as is indicated by the coldest deep ocean of all experiments. Only AREF with its strong NADW outflow reflects a condition where 0°C water manages to reach the Antarctic continental margin, as observed. Of all experiments, also the northward intrusion of AAIW is most pronounced and realistic in AREF. As mentioned in section IV.B, this experiment also features the most realistic sea-ice cover without upper-ocean temperature

constraint, indicating that a decent amount of oceanic heat flux that allows for just enough ice melt to maintain a relatively compact sea-ice cover (see Stössel et al., 2007) may be critical for a realistic simulation of AAIW.

Figs 4-2a-c show distributions of winter-mean (July – September) ice concentration between 90% and 100% with 1% isoline increment and location of the ice edge defined along 20% ice concentration. Variations in the uppermost range of ice concentration are most critical for the heat flux between atmosphere and ocean, i.e. a change from 99% to 95% has a much larger impact than a change from 79% to 75%, where the 79% case is already highly transparent in terms of heat flux. In terms of a transition from a stable to an unstable ASL condition over sea ice, such is also more likely in the first case than in the latter case. Figs 4-2a and 2b show large-scale coastal polynyas of the size of the coarse ocean model grid which are due to the fact that the variables shown (in this case ice concentration) are plotted on the fine grid, i.e. these patterns would not show up if plotted on the coarse grid. While appearing unrealistically artificial, coarse-grid features within the fine grid sea ice readily indicate where the oceanic influence dominates. EXPC shows no such pattern, because the assimilated upper-ocean temperature follows the fine-grid satellite data, and does not allow for coarse-grid convection to strongly affect the ice cover where the satellite-derived ice concentration is high (see Stössel, 2008).

Figs 4-2a-c reveal that the three reference experiments are very different in the way they simulate compact sea ice. CREF clearly delivers the most realistic ice concentration, as already found in Stössel (2008), followed by AREF, as found in Stössel et al. (2007). BREF suffers from excessive localized oceanic convection associated with

excessive localized ice melt. In spite of these differences all experiments feature coastal polynyas and wide ice edges that emerge as low ice concentration and low grid-cell mean ice thickness (not shown). Such initial boundary conditions tend to destabilize the ASL, the application of the IMF thus acting to enhance the atmospheric momentum forcing of sea ice in those regions. This is indicated in Figs 4-2d-f, which shows the difference of surface wind stress between the IMF experiments and the respective reference experiments. While overall enhanced, there is clearly a tendency for the wind stress to become stronger with IMF along the 90% ice concentration line and along the coastline where polynyas emerge, whereas there is minimal increase over the compact ice pack. The pattern of the wind stress change is also reflected in the sea-ice velocity change (not shown), which is consistent with the study presented in the previous chapter. All of the three experimental frameworks show similar tendencies for wind stress and sea-ice velocity in association with application of the IMF, which provides a reasonable starting point toward studying the respective long-term oceanic response.

D. Results of IMF experiments

The application of the IMF is conceptually expected to increase dense water formation through increases of heat loss and new ice formation resulting from an increase in the lead fraction where ice becomes more divergent. Antarctic Surface Water (AASW) and High-Salinity Shelf Water (HSSW) are source water masses for AABW. Since they are colder and less saline than CDW and NADW, an increased volume of AABW goes generally along with colder and fresher global-mean deep-water characteristics. This

holds if CDW is only marginally involved in the AABW formation process, as in the case of near-boundary convection. If AABW is primarily formed through open-ocean convection, however, as in most ocean GCMs, CDW will become a major ingredient, and the global deep-ocean properties thus colder and saltier with enhanced AABW formation. As seen from Table 4-2, all IMF experiments cause a long-term cooling of the global deep ocean, consistent with the expected enhanced AABW formation. Salinity-wise, the deep-ocean response reveals a freshening in AIMF and slightly saltier conditions in CIMF versus their respective reference experiments which indicates more AABW formation through near-boundary convection in AIMF versus more AABW formation through open-ocean convection in CIMF. All IMF cases show a consistent increase of the ACC. Possible mechanisms that explain this IMF-induced consistent increase in the ACC in the respective experimental frameworks will be explored in the following section.

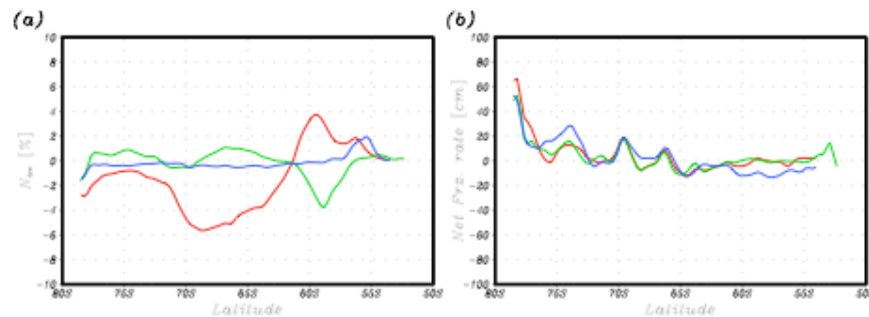


Fig. 4-3 Differences of zonally averaged winter-mean ice concentration and annual net freezing rate (AIMF minus AREF: red, BIMF minus BREF: green, CIMF minus CREF: blue lines).

1. The IMF-induced sea-ice – ocean interaction

The wind stress anomaly, which showed consistently increased wind stress fields along the coastline and along the 90% ice concentration line (Figs. 4-2d-f), incorporated

characteristics of the respective reference experiments to generate sea ice anomalies that reflect both the wind stress anomaly and the respective characteristics. Figure 4-3 shows the zonally averaged differences of the IMF-applied cases minus the respective reference cases for the winter-mean ice concentration and the annual net freezing rate. Here, the calculated ice concentration is the one before the thermodynamic process, i.e. before the wind-driven ice-free part is closed by newly formed sea ice due to the thermodynamic process. For analysis, these latitudinal distributions are divided in three domains: 1) south of 75°S , 2) between 75°S and 62°S , and 3) north of 62°S . The first domain represents coastal regions in the southern Weddell Sea and Ross Sea, the second mostly the interior sea-ice pack, as well as the coastline of East Antarctica, and the third the sea-ice edge.

The first domain shows a consistent decrease in ice concentration along the southern coastline or ice-shelf line (AIMF: decrease by about 3%, BIMF and CIMF: decrease by about 1.5%), which is in agreement with the results of the previous chapter. As explained earlier, during winter these amounts of decrease in ice concentration along the coastline can affect the formation of AABW with the following process. The IMF-induced wind stress anomalies act to accelerate offshore advection of newly formed sea ice, widen preexisting coastal polynyas, and thus increase the ocean-to-atmosphere heat loss, resulting in an increase in dense water formation along the coastline via new ice formation and surface cooling. It is supported by Fig. 4-3b showing that south of 75°S the zonally averaged net freezing rates, indicative of new ice formation, increased substantially. In particular, the AIMF that showed the largest reduction of ice concentration also shows the largest net freezing rate increases, implying an IMF-induced

increase in near-boundary convection in the high-latitude embayment of the Weddell and Ross Sea.

In the second domain, the ice concentration of CIMF decreased only very little. Since its upper-ocean temperature is constrained by the satellite-derived ice concentration, an oceanic heat flux associated with open-ocean convection does not affect SO sea ice, which render ice concentration of EXPC higher than that of the other two experiments. Therefore, the ice concentration anomaly of CIMF is affected only by the effect of wind-driven sea-ice drift, and thus is very small. AIMF shows a distinct decrease in ice concentration. It indicates more coastal polynyas along East Antarctica, which can be explained by the largest increase in wind stress along the coastline of East Antarctica (Fig. 4-2d versus Figs. 4-2e and 2f). The ice concentration anomaly of BIMF varies between about -0.5 and 1.0%. On the other hand, albeit a very little decrease in ice concentration, CIMF shows larger net freezing rates between 76°S and 73°S and between 69°S and 67°S than the other two experiments. It would be attributed to the higher ice concentration of EXPC, because a change in high ice concentration (e.g. from 99% to 95%) has a larger effect than that in relatively low ice concentration (e.g. from 79% to 75%).

In the third domain denoting the ice edge, while there is difference in response magnitudes, ice concentrations, as a whole, increased north of 56°S in all experiments. A noticeable thing is a contrasting response of ice concentrations of AIMF and BIMF in between 62°S and 56°S. It could be the effect of oceanic heat flux due to open-ocean convection in BIMF. The open-ocean convection triggered by the IMF-induced dense water along the ice edge can bring up the warm CDW to melt sea ice. However, since net

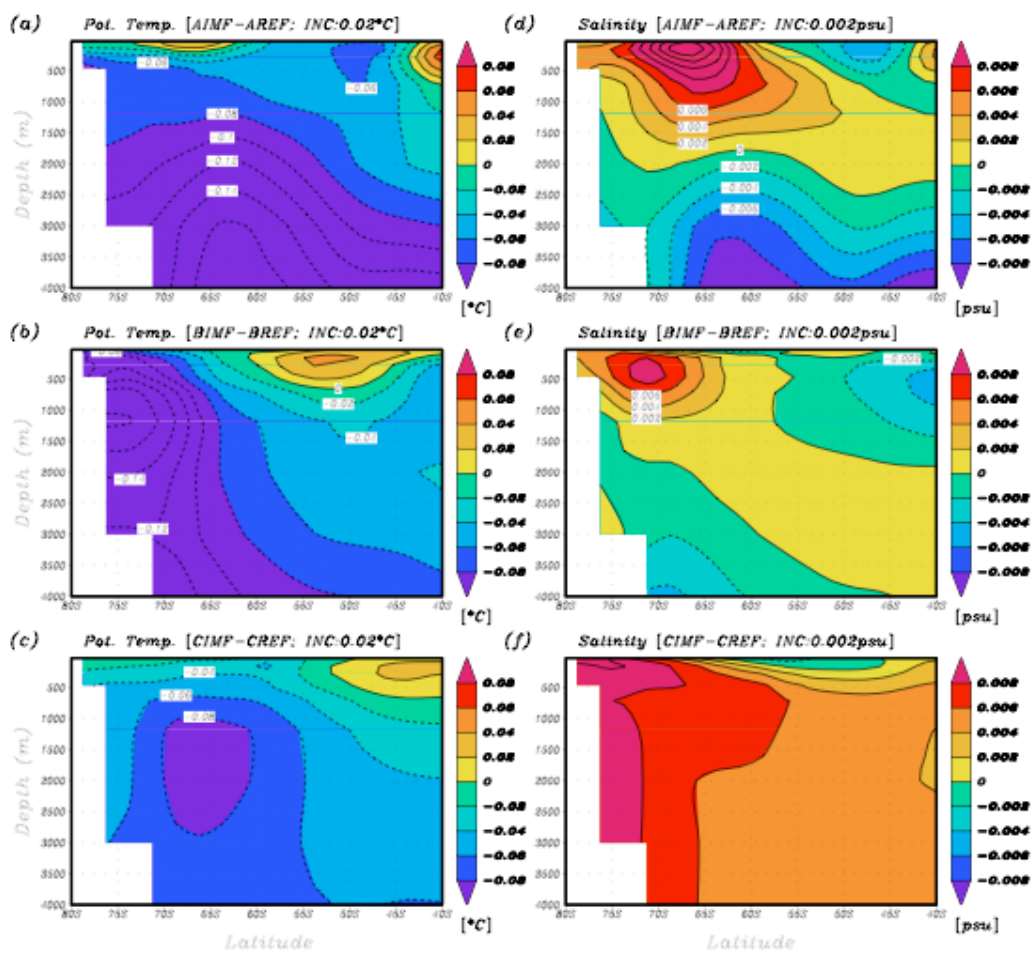


Fig. 4-4 Zonally averaged meridional sections of the global potential temperature and salinity.

freezing rate anomalies in this domain are smaller than those in the other two domains, the ice concentration anomaly is considered not to affect convection as much as that in the other two domains does.

Meridional sections of the zonally averaged potential temperature and salinity of the SO in Fig. 4-4 show a better indication of what type of convection is more enhanced by the IMF. As explained earlier, enhanced near-boundary convection makes deep- and bottom water colder and fresher, while enhanced open-ocean convection makes it colder and saltier because of the influence of CDW. The bottom water of AIMF shows the largest decreases in potential temperature and salinity, which are associated with a transmission of the cold and fresh AASW anomaly to the AABW that is rather unaffected by CDW. It is indicative of an intensified near-boundary convection associated with the IMF. Although the increased leads and open-ocean polynyas along East Antarctica build the condition to increase more new ice formation and thus more brine rejection, the high diffusivity of EXPA does not allow this saline water to be transmitted to the depth, shutting that into the upper-ocean (Fig. 4-4d). On the contrary, in CIMF the AABW is affected not only by the increased cold HSSW but also by the warm and salty CDW, thus becoming colder, but not as much as that of AIMF, and saltier (Figs. 4-4c and 4f). This salinity anomaly is attributed to both an increased brine rejection due to new ice formation (Fig. 4-3b) and an increased influence of the CDW due to open-ocean convection. Moreover, the core of maximum anomaly of cold water found far away from the continent (Fig. 4-4c) is also indicative of an intensified open-ocean convection. Although EXPB, free from any pragmatic constraint, is supposed to trigger any type of convection between near-boundary convection and open-ocean convection, an anomalous

upward oceanic heat flux associated with open-ocean convection will give rise to an anomalous ice melting, which tends to re-stratify the water column, and thus suppress open-ocean convection. As shown in Figs. 4-4b and 4e, the effect of enhanced near-boundary convection appears to yield a core of cold water at intermediate depth, while the salinity anomaly confined to the upper-ocean, which is smaller than that of AIMF (Fig. 4-4d), indicates that an intensity of open-ocean convection in BIMF is smaller than that in AIMF because of the anomalous ice melting. All the above is consistent with the anomalies in the globally averaged bottom water properties (Table 4-2).

2. The IMF-induced changes in meridional overturning circulations

The IMF-induced changes in the SH sea-ice – ocean interaction not only directly affect the SH overturning, consisting of the Antarctic overturning cell and the bottom overturning cell, but also indirectly affect the NH overturning, consisting of the North Atlantic overturning and the NADW outflow. Figs. 4-5 and 4-6 show meridional overturning circulations in the AO and the global ocean, respectively. In the AO, while the IMF, seemingly, does not exert an effect on the Antarctic overturning cell, it does give rise to a slight upward and northward expansion of bottom overturning cell, which finally leads to a slight reduction of the NA overturning and the NADW outflow (see table 4-2), uniformly in all experiments. The impact of the IMF on the meridional overturning circulation is somewhat more distinct in the global ocean. In association with the IMF, the Antarctic overturning cell is uniformly enhanced, and moreover, not only is the sphere of influence of the bottom overturning cell expanded, but also the intensity of

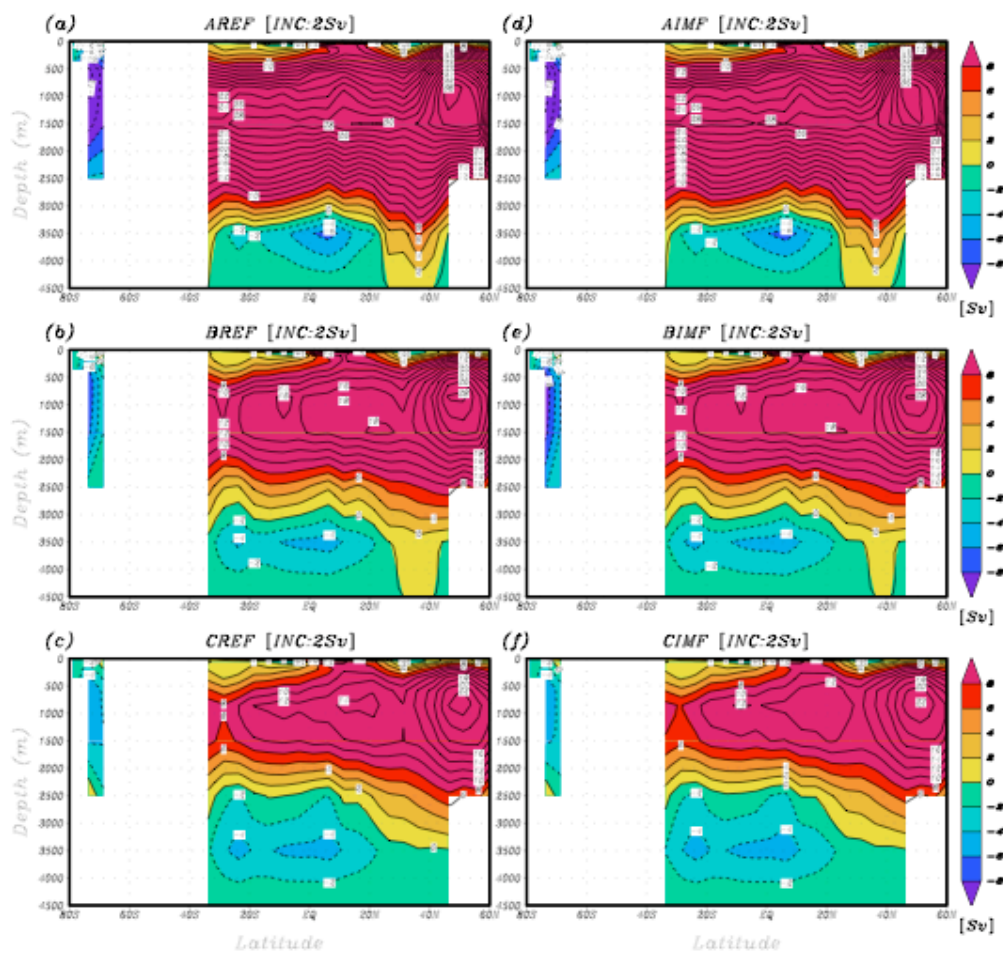


Fig. 4-5 Meridional overturning circulations in the Atlantic Ocean.

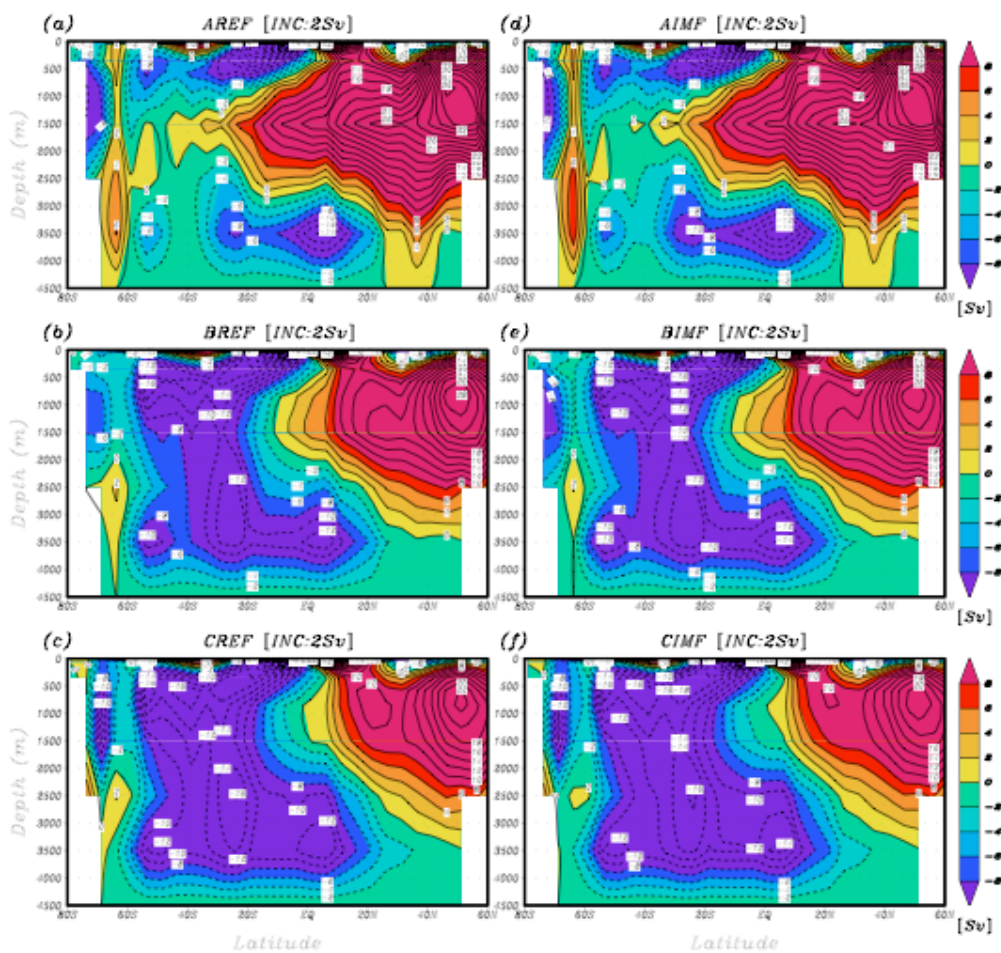


Fig. 4-6 Meridional overturning circulations in the Global Ocean.

the northward intrusion of AABW. Along with the intensification of the SH overturning, the sphere of influence of the NH overturning slightly shrinks with the IMF. It is important to note that the IMF gives rise to consistent changes in the global meridional overturning circulation in all three experimental frameworks, even though their respective mean state is considerably different.

3. Long-term baroclinic adjustment of the ACC to the IMF

The mechanism that can explain the world's largest eastward volume transport, the ACC, still remains unclear. Two major components that sustain the ACC are the influence of SWWs, and the so-called Drake Passage effect: the fact that the latitude band containing Drake Passage does not meet any coasts of the major continents, which results in the lack of zonal pressure gradients, and thus the lack of meridional geostrophic flow above the ridge depth of about 2000 *m*. Based on these two issues, the question about what sets the transport of the ACC has been widely approached with moot points on the dynamic and thermodynamic balances associated with the SWWs. There are two arguments on the dynamic balance: 1) the dependence on the mean stress so-called "bottom form drag" or "mountain drag" (e.g. Wang 1994; Krupitsky and Cane 1994; Stevens and Ivchenko 1997; Olbers 1998; Gent et al. 2001) and 2) the dependence on the wind stress curl based on the Sverdrup balance (e.g. Warren et al. 1996). Such approaches have some advantages in that the current comes into dynamic balance relatively quickly. However, such a short-term adjustment is not sufficient for assessing

the response of the ACC to the long-term oceanic adjustment, which is mainly associated with thermodynamic balance. Gnanadesikan and Hallberg (2000) first showed how the effect of anomalous SO winds is, by means of the thermodynamic balance, transmitted to the ACC. They argued that the baroclinic part of the ACC depends directly on the winds within Drake Passage, in the framework of a coarse-resolution ocean GCM with restoring surface conditions. Based on the argument of TS93 and TS95, an increased northward Ekman transport due to anomalous SO winds is considered to enhance the NA overturning, leading to an increase in northward heat transport. This process warms (cools) the ocean north (south) of the ACC. These changes are then reflected in the meridional density gradient, which lead to the stronger ACC by way of an increased thermal wind shear. In contrast to the baroclinic adjustment of the ACC derived from the anomalous northward Ekman transport in the SH (e.g. Gnanadesikan and Hallberg 2000), the IMF in this chapter directly strengthens the SH overturning via the enhanced SO convection and indirectly weakens the NA overturning, which renders the SO colder and saltier (Fig 4-4). Finally, the volume transport of the ACC consistently increases with the application of the IMF (table 4-2).

E. Summary

The response of the SH overturning to the IMF over sea ice and its impact on the global ocean circulation were investigated in three different experimental frameworks. While there are differences in response magnitudes with the respective frameworks, the IMF-induced positive feedback between the unstable ASL condition over sea ice and the

atmospheric momentum flux appeared to uniformly operate mostly along the coastline and partly and conditionally in the interior and the edge of the pack ice, enhancing ice drift. This appeared to play a role in widening preexisting coastal polynyas as well as conditionally triggering open-ocean polynyas, which finally intensify near-boundary convection and open-ocean deep convection, respectively. In detail, AIMF shows a dominance of anomalous near-boundary convection over anomalous open-ocean convection, while CIMF shows an opposite dominance. The response of BIMF is in between those of AIMF and CIMF. While responses of deep- and bottom water properties to the IMF are somewhat different due to the different contributions of near-boundary convection and open-ocean deep convection, the IMF appeared to consistently strengthen (weaken) the SH (NH) overturning in all experimental frameworks. Another important oceanic response to the IMF was the consistently increased ACC via the long-term baroclinic adjustment. Both the strengthened SH overturning and the weakened NH overturning play a role in increasing the meridional density gradient across the latitude band containing Drake Passage. Therefore, the thermal wind shear strengthens, and so does the volume transport of ACC.

Throughout this chapter, the climatic signals naturally generated by the atmospheric momentum anomaly, i.e. the IMF over sea ice, turned out to be able to not only directly perturb the SH overturning via the complex sea-ice – ocean interaction anomalies, but also indirectly perturb the NH overturning. It implies that the SH overturning is not just a passive component in the global overturning circulation system. Besides, as the current warming of the world is accelerated by the human activity, the long-term high polarity of SAM will perturb the SWWs, which is a major driving force

for the northward Ekman flux as well as the SH sea-ice – ocean interaction. Then, the role of the SH overturning is expected to be more important than in the present-day climate. The next chapter addresses how an external forcing anomaly associated with the positive SAM can simultaneously perturb interhemispheric overturning circulations with different mechanisms and how its long-term baroclinic adjustment affects the volume transport of ACC.

CHAPTER V

OCEANIC RESPONSE TO THE POLEWARD SHIFTED SOUTHERN
HEMISPHERE SUBPOLAR WESTERLY WINDS

A. Introduction

In the previous chapter, the dense water formation anomalies, naturally intensified by the application of IMF, perturbed the SO convection system consisting of near-boundary convection and open-ocean convection, and thus enhanced the SH overturning (i.e. the bottom cell overturning), which led to a reduction of the NH overturning (i.e. the North Atlantic overturning). These changes originating from the IMF over the SO sea ice appeared to be able to perturb the global ocean conveyor belt system and finally increase the volume transport of the ACC. Then, in climate issues associated with the GHGs warming, what in the SH can simultaneously perturb both the SH overturning through the anomalous sea-ice – ocean interaction and the NH overturning through the anomalous northward Ekman transport?

According to the recent Intergovernmental Panel on Climate Change (IPCC) report, the global warming accelerated by the anthropogenic greenhouse gases such as carbon dioxide seems to give rise to a poleward shift and intensification of the SWWs, the mechanism of which has been explained by the positive SAM. The SAM, also known as the Antarctic Oscillation (Gong and Wang 1999), is a pervasive mode of climate variability that affects the atmosphere, ocean, and sea ice at mid and high latitudes over a

wide range of time scales (Thompson and Wallace 2000), so such a change implies a major shift in the broadscale climate of this hemisphere. Basically, large differences in the radiation budget between the tropics and the poles result in global-scale meridional temperature gradients, particularly showing a strong tendency at mid-latitudes. In the troposphere, these meridional temperature gradients result in thermal wind shear to drive a predominantly geostrophic westerly wind, which extends from the surface and reaches maximum strength in the upper troposphere as the subtropical jet. This strong flow generates the energy for baroclinic instability and the formation of transient eddies. These eddies not only are associated with a large degree of variability, but also have the ability to interact with and feedback onto the mean flow. A north-south oscillatory SAM acts to swing atmospheric mass, and thus gives rise to a perturbation in the meridional pressure field, ultimately leading to a zonal geostrophic wind anomaly at mid latitudes. It is supported by observational (e.g. Hartmann and Lo 1998; Lorenz and Hartmann 2001) and model (Limpasuvan and Hartmann 2000; Codron 2005) studies suggesting a positive feedback between the zonal wind and fluxes of transient eddy momentum driven by the meridional pressure gradient. Therefore, the dominant mode of variability associated with the SWW fields is characterized by swings between a poleward-shifted and intensified flow and an equatorward-shifted and weakened flow.

The issue that the SAM has drifted toward a high index polarity during the past few decades has been assessed by use of the reanalysis data (Thompson et al. 2000, 2005), station data (Marshall 2003; Thompson et al. 2005), and climate models (Kushner et al. 2001). Using a coarse-resolution climate model, Hall and Visbeck (2002) showed that the poleward movement and intensification of the atmospheric jet stream associated

with the positive SAM result in strengthening westerly winds at about 55°S and weakening at about 35°S, which exert an effect on both the atmosphere and the ocean. In the atmosphere, the surface meridional flow anomalies generated by the zonal wind fluctuations exerts both the effect of generating convergence anomalies at around 65°S, and thus rising motion of air in order to satisfy mass continuity, and of generating divergence anomalies at around 40°S, and thus subsidence of air. In the ocean, the surface westerly anomalies act to enhance the northward Ekman transport between about 45° and 65°S, while the surface easterly anomalies act to create southward Ekman transport anomalies between 30° and 45°S, which lead to an increase in upwelling (downwelling) around the Antarctic coast (at about 45°S). While there are substantial differences in the response magnitude, the overall concept about these SAM-induced anomalies in the atmosphere and the ocean is in good agreement with the recent analysis of results of Sen Gupta and England (2006) using a higher-resolution climate model and reanalysis datasets.

The long-term positive SAM results in poleward shifted and intensified SWWs, which can be divided into contributions from intensification and from shift, respectively. The former has been well documented in the framework of ocean-only GCMs (TS93; TS95; RE97; Gnanadesikan and Hallberg 2000) and a sea-ice – ocean coupled GCM (Brix and Gerdes 2003). With regard to SWW shift, Oke and England (2004; hereafter denoted as OE04) using an ocean-only GCM assessed the oceanic response to a poleward shift of the SWWs by 5.4° (hereafter denoted as PSW) in their 100-year trend experiment.

The objective of OE04 was to assess ocean sensitivity to changes in the latitude of the SWWs, and their experiments were motivated by the recent observation (Gille 2002) showing a significant intermediate depth ($\sim 700\text{ m}$) cooling at mid latitudes and larger-than-expected warming at high latitudes over the past 50-100 years. It means that they focused on the short-term oceanic adjustment to the PSW. Following the experimental design of OE04, the PSW is, in this chapter, further explored by adding two factors that lead to conclusion that are inconsistent with the OE04. First, the sea-ice – ocean coupled GCM used in this study provides the ocean with thermohaline flux forcing generated by the sea-ice – ocean interaction, which was excluded in OE04. While there are probably differences in magnitudes and patterns, the anomalous overturning induced by the IMF is expected to become amplified by virtue of the PSW. Second, the 100-year integration in their trend anomaly experiment is insufficient for evaluating mean transports of the deep-ocean circulation. This study allows focusing on the long-term oceanic response to perturbation of the momentum forcing, including transient responses of the sort investigated in OE04.

Isolating the impact of the PSW on the ocean is expected to be a step toward understanding the multitudinous impacts of poleward shift and intensification of the SWWs. A simple description for this experimental setup follows in the next section. The PSW-induced interhemispheric changes are discussed and compared with the results of OE04 in section C. A summary and conclusions are provided in section D.

B. Experimental setup

As discussed earlier, the IMF-accelerated wind-driven divergences of sea ice along the coastline and the 90% ice concentration line appeared to enhance near-boundary convection and conditionally trigger open-ocean convection, respectively. This constitutes a central frame of the SH sea-ice – ocean interaction system, which is also expected to play an important role in case of the PSW-induced intensification of divergent wind fields over the SO. For this reason, the same reference experiments, which were useful for investigating the robustness of the oceanic responses to the IMF in the previous chapter, are again employed here (refer to chapter IV).

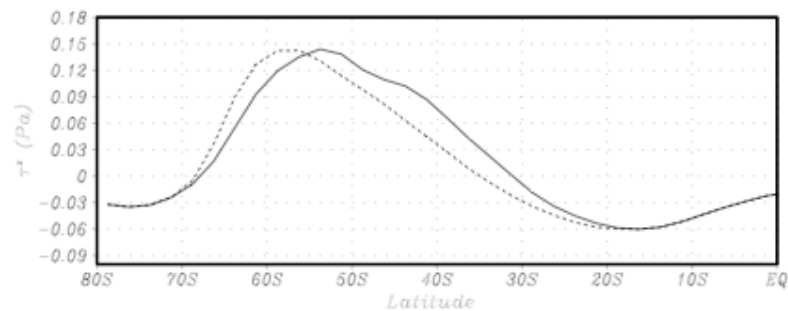


Fig. 5-1 Zonally averaged annual-mean zonal wind stress.

The zonally averaged annual-mean zonal wind stress for the PSW is compared to the one for the reference case in Fig. 5-1. As discussed earlier, the maximum strength of the zonally averaged annual-mean zonal wind stress remains unchanged throughout the experiments. The reference case shows its peak at 53°S, while in the PSW case it is shifted to 58°S. The westerly winds are weakened between 55°S and 35°S, while the winds are enhanced between 70°S and 55°S, which yields an intensification of the negative wind stress curl south of 58°S. Between 35 °S and 30°S the original westerly

wind field is changed into an easterly wind field, and north of 30°S the preexisting easterly wind field is strengthened. There is no change north of 20°S and south of 70°S.

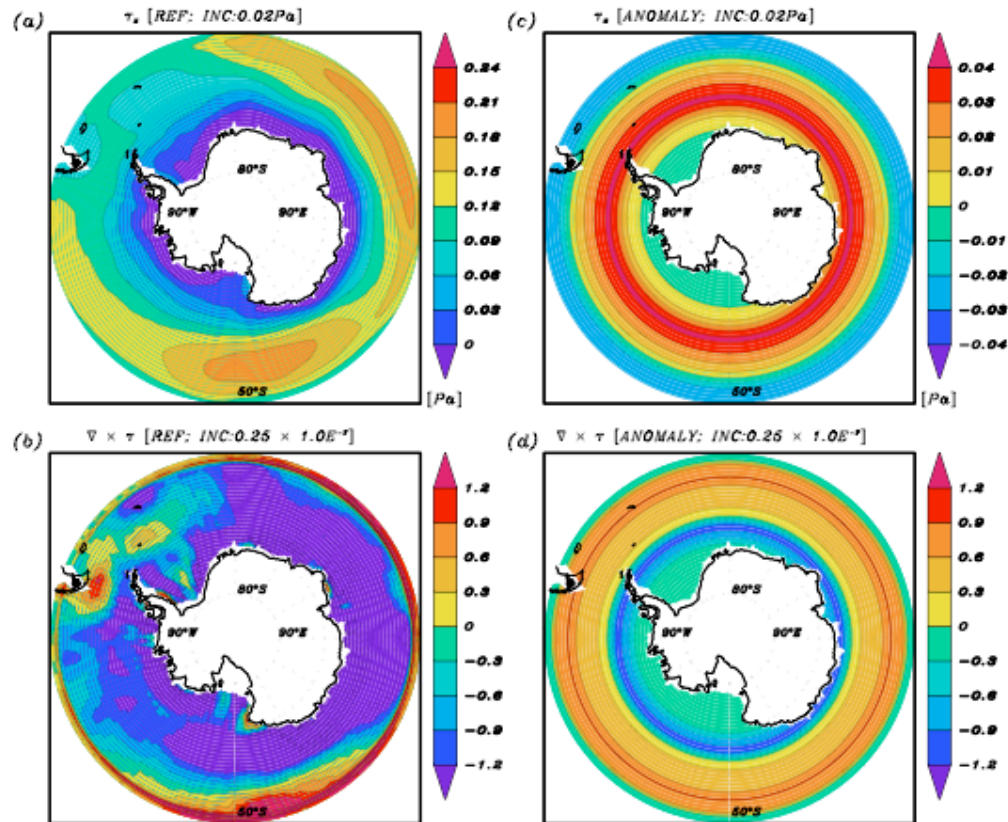


Fig. 5-2 Annual-mean wind stress magnitude and curl of reference and anomaly.

A noticeable issue is that the wind fields south of 50°S in this study are different from those in OE04. The overall winds applied at the surface are identically derived from Hellerman and Rosenstein (1983, hereafter HR83), while in the model used here ECMWF daily wind fields are employed south of 50°S for a realistic reproduction of the SO sea ice. A comparison between the two wind fields (refer to Fig.1 in Oke and England 2004) suggests two interesting points. First, the westerlies predominant over the subpolar region turn into easterlies at about 68°S and therefore easterlies are prevailing near the Antarctic continent in the ECMWF winds, while the westerlies of HR83 extend to about

75°S, the easterlies emerging only marginally in the high-latitude embayment. As explained earlier, the Antarctic coast is, actually, under the influence of prevailing easterly winds. Moreover, the ECMWF westerly winds are stronger than the westerly winds of HR83 in the subpolar region. Second, the strongest westerly winds of HR83 are located at about 48°S, i.e. farther north of the latitude containing Drake Passage, as well as north of the latitude the ECMWF westerly winds peak. A complex effect results from the aforementioned two points which may give rise to serious differences between the SO circulations produced by the two experimental setups.

Fig. 5-2 furnishes detailed features showing horizontal distributions of the annual-mean zonal wind stress, wind stress curl, and their PSW-driven anomalies. Under the influence of yearlong low-pressure systems moving around the Antarctic continent, the whole coastal areas are dominated by easterly winds, while the sea-ice – ocean surface far away from the continent is dominated by the westerly winds, which show a distinct wave number-3 pattern. Moreover, most areas south of 50°S are under the influence of negative wind stress curl. The complex geographical projection associated with the southern limb of South America and the Antarctic Peninsula seems to play a role in breaking the zonal wave. As shown in Fig. 5-2c, the PSW pulls the surface westerly jet deep into the SO, which implies that during winter the ice edge is entirely under the influence of the jet that exerts both the effect of enhancing the eastward component of the ice velocity and of enhancing the northward Ekman drift of ice. Consistent with OE04, Fig. 5-2d shows that the negative wind stress curl south (north) of about 60°S is intensified (weakened), which also implies that the rate of upwelling of CDW south (north) of about 60°S will increase (decrease).

In contrast to the application of the IMF that allows only the momentum flux to be modified by the simulated sea-ice conditions, the application of PSW affects the sea-ice – ocean system dynamically and thermodynamically.

C. Results

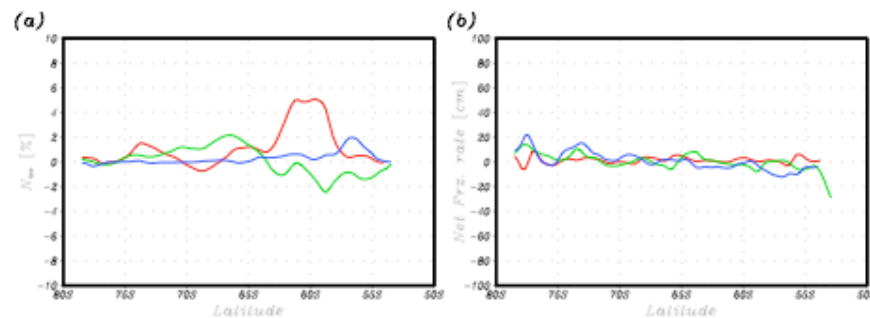


Fig. 5-3 Differences of zonally averaged winter-mean ice concentration and annual net freezing rate (APSW minus AREF: red, BPSW minus BREF: green, CPSW minus CREF: blue lines).

Figure 5-3 shows the zonally averaged differences of the IMF-applied cases minus the respective reference cases for the winter-mean ice concentration and the annual net freezing rate. Same as Fig. 4-3a, the calculated ice concentration is the one before the thermodynamic process. South of 70°S, any distinct decrease in the ice concentration is not found. The contrasting response of ice concentration of APSW and BPSW north of 65°S is similar with that of AIMF and BIMF shown in Fig. 4-3a. The net freezing rates of BPSW and CPSW increased by less than 20 cm near 78°S and 73°S, while that of APSW decreased slightly near 78°S. In contrast to the IMF-induced substantial changes along the coastline (see Fig. 4-3), the PSW, as a whole, did not give rise to large changes in ice concentration and net freezing rate. This is attributed to the experimental setup in that the zonal wind stress fields south of 70°S are not changed. Now one can expect that the

PSW-induced anomalous sea-ice – ocean interaction does not affect the SH overturning as much as the IMF-induced one did, which allows focusing on the linkage between the PSW-induced northward Ekman transport anomaly and the NA overturning and NADW outflow.

Table 5-1. As in Table 4-2 but for the comparison with the PSW-applied cases (abbreviations explained in text). Unit of the NA overturning, NADW outflow, and ACC is Sv .

	AREF	APSW	BREF	BPSW	CREF	CPSW
θ_{4000m} [$^{\circ}C$]	2.35	2.20	0.97	0.75	0.54	0.38
S_{4000m} [psu]	34.635	34.622	34.678	34.655	34.775	34.755
NA overturning	38.1	36.4	28.6	27.3	23.3	21.5
NADW outflow	27.1	26.8	12.3	10.9	8.3	7.8
ACC	88.2	77.4	99.9	87.4	111.3	95.1

Table 5-1 shows selected mean-state choke point numbers of the thermohaline circulation for the listed experiments. The PSW has both the uniform effect of substantially cooling and freshening the deep ocean (steady-state global mean at 4000 m depth), which is indicative of an increased AABW formation, and of decreasing the maximum transport of North Atlantic overturning and the NADW outflow. The most noticeable change associated with the PSW is the substantially decreased transport of the ACC, which is going to be a major issue in this section because it is entirely contrary to the result of OE04. It is quite striking that the impact of PSW is consistent in all three experimental frameworks, thus supporting its robustness. Detailed features are illustrated in Figs. 5-4 and 5-5 showing meridional overturning circulations in the AO and the global ocean for the reference experiments and the PSW-applied experiments. Noticeably, the maximum transports in both the NA overturning cell (Fig. 5-4) and the

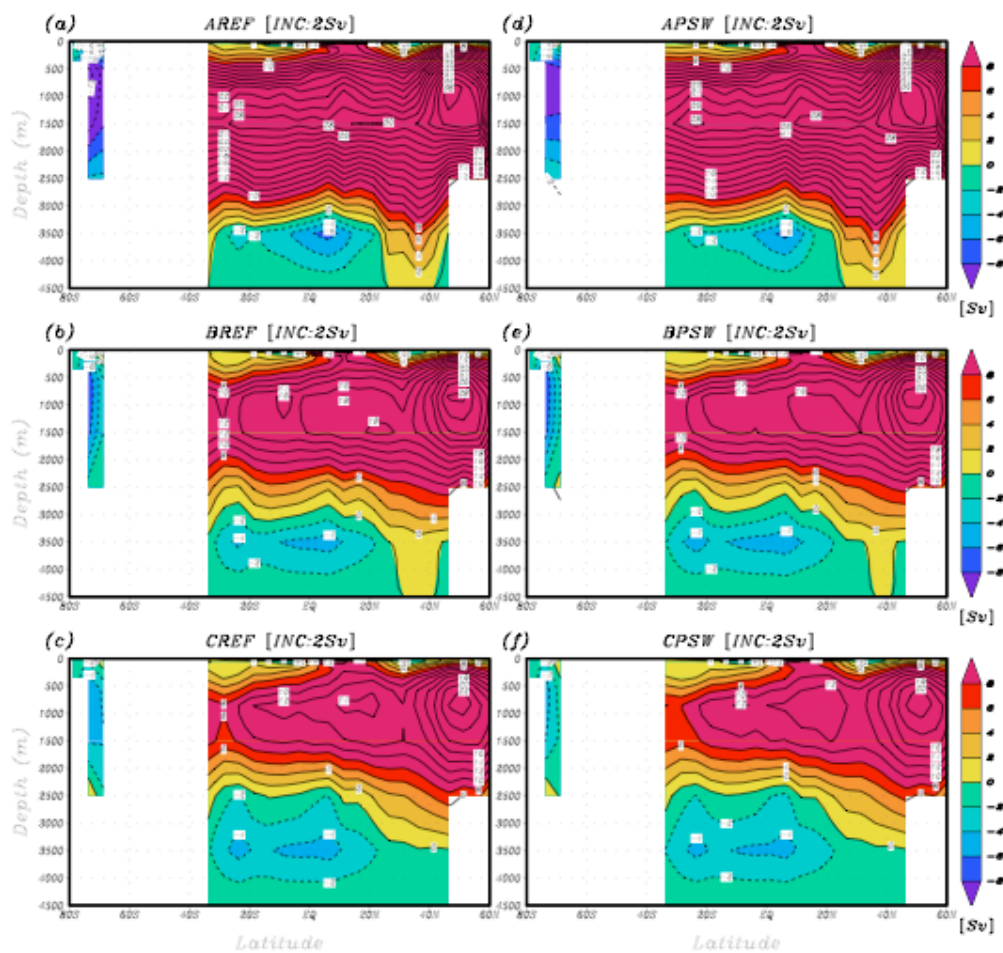


Fig. 5-4 Meridional overturning circulations in the Atlantic Ocean.

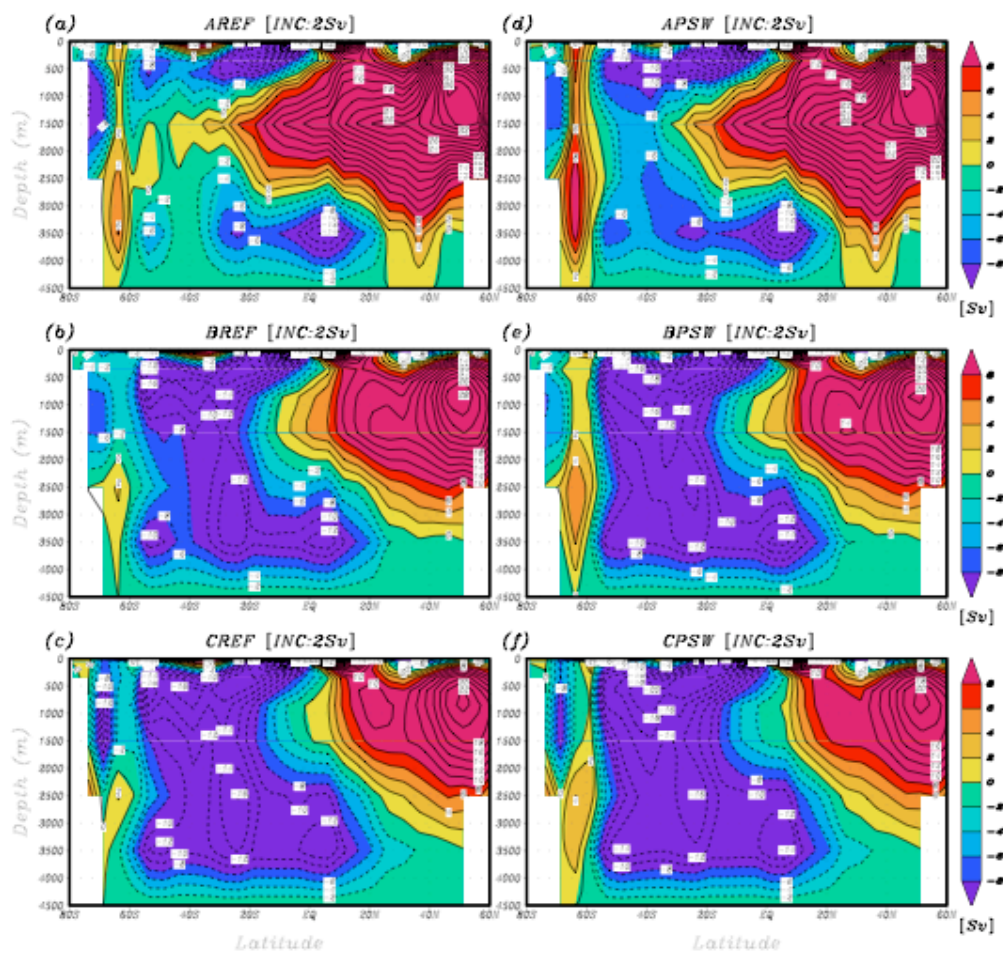


Fig. 5-5 Meridional overturning circulations in the Global Ocean.

NH overturning cell (Fig. 5-5) consistently decreased with application of PSW. The bottom cell in the AO expanded slightly upward and farther north only in BPSW. In the globe, the expansion and intensification of the bottom cell overturning both become distinct. As discussed above, these are mainly attributable to the anomalous northward Ekman transport rather than the anomalous SH sea-ice – ocean interaction. Consistent with OE04, the PSW causes the Deacon cell overturning to uniformly deepen and strengthen. On the other hand, the enhanced Deacon cell overturning, seemingly, suppresses the Antarctic cell, which is also in agreement with OE04.

Table 5-2. Maximum transports of the NA overturning, Antarctic overturning, and SH overturning, outflow of NADW, and Drake Passage throughflow (ACC) in control case (CNTRL) and trend experiment of the PSW (results quoted from Oke and England (2004)). Unit of the NA overturning, NADW outflow, and ACC is Sv .

	NA overturning	NADW outflow	Antarctic overturning	SH overturning	ACC
CNTRL	10.6	6.6	7.7	13.6	126.4
PSW	10.6	6.7	6.4	13.8	132.1

It seems to be necessary to first review the results of OE04 here because the results of this study are not consistent with those of OE04. The PSW-induced changes in the global ocean circulation quoted from OE04 are summarized in Table 5-2. The NA overturning, NADW outflow, and SH cell overturning remain virtually unchanged, while the Antarctic overturning cell and the Drake Passage Throughflow (i.e. ACC) decrease by $1.1 Sv$ and $4.3 Sv$, respectively. Their argument was mainly based on three additional PSW-induced changes. First, the Deacon cell deepens and shifts poleward, albeit no virtual change in the rate of meridional overturning. The increased (decreased) wind stress curl north (south) of $60^{\circ}S$ is speculated to increase (decrease) local Ekman

pumping that exert an effect on the change of the Deacon cell, which also results in deepening (shoaling) of the thermocline and halocline (i.e. isopycnal). Second, the zonally averaged global northward heat transport (NHT) showed a broad negative anomaly between 50°S and 0°. Changes in Ekman transport, interestingly, appeared to contribute significantly to the peak in the anomaly at 40°S with a band between 30°S and 50°S (refer to Fig. 5 in Oke and England 2004), while there was also a broad NHT anomaly that is not directly explained by the Ekman component. Third, north of the latitude band of Drake Passage, waters above 1500 *m* depth has become significantly colder and fresher (refer to Fig. 6 in Oke and England 2004), which appeared to be a compound of changes in the $T - S$ properties of water masses and changes due to isopycnal shoaling or deepening, so-called “heaving” (Bindoff and McDougall 1994). OE04 concluded that the cooling of the Subantarctic Model Water (SAMW), rather than changes in its rate of formation, is primarily responsible for the PSW-induced negative NHT anomaly, which was speculated to be attributable to an increase in the northward advection of colder water in the Ekman layer. In particular, they interpreted the aforementioned Ekman component of the NHT anomaly as an increase in the northward advection of cold water in the Ekman layer around 40°S.

Here, I would like to propose two doubtful points on the above argument in the range of their experimental framework, not through the comparison with the results of this study. First, does the Ekman component of NHT anomaly really indicate anomalous northward advection of cold water in the Ekman layer around 40°S? As the maximum westerlies move poleward, a larger amount of cold waters are certainly expected to sink along the isopycnals and flow northward, not to just flow northward in the Ekman layer.

Moreover, their experimental design of the zonal wind stress anomaly (refer to Fig. 1 in Oke and England 2004) indicates a decrease (increase) in the westerly (easterly) winds between 50°S and 30°S (between 30°S and 20°S), which implies a decrease (increase) in the northward (southward) Ekman transport. A certain amount of decrease in the northward Ekman transport of cold water, which is expected to sink along the isopycnal around 40°S , can be connected to an enhanced influence of the southward transport of warm water in the Ekman layer. Therefore, the increased southward Ekman transport of warm water from the tropics is presumed to be responsible for the Ekman component of NHT anomaly. Second, was there really an increase in the rate of formation of AAIW? Their passive tracer experiment does not seem to be a proper way to monitor changes in the rate of production of AAIW caused by the PSW. The passive tracers for AAIW were located only in the latitudinal band between 60°S and 50°S , and the latitude of the maximum westerly winds was shifted from 48°S to 53°S , which means that the latitude of the maximum northward Ekman transport and the maximum upwelling shifts from a location without passive tracers to a location with passive tracers. Therefore, it is natural for the PSW to increase the concentration of tracers, but it is unlikely to indicate an increase in the rate of formation of AAIW. The Deacon cell is rather to be a proper indication of the rate of formation of AAIW, and it appeared to remain unchanged. Besides, if the rate of formation of AAIW increased, it meant an increase in the wind-driven northward Ekman transport. In that case, the rate of formation of NADW, on the basis of TS95 and RE97, should increase. Moreover, in OE04, the rate of formation of NADW remained unchanged.

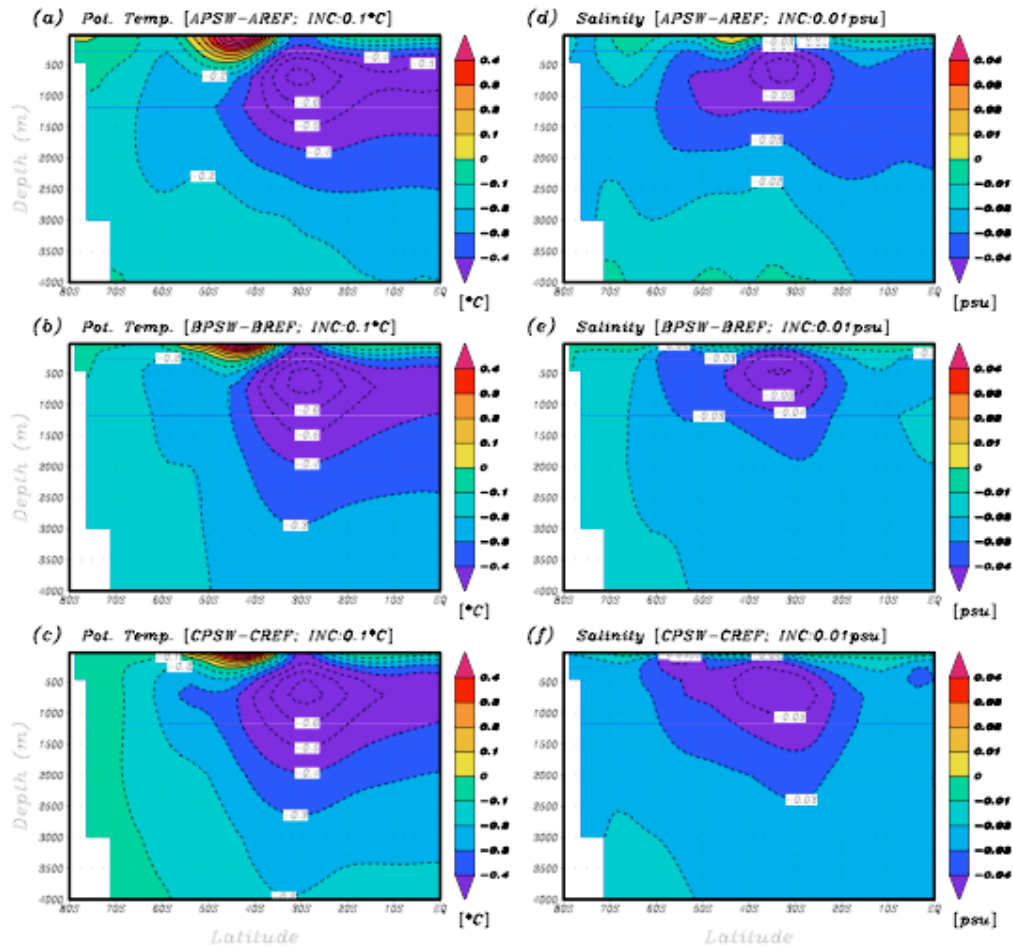


Fig. 5-6 Meridional sections of global potential temperature and salinity.

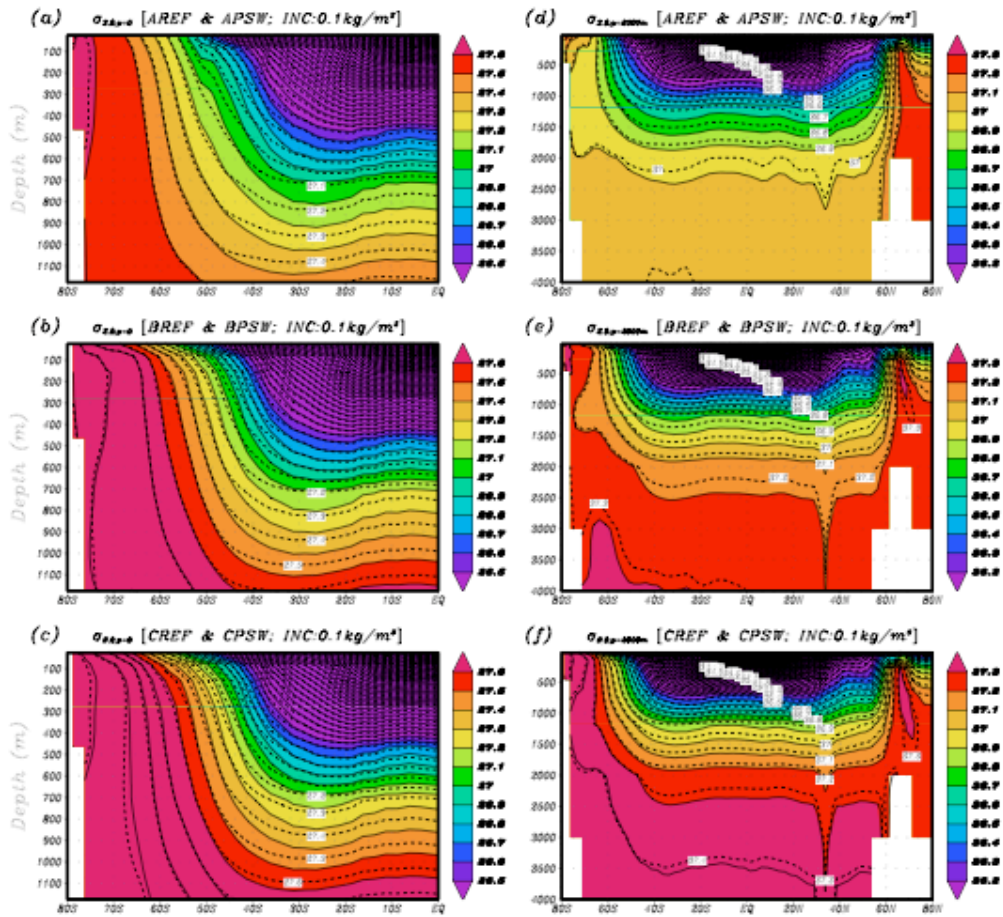


Fig. 5-7 Zonally averaged global density ($\sigma_{s,\theta,p=2000m}$ and $\sigma_{s,\theta,p=0}$) fields (REF: solid, PSW: dashed lines)

Figure 5-6 shows the PSW-induced anomalous fields of the zonally averaged potential temperature and salinity in the SH. In all experiments, a substantial warming is uniformly found in the upper ocean between 55°S and 35°S, while the rest of the ocean in the SH has become colder and fresher. While the former does not emerge in OE04, the anomalous $T - S$ fields above 1500 m are in agreement with those in OE04. Mechanisms that could explain the upper-ocean warming within these latitudes include an increased (decreased) southward (northward) transport of warm (cold) water from the tropics (SH high latitudes) through the wind-driven Ekman layer and a deepening of the thermocline caused by an increased local Ekman pumping. However, in these latitudes the local Ekman pumping actually decreased with the PSW because there is weakening of the westerlies in this latitudinal band (see Fig. 5-1), so the latter mechanism is excluded. On the other hand, mechanisms that could explain an overall cooling and freshening of the ocean in the SH are 1) an increased northward Ekman transport of cold water, 2) northward Ekman transport of colder water, 3) a decreased formation rate and outflow of NADW, and 4) an increased formation rate of AABW. These factors are explored in more detail below.

Figure 5-7 shows the zonally averaged fields of $\sigma_{S,\theta,p=0}$ for the upper 1200 m in the SH and $\sigma_{S,\theta,p=2000m}$ for the upper 4000 m of the global ocean in the reference cases (solid lines) and the PSW-applied cases (dashed lines). In association with the PSW, the isopycnals of $\sigma_{S,\theta,p=0}$ deepen and steepen in the upper-ocean ($> 500 m$) between 55°S and 35°S (Figs. 5-7a-c), which can be explained by two processes. First, as shown in Fig. 5-1, the westerlies driving northward Ekman transport are weakened by the PSW between 55°S and 35°S, implying a decrease in cold water transported northward in the Ekman

layer. Moreover, the westerlies are changed into easterlies, or the easterlies are intensified by the PSW between 35°S and 20°S, implying an increase in warm water transported southward in Ekman layer. These Ekman transport anomalies cause an increase in poleward heat transport in the Ekman layer, in other words the PSW-induced negative NHT anomaly, which is consistent with OE04. Therefore, the upper-ocean warming (Figs. 5-6a-c) is due to the PSW-induced negative NHT anomaly, and is responsible for the deepening of isopycnals of $\sigma_{S,\theta,p=0}$ between 55°S and 35°S. Second, in contrast to the increased ‘cold’ water transported northward in the Ekman layer between 55°S and 35°S, there is an increased amount of ‘colder’ water flowing northward in the Ekman layer where the westerly winds are intensified by the PSW (67°S-55°S in this study; 75°S-50°S in OE04). This colder water then sinks along the steep isopycnals when this water meets the Antarctic Polar Front (APF). Net buoyancy loss associated with the anomalous cold water plays a role in making the isopycnals of $\sigma_{S,\theta,p=0}$ steeper.

Then, what mechanisms are behind the overall cooling and freshening of the ocean? Although the ocean north of 20°S is not directly affected by the PSW, the isopycnals ($\sigma_{S,\theta,p=0}$ and $\sigma_{S,\theta,p=2000m}$) substantially shoal, even in the northern high latitudes (Fig. 5-7). This indicates that the PSW-induced changes affect the global ocean circulation, which implies the combined effects of an expanded and/or intensified SH overturning, a weakened NA overturning, and a decreased NADW outflow (Table 5-1 and Figs. 5-5 and 5-6). If so, what about the possibility proposed by OE04 that the increased northward Ekman transport of cold and fresh water and the associated increase in AAIW are responsible for the overall cooling and freshening of the ocean? A doubtful

point of whether the PSW really acts to increase the total amount of northward Ekman transport in the SO and the AAIW or not is addressed in the following.

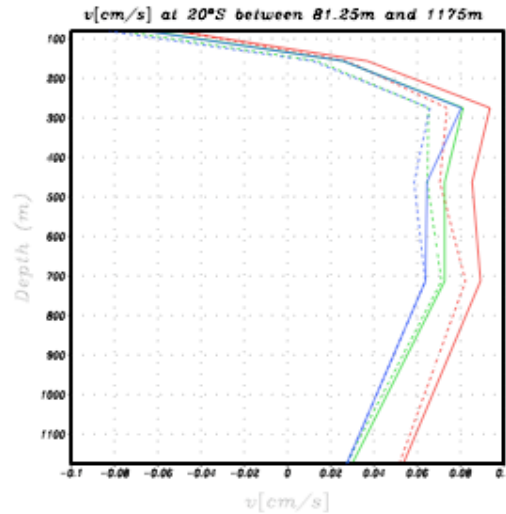


Fig. 5-8. Vertical profiles of zonally averaged meridional velocity.

At first, the PSW induces an *increased* northward transport of *colder* water in the Ekman layer, albeit it is not clear whether the total amount of northward Ekman transport increases or not. The increased northward Ekman transport between 67°S and 55°S will to a large extent counterbalance the decrease between 55°S and 35°S. Considering furthermore the meridian convergence, the total amount of northward Ekman transport would rather be expected to decrease than increase. The northward Ekman transport plays a role in spreading water properties of AASW northward, which in turn plays an important role in the circumpolar formation of AAIW (Rintoul and England 2002; Santoso and England 2004). As previously shown in Figs. 4-2e-h, the northward intrusion of AAIW and the southward intrusion of NADW are usually found at about 700 m and between 2000 m and 3000 m, respectively. Therefore, the meridional velocity at each depth can be used to measure the intensity of the respective water mass. As shown in Fig.

5-8, zonally averaged northward velocities at intermediate depth consistently decreased with the PSW, implying decreases in AAIW intrusion. This is contrary to the argument of OE04. Southward velocities averaged over the AO at depth (2000 *m*-3000 *m*), which denotes the NADW outflow, also consistently decreased (not shown here). Now, let's list clues associated with the PSW and conjecture what mechanisms are behind the overall cooling and freshening of the ocean.

First, as the SWWs shift poleward, the latitude band of the maximum northward Ekman transport approach the Antarctic continent, and thus the *colder* and *saltier* waters flow northward in the Ekman layer (refer to Figs. 4-2e-h) and sink along the isopycnals. Second, the northward transport of AAIW decreases. Third, the total amount of northward Ekman transport is presumed to decrease. Fourth, the warm and salty NADW outflow decreased. Here, I think that the AAIW did not play a role in the cooling and freshening of the global ocean as much as OE04 argued. Based on the decreased northward velocities at intermediate depth, the AAIW was judged to decrease. But, following the arguments of OE04, if the AAIW increased with the PSW, and if the increased AAIW were responsible for the cooling and freshening, it contradicts the first clue in the above. Therefore, I think that the most straightforward explanation is the fourth clue. The PSW-induced decrease in the warm and salty NADW outflow is responsible for the cooling and freshening of the ocean.

Then, let's talk about what mechanism is behind the decreased NA overturning and NADW outflow. I.e., how is the AAIW anomaly connected to anomalies in the NA overturning and NADW outflow? Since three reference frameworks have shown consistent responses to the PSW, only the PSW sensitivity of EXPB is considered in the

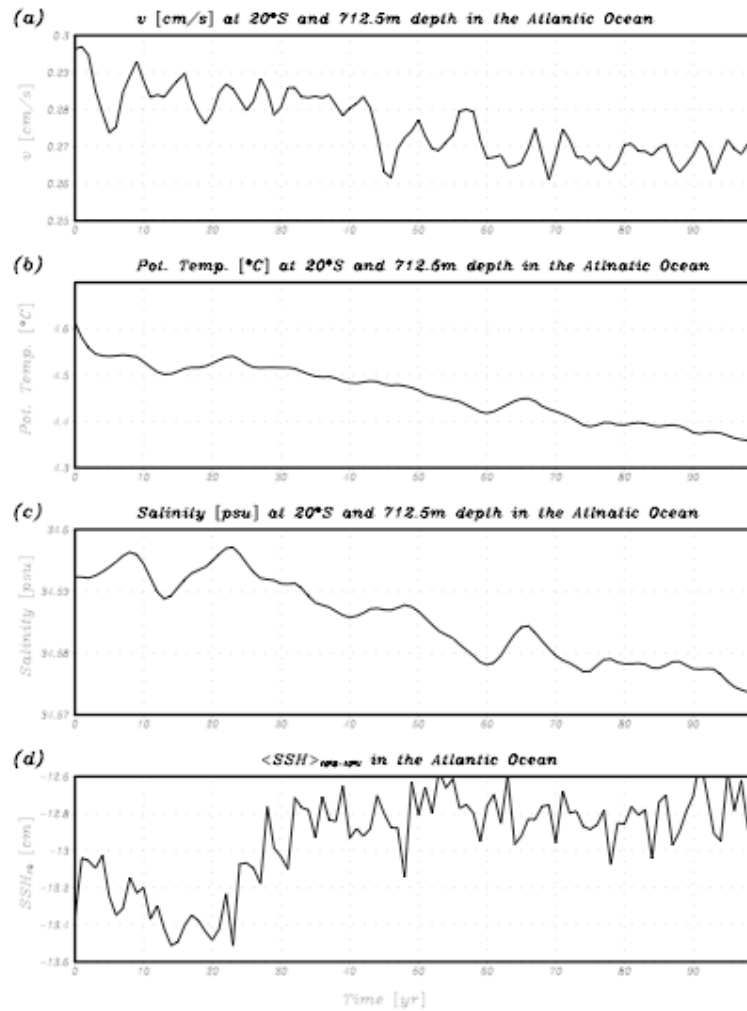


Fig. 5-9 Zonally averaged meridional velocity, potential temperature, and salinity at 20°S, and zonally averaged SSH averaged from 10°S to 10°N in the Atlantic Ocean for the first 100 years (BPSW).

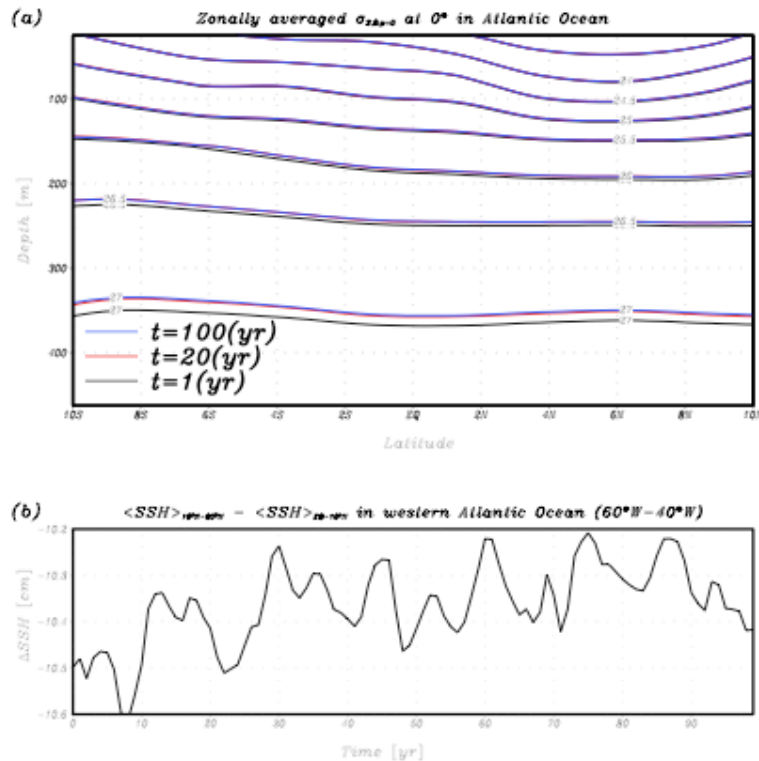


Fig. 5-10 Zonally averaged isopycnal and meridional SSH difference in the Atlantic Ocean.

following. As explained in chapter II, in low latitudes, where the Coriolis force is relatively weak, the major driving force for sustaining the teleconnection between the northward Ekman flux due to the SWWs and the NA overturning is the frictional flow near the western boundary (G99), which is driven by the meridional pressure gradient due to the north-south Sea Surface Height (SSH) difference. Figures 5-9a-c present key variables relevant to the AAIW transport for the first 100 years' simulation period under the assumption that the PSW-generated anomalous signal can propagate to the northern NA in this period (e.g. Brix and Gerdes 2003). The time series of northward velocity shows a gentle decline, meaning a decreasing AAIW transport or total amount of northward Ekman flux. Albeit this decrease, the water at that depth gradually cools from

the beginning, and starts getting fresher after 30 years, which furnishes an important clue. The following is my explanation based on the clue. The decreasing northward Ekman transport and northward intrusion of AAIW lead to the decreasing SSH and in low latitudes for the first 20 years (Fig. 5-9d), which give rise to decreases in the meridional pressure gradient in low latitudes, NA overturning and, NADW outflow. As discussed above, albeit decreases in the total amount of northward Ekman transport and the northward intrusion of AAIW, the colder and saltier water is transported northward in the Ekman layer by the PSW, which supports the first 20-year variation of $T - S$ fields at the intermediate depth showing the falling temperature and fluctuating salinity (Figs. 5-9b and 9c). Then, as the NA overturning and NADW outflow decrease, the intermediate- and deep-water not only continues to get colder but also begins getting fresher. I clarify that this explanation focuses on the remote connection between the SO winds and the NA overturning, not on the propagation time of the first 20 years. After the first 20 years, the SSH in low latitude rapidly ascends, and then remains constant at a slightly higher level than initial stage (Fig. 5-9d), which means that the NA overturning stops decreasing. As shown in Fig. 5-10a, the isopycnal depths at each time step ($t = 1^{\text{st}}, 20^{\text{th}}, 100^{\text{th}}$ year) vary with the SSH. Together with this, the time variation of the meridional SSH difference (Fig. 5-10b) supports G99, arguing about the impact of the pycnocline structure on the remote connection between the NA overturning and the NADW outflow.

Now one can reflect on how the PSW induces the uniform decrease in the volume transports of ACC in long-term baroclinic adjustment. The PSW, ultimately, plays a role in weakening the NH overturning, leading to a decreased meridional density gradient, and thus weaker thermal wind shear. The volume transport of the ACC thus decreases

consistently. The basic mechanism that explains this is consistent with the results in the previous chapter.

D. Summary

The long-term oceanic responses to the PSW were investigated in this chapter. On the one hand, the PSW did not give rise to substantial changes in the SH sea-ice – ocean interaction in contrast to the IMF experiments. Therefore, the SH overturning just passively responded to the PSW via the anomalous NA overturning. On the one hand, the PSW gave rise to changes in magnitudes of the local Ekman transport under the influence of the SSW fields. This played a role in decreasing the total amount of northward Ekman transport and the corresponding AAIW intruding low latitudes, which resulted in shoaling of isopycnals in low latitudes. As a result, the SSH in low latitudes decreases, and so does the meridional pressure gradient, the frictional current near the western boundary, the NA overturning, and the NADW outflow, the mechanism of which is in agreement with G99. As a result of the above PSW-induced decreases in the NA overturning and the NADW outflow, the ocean, in particular north of ACC, became less dense, and the meridional density gradient across the zonal band of the ACC thus decreased, leading to a consistently substantial decrease in the volume transports of ACC. This study showed that the teleconnection between the SSW fields and the NA overturning is critical under relatively weak external perturbation.

CHAPTER VI

SOUTHERN HEMISPHERE SEA-ICE – OCEAN INTERACTION AND GLOBAL
OCEAN CIRCULATION IN A WARMING CLIMATE

A. Introduction

Consistent responses of the SO sea ice to the PSW was a decreased sea ice along the coastline and in the interior pack ice, and an extension of ice coverage, all of which are basically attributed to the enhanced sea-ice divergence driven by the enhanced negative wind stress curl (see Fig. 5-2d). The first is indicative of an increased formation rate of coastal polynyas linked to near-boundary condition, while the second and third could be caused by enhanced open-ocean deep convection. Mechanisms that link anomalous wind stress to anomalous polynyas and anomalous convection were discussed in Chapter IV.

In present day climate, the presence of coastal polynyas around Antarctica has a direct and large impact on AABW formation. The Weddell Sea polynya that occurred in the 1970s is thought to have affected AABW formation through open-ocean deep convection (Gordon 1982). This implies that as the wind stress curl over the SO sea ice strengthens an open-ocean polynya and open-ocean convection could emerge and in that case exert a larger influence on the AABW formation. In the big picture, the long-term positive SAM (Hall and Visbeck 2002; and Sen Gupta and England 2006) will generate a stronger eastward component of sea-ice velocity and northward advection by Ekman

drift, which result in enhanced sea ice divergence. Therefore, in a warming world the impact of wind-driven ice divergence on the sea-ice – ocean interaction, such as positive feedbacks between coastal polynya and near-boundary convection and between open-ocean polynya and open-ocean convection, and thus AABW formation is expected to become stronger than now.

In association with the long-term positive SAM, another factor can be considered to presumably affect the sea-ice – ocean interaction. The enhanced divergent fields of the atmosphere and the ocean will increase upwelling of CDW, which will play a role in bringing more oceanic heat to the sea surface near the Antarctic continent. The influence of the anomalous oceanic heat flux is expected to be transmitted along the paths of gyre circulations surrounding the Antarctic continent. This may trigger ice melting, open-ocean polynyas, and open-ocean convection, e.g. a Weddell polynya similar to the one observed in the 1970s (Gordon 1982). When anomalous CDW reaches onto the continental shelves (Orsi et al. 1993), it can lead to an increase in coastal polynyas and an enhancement of near-boundary convection.

The long-term positive SAM can be divided into two components: “poleward shift” and “intensification” of SWW fields. Besides, the IMF is a way to provide sea ice with more atmospheric momentum stress where buoyancy-driven turbulence due to open-ocean among sea ice and/or shear-driven turbulence due to strong winds generate an unstable ASL condition. The author’s blue print that ultimately has driven the entire study presented in this thesis is illustrated in a simple schematic diagram of Fig. 6-1 showing how the atmosphere, the sea ice, and the ocean systems will interact with one another under the influence of the long-term positive SAM. The enhanced negative wind

stress curl is supposed to intensify sea ice divergence via ice advection and ice melting in regions *A* and *B*. This will be amplified by the application of the IMF. Through the widened ice-free ocean among sea ice, the enhanced surface cooling due to the ocean-to-atmosphere heat loss and the increased brine rejection due to new ice formation will act to increase the formation of dense water. This will ultimately enhance the SH overturning.

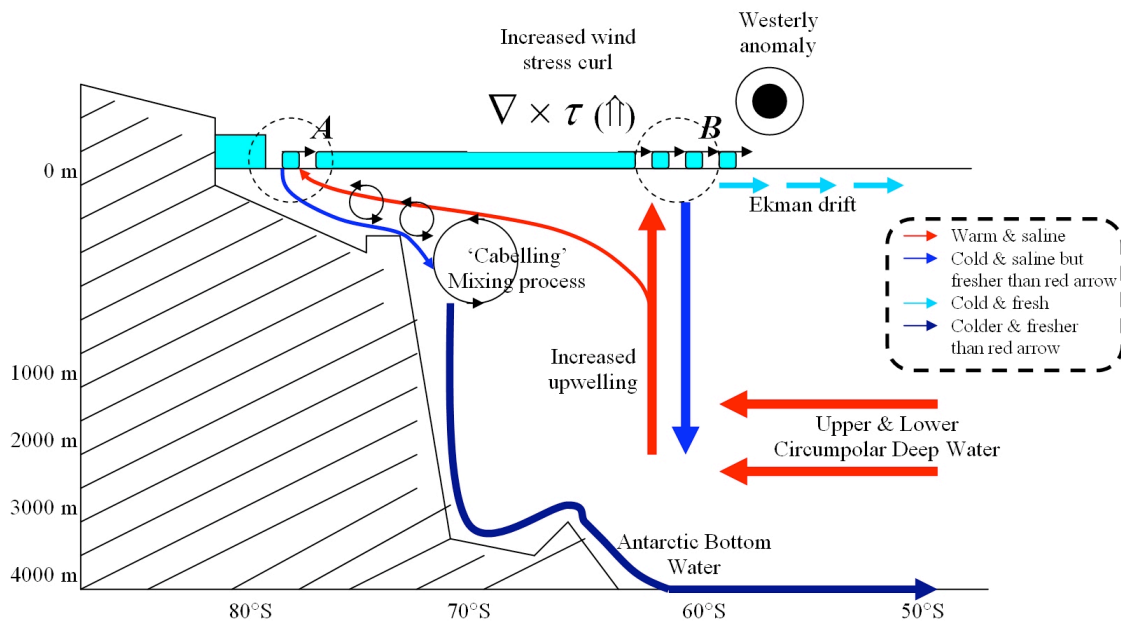


Fig. 6-1 Schematic diagram of process of the SH atmosphere – sea-ice – ocean interaction in a warming world.

Recent analyses of fully coupled climate models employing the AR4 scenario of the IPCC have shown that the SWWs are shifted poleward and intensified with increasing CO₂ emissions in the atmosphere, consistently leading to an increased volume transport of the ACC (Russell et al. 2006; Fyfe et al. 2007). While there are substantial differences in the magnitude, the high polarity of the SAM appeared to be correlated with an increase in the ACC transport (Hall and Visbeck 2002; Sen Gupta and England 2006). Besides,

many studies have shown that intensified SWWs without shift consistently increase the volume transport of the ACC in an ocean-only GCM (Gnanadesikan and Hallberg 2000) and sea-ice – ocean coupled GCM (Brix and Gerdes 2003). In the previous chapter the long-term baroclinic adjustment to PSW turned out to decrease the volume transport of the ACC, which is contrary to the short-term results of OE04. In this chapter, the mechanism that can strengthen the ACC in a warming world is investigated.

A simple description for this experimental setup follows in the next section. The SH sea-ice – ocean interaction and global ocean circulation in a warming climate are discussed in section C and D, respectively. A summary is provided in section E.

B. Experimental setup

Since all experimental frameworks (see Table 4-1) revealed similar sensitivities to IMF and PSW, respectively, only one framework EXPB is employed for the following investigation. A reference case is thus BREF. Referring to the results of climate models (Russell et al. 2006; Fyfe et al. 2007), the SWWs are shifted poleward by 5° in the same way as in the PSW-applied experiments, and are now in addition intensified by factor 1.5 (BPSW50S). BIMFPSW50S includes the application of the IMF. In another experiment (BPSWI50S), the changed wind fields of BPSW50S are applied only over sea-ice. That is, the SO sea ice is thermodynamically and dynamically forced by the changed wind fields, while the ocean is forced by the original wind fields. This experiment is designed to isolate the PSW effect on SO sea ice from that on the ocean. It should note that the

ocean is nevertheless getting affected in BPSWI50S because the changed wind fields indirectly affects the upper-layer current through the sea-ice – ocean drag.

C. SH sea-ice – ocean interaction in a warming climate

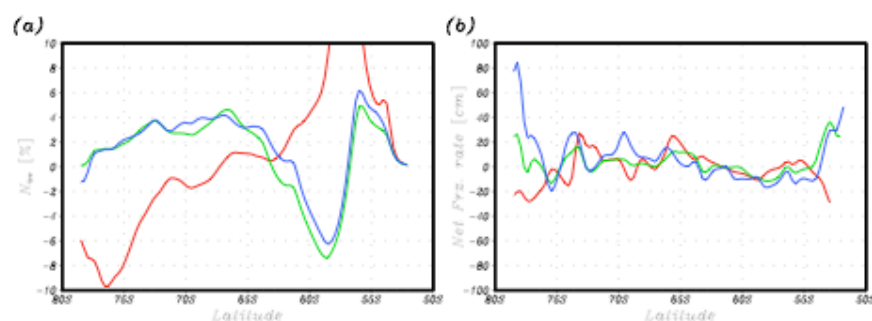


Fig. 6-2 Differences of zonally averaged winter-mean ice concentration and annual net freezing rate (BPSWI50S minus BREF: red, BPSW50S minus BREF: green, BIMFPSW50S minus BREF: blue lines).

Figure 6-2 shows the zonally averaged differences of the BPSWI50S, BPSW50S, and BIMFPSW50S minus BPSW for the winter-mean ice concentration and the annual net freezing rate. Same as Fig. 4-3a and 5-3a, the calculated ice concentration is the one before the thermodynamic process. BPSWI50S shows the largest decrease in zonal-mean ice concentration near the Antarctic continent, while BPSW50W does not show any distinct decrease in ice along the coastline. A noticeable thing is that in BPSWI50S the largest ice reduction is far from leading to the largest net freezing rate, leads to a decrease in net freezing rate, and besides in BPSW50W it reaches up to 20 *cm* near 78°S. On the other hand, in comparison to BPSW50S, the application of IMF gives rise to an additional ice reduction near 78°S and 70°S in BIMFPSW50S, thus leading to a substantial increase in net freezing rates. Intuitively, one can see that the inconsistency between the zonal mean ice concentration anomaly and the zonal mean net freezing rate

anomaly shown in BPSWI50S and BPSW50S is attributed to regional difference of sea-ice response.

Figure 6-3 shows changes of winter mean ice concentration and thickness for respective sensitivity experiments. Common responses between BPSWI50S and BPSW50S are ice reductions in the eastern Weddell gyre near Maud Rise, in the west of Kerguelen Plateau, and in most areas along the coastline. Such responses are indicative of the dominance of wind-driven sea-ice divergence in those regions. In comparison to BPSWI50S, BPSW50S shows three noticeable differences: 1) decreased sea ice east of the Antarctic Peninsula, 2) decreased sea ice from the east of Kerguelen Plateau to Adélie coast, and 3) increased sea ice in the Ross Sea. Major factors that could drive these differences are presumed to be the aforementioned anomalous upward oceanic heat flux and anomalous gyre circulations, the latter of which not only supply the ocean with an anomalous oceanic drag force but also bring anomalous heat originating from the NADW south of the ACC. The effect of anomalous influx of heat due to gyre circulation will be combined with the effect of anomalous upward heat flux due to upwelling to accelerate the process of ice melting. The similarity of the response pattern of BPSW50S and BIMFPSW50S shows that IMF only has an impact on the response magnitude, while the difference of the response pattern of BPSWI50S relation to the other two experiments indicates that the altered wind forcing over the entire SO sets the stage for major redistributions of the large-scale circulation. This is supported with Figs. 6-4a-4c showing annual mean SSH anomalies for the respective experiments. In the reference experiment, the SSH in the SO is mostly lower than -100 m , the SSH gets lowered as it approaches the coast, and several low pressure cores are located around the Antarctic

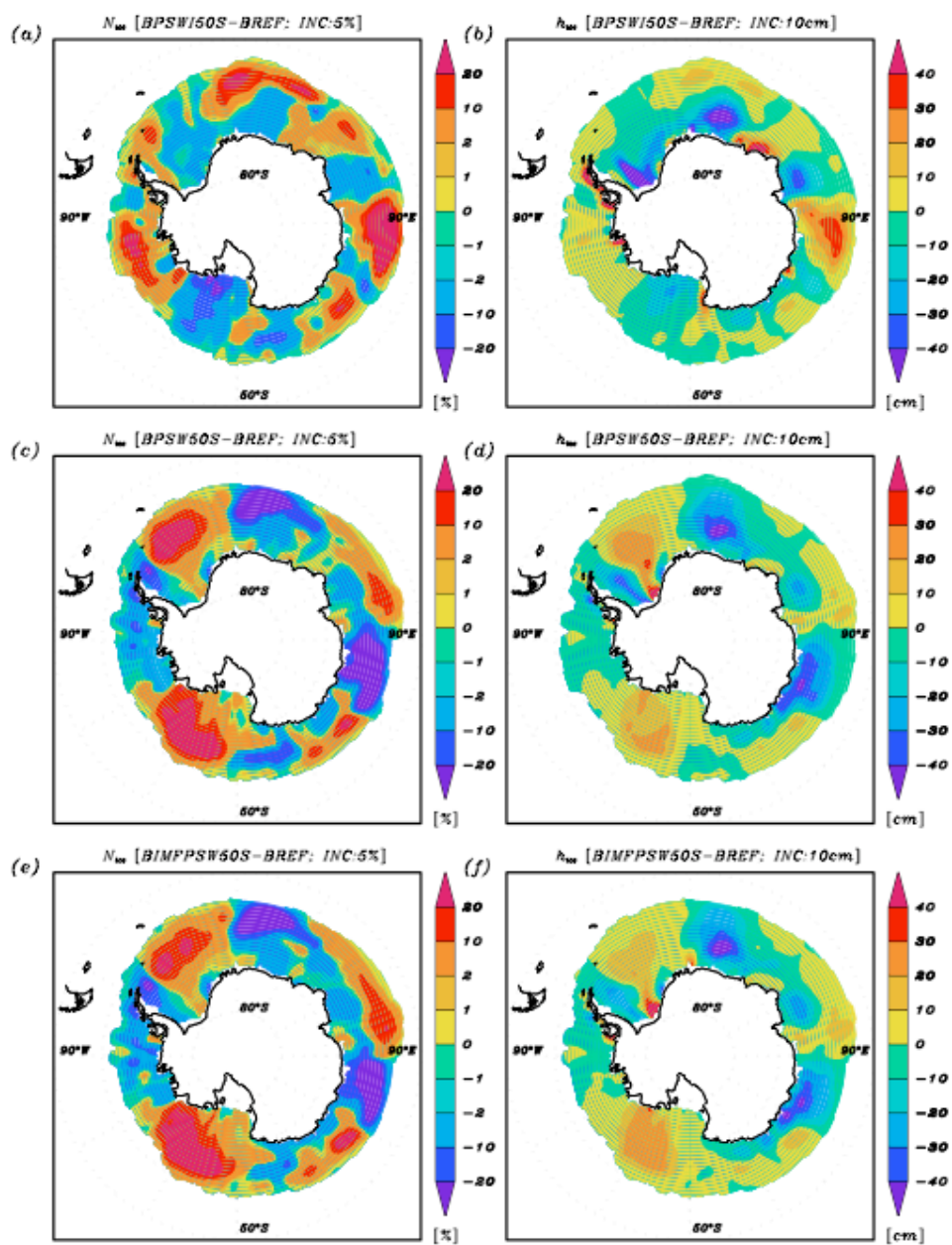


Fig. 6-3 Differences of winter-mean ice concentration and thickness.

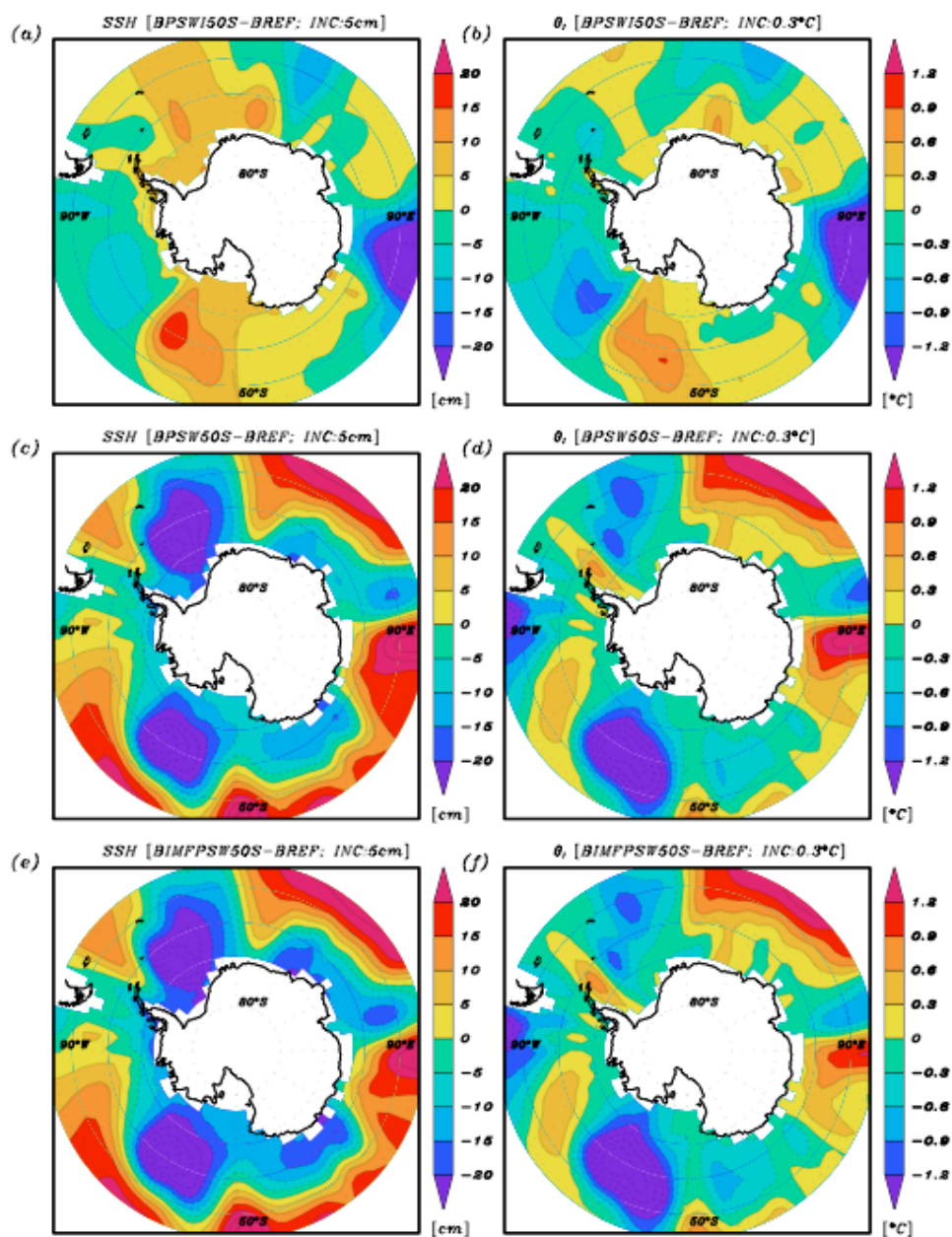


Fig. 6-4 Differences of annual-mean SSH and potential temperature averaged from surface to intermediate depth (θ ; 712.5 m).

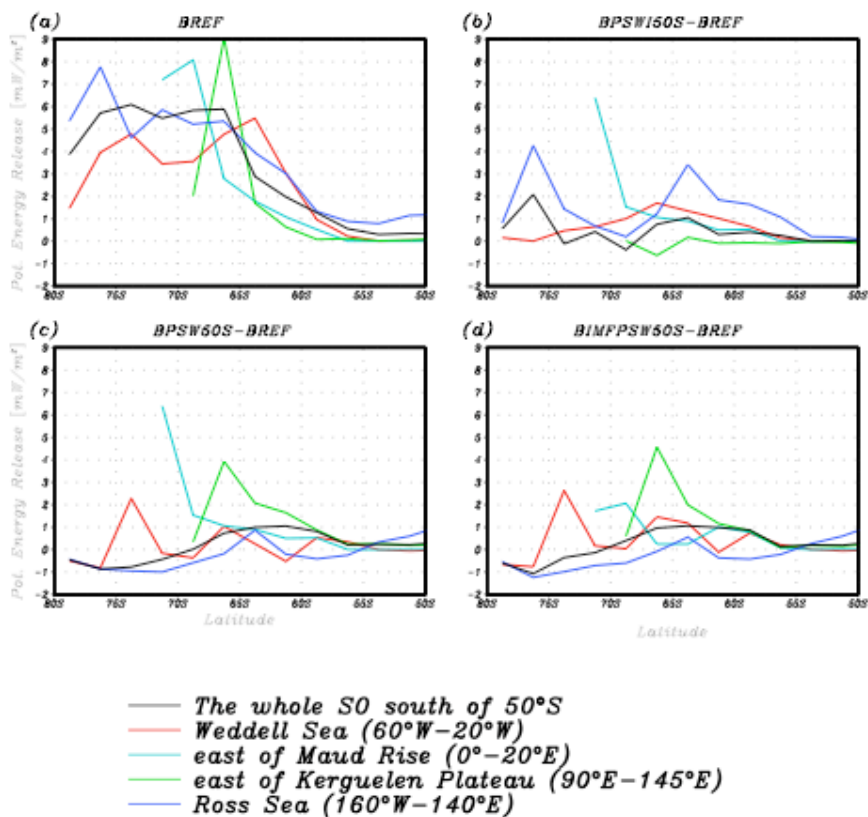


Fig. 6-5 Zonally averaged annual-mean convective potential energy release.

continent (not shown here), which mainly drive cyclonic gyre circulation through the geostrophic balance. Thus, a decreased (increased) SSH is indicative of an enhanced (weakened) cyclonic gyre circulation. The pattern of SSH anomalies is rather consistent with the anomalous potential temperature fields averaged from surface to the intermediate water depth ($\sim 700\text{ m}$), as shown in Figs. 6-4d-4e. Areas that indicate an enhanced (weakened) gyre circulation also show a cooling (warming) of intermediate water, which to some extent coincides with the pattern of increased (decreased) sea ice.

Now I turn to question on how the sea-ice anomalies affect convection in the SO? Fig. 6-5a shows zonally averaged annual-mean potential energy release due to convection

along selected longitudinal sections for reference experiment BREF, and convection anomalies for the respective sensitivity experiments. Most selected sites, as well as the whole SO, show strong convection south of 65°S . In BPSWI50S, convection has become substantially stronger in the Ross Sea and east of Maud Rise, and strengthened slightly off the coast of the Weddell Sea, which are consistent with where reductions of sea ice occurred (Figs. 6-3a and 3b). East of Kerguelen Plateau where sea ice increased, convection has been slightly weakened. As a result of the wind-driven sea-ice divergence in BPSWI50S, the SO convection as a whole shows an increase in both near-boundary convection and open-ocean convection. On the contrary, in BPSW50S, convection in the Ross Sea decreased, while convection in the Weddell Sea, the east of Maud Rise, the east of Kerguelen Plateau increased, all of which is consistent with the pattern of sea-ice anomalies (Figs. 6-3c and 3d). East of Maud Rise where sea ice decreases in both BPSWI50S and BPSW50S, convection consistently increased. As a whole, in comparison to the reference case, in BPSW50S, the zonal mean convection around 75°S , indicative of near-boundary convection, has decreased, while that between 65°S and 58°S , indicative of open-ocean convection, has increased. On the other hand, in the Weddell Sea, at 73°S convection has increased, in contrast to the zonal mean value. It indicates enhanced near-boundary convection along the Antarctic peninsular, where sea ice has consistently decreased. Therefore, one can say that both types of convection will increase along with the poleward-intensified SWW fields. The application of IMF appears to increase convection only slightly.

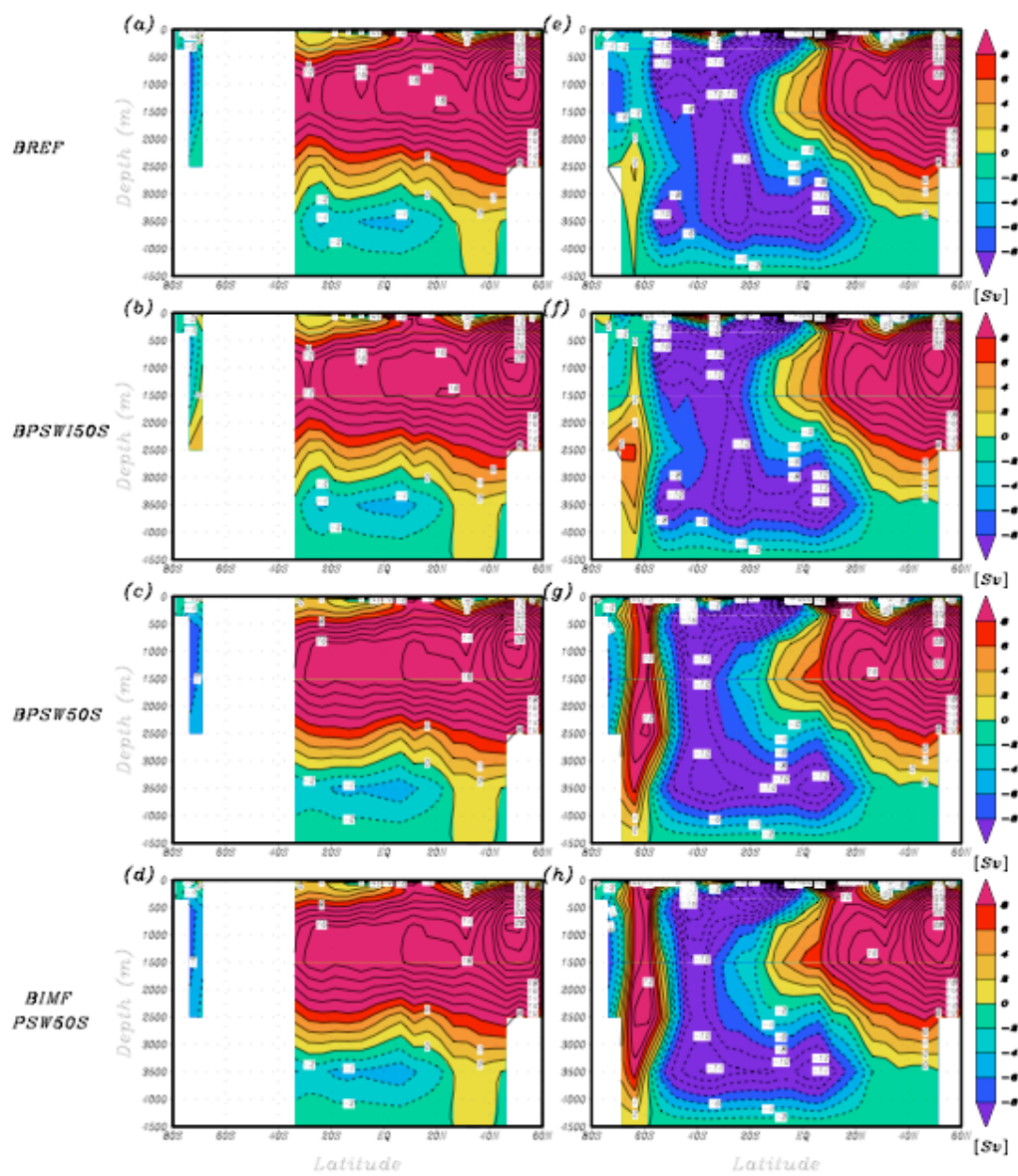


Fig. 6-6 Meridional overturning circulations in the Atlantic and Global Ocean.

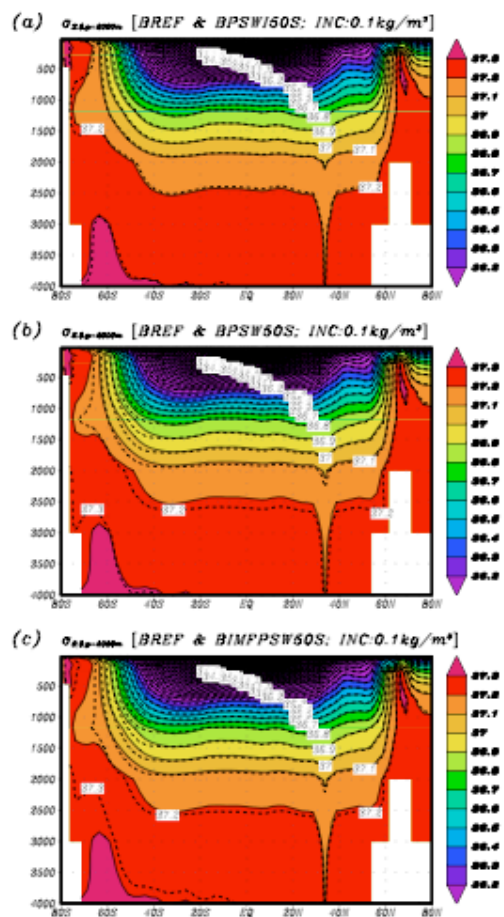


Fig. 6-7 Zonally averaged global density fields ($\sigma_{s,\theta,p=2000m}$) fields.

D. Global ocean circulation in a warming climate

Table 6-1. As in Table 4-2 but for the comparison of BREF with the BPSWI50S, BPSW50S, and BIMFPSW50S (abbreviations explained in text).

	BREF	BPSWI50S	BPSW50S	BIMFPSW50S
$\theta_{z=4000m}$ [°C]	0.97	0.98	1.12	1.07
$S_{z=4000m}$ [psu]	34.678	34.680	34.697	34.702
NA overturning	28.6	28.2	28.6	28.6
NADW outflow	12.3	12.0	16.7	16.8
ACC	99.9	94.7	116.7	121.5

Fig. 6-6 shows meridional overturning circulations in the Atlantic and the global Ocean for all experiments dealt with in this chapter. As discussed earlier, a central issue is the anti-correlation between the North Atlantic overturning and the Atlantic division of the SH overturning. Even with the effect of anomalous wind-driven sea-ice divergence, sea ice in BPSWI50S appears to decrease in most coastal areas, in the Ross Sea, and in parts of interior pack ice, leading to an increase in convection and dense water formation. The Atlantic bottom cell overturning slightly expanded upward, and thus the NA overturning cell slightly shrank. As presented in Table 6-1, while there are no distinct changes in deep-water temperature and salinity at 4000 *m*, the NA overturning and NADW outflow slightly decreased. The maximum transport of the global bottom cell overturning north of equator increased by about 2 *Sv*, as indicated by the comparison of Figs. 6-6e and 6f. As shown in Fig. 6-7a, deep water has become slightly denser, and inclinations of isopycnals at latitude band of Drake Passage has become less steep, leading to a decrease in the volume transport of the ACC (Table 6-1). Moreover, the relatively more weakly stratified water column south of 60°S denotes the results of strong convection (Fig. 6-5b).

In previous chapters, the effect of IMF over sea ice appeared to enhance the SH overturning, counteracting the NH overturning, and moreover the PSW appeared to trigger both a weakening the NH overturning and an expansion and/or enhancement of the SH overturning. Albeit without change in the maximum transport of the NA overturning, BPSW50S shows a substantial increase in the NADW outflow (Fig. 6-6c and Table 6-1), concomitant with shrinkage of the Atlantic bottom cell. Consistent with increased near-boundary convection in the Weddell Sea, the intrusion of AABW into the Atlantic increased, while that of the globe (Fig. 6-6g) decreased, compared to the reference case (Fig. 6-6e), along with the decreased near-boundary convection in the whole SO. The most noticeable difference in Fig. 6-6g versus Fig. 6-6e is a substantial increase in the Deacon cell overturning. It can be interpreted that two causes operate on this. On the one hand, the enhanced upwelling and open-ocean convection could be responsible for this. It is possible because the Deacon cell overturning in BIMFPSW50S where open-ocean convection was slightly enhanced (Fig. 6-4d) also slightly increased. On the other hand, an excessively increased northward Ekman transport of colder water is likely to enhance convection in the formation regions to increase the Deacon cell overturning in contrast to the pure PSW case, anomalous response signal was transmitted to the northern NH to increase the NA overturning. This is somewhat consistent with the aforementioned argument of RE97. Therefore, the increased NADW outflow could be influenced by the increased Deacon cell overturning, and not by the expanded NA overturning. The increased NADW outflow, as well as the enhanced open-ocean convection, not only render the global deep ocean warmer and saltier (Table 6-1) but also increased the meridional density gradient between 60°S and 40°S (Fig. 6-7b), the latter of

which finally leading to a substantially increased volume transport of the ACC (Table 6-1).

As discussed earlier, convection in BIMFPSW50S is slightly stronger than in BPSW50S, rendering the global deep ocean somewhat colder and saltier than in BPSW50S (Table 6-1). While the NH overturning including the NA overturning and the NADW outflow remained unchanged (Table 6-1 and Figs. 6-6d and 6h), this increased dense water increased the SH overturning (Fig. 6-6h), and made the SO water south of 50°S denser (Fig. 6-7c), which increased the ACC even further.

E. Summary

Using the experimental framework of EXPB as a reference case, the impact of poleward-shifted and intensified SWW fields on the sea-ice – ocean interaction and the global ocean circulation has been studied in this chapter. Along with this, the additional effect of the IMF has been assessed. The SO sea-ice system appeared to be perturbed not only by the anomalous wind-driven sea-ice divergence but also by wind-driven anomalous oceanic heat flux determined by enhanced upwelling and change in the gyre circulations around the Antarctic continent, leading to distinct change in the strength and patterns of convection in the SO. Inconsistent with the results of the PSW, the poleward-shifted and intensified SWW fields (in case of BPSW50S) did not decrease the NA overturning and NADW outflow, but instead gave rise to substantial increases in the Deacon cell overturning and the NADW outflow, while the NA overturning remained unchanged. Enhanced convection due to the substantially increased northward Ekman

transport of cold water, as well as the increased upwelling south of the ACC constitutes the driving mechanism for the increased Deacon cell. The influence of enhanced SO convection also increased the bottom cell overturning, though without diminishing the NADW outflow. Consistent with the previous study in chapter IV, the application of IMF (in case of BIMFPSW50S) amplified the SH overturning. The ACC increased with the poleward-intensified SWW fields, and moreover the application of IMF amplified the increase of the ACC. The responses explained in this chapter provide an explanation for why the simulated results from coupled climate models with the AR4 scenario have consistently shown an increased ACC. These models not only implicitly include the IMF but also provide the ocean with poleward-shifted SWW that are intensified (e.g. Hall and Visbeck 2002; Sen Gupta and England 2006; Russell et al. 2006; Fyfe et al. 2007). To sum up, the anomalous SWW fields provide the ocean circulation system with two competing climatic signals, i.e. one with direct impact on the NA overturning and the other along the SH overturning.

CHAPTER VII

FINAL DISCUSSION AND CONCLUSIONS

This study began with a question on the linkage between the SO winds and the global ocean circulation. This linkage is composed of two processes. First, the SO winds determine the northward transport of the cold AASW in the Ekman layer, which affects both the Deacon cell overturning and the NH overturning, in particular the NA overturning and NADW outflow. As illustrated in Fig. 2-2, this process indicates connections between *A*, *B*, *C*, and *D*. Second, the SO winds play an important role in the SH sea-ice – ocean interaction, which affect the SH overturning, consisting of the Antarctic cell overturning and the bottom cell overturning. This process involves a connection between *A* and *E*, which includes the sea-ice – ocean interaction processes, as illustrated in Fig. 6-1. Therefore, the anomalous SO winds can synchronously generate climate signals that propagate in two directions: 1) *A* to *B* (hereafter denoted as PCSI) and 2) *A* to the SH sea-ice – ocean interaction (hereafter denoted as PCSII). Then, resultant interhemispheric changes in meridional overturning circulations set long-term baroclinic mean transports, which determine the thermodynamic balance involved in the transport of the ACC. On the other hand, in the framework of an ocean GCM coupled to a sea-ice model, the IMF plays an important role in amplifying the PCSII. Several little clues for the above puzzle were found throughout this study, and these are critically discussed in detail below.

A. Interactive momentum flux over the SO sea ice

The wind-driven sea-ice motion plays an important role in ocean ventilation by way of controlling where and how much thermohaline fluxes are provided to the ocean. The way the momentum flux is modified by simulated sea ice, in particular its sub-grid heterogeneity, has been applied to the sea-ice model coupled to a global ocean GCM in order to provide sea-ice dynamics with physically more reasonable atmospheric momentum stress. In contrast to the usual approach of having the momentum flux just depend on the wind speed and a constant drag coefficient, the newly introduced momentum flux driving sea ice considers the local stratification and roughness over ice in one case, and the flux-aggregated stratification and roughness using the blending-height concept in the other case. While both cases thus allow for an interactive feedback, only the latter case accounts for the sub-grid scale heterogeneity of the sea-ice pack. In particular, the sea-ice feedback is in the former case only provided by the simulated ice thickness, affecting the surface temperature and local stratification, while in the latter case it is also determined by the ice concentration.

Both parameterizations yield predominantly statically stable, but dynamically unstable conditions at any instant over the wintertime sea-ice pack. On the seasonal mean, statically and dynamically unstable conditions prevail over coastal polynyas, and lead to a positive feedback with increased momentum flux. The larger momentum flux enhances the along and offshore ice drift, leading to corresponding changes in the seasonal mean ice thickness distribution, a reduction in coastal ice concentration, and an increase of heat loss due to sensible heat flux. In the case where surface heterogeneity is

accounted for, the impact of the lower coastal ice concentration leads to a larger momentum flux than in the homogeneous case. The long-term deep-ocean properties are only affected when in the heterogeneous case the form drag is raised by increasing the ice freeboard and decreasing the maximum ice concentration. Only the combination of both yields a significant increase of Antarctic Bottom Water formation, as reflected by a long-term cooling and freshening of the global deep-ocean properties.

B. Oceanic response to anomalous SO winds via the sea-ice – ocean interaction

The near-boundary convection associated with coastal polynyas, as well as the open-ocean convection associated with open-ocean polynyas, play a key role in generating the PCSII perturbing the SH overturning. When the SWWs shift poleward and intensify (e.g. experiment BPSW50S), these two types of convection are enhanced by both the wind-driven sea-ice divergence anomaly and the wind-driven oceanic heat flux anomaly. The former is influenced by the wind stress curl anomaly over sea ice, while the latter is influenced by the upward heat flux anomaly due to upwelling and anomalous southward influx of heat from the northern flank of ACC due to the gyre circulation. Therefore, the PCSII perturbed by the poleward shifted and intensified SWW fields is transmitted to the global ocean to expand and/or strengthen (weaken) the SH overturning (the NH overturning).

On the other hand, the IMF-induced positive feedback consistently increases the formation rate of polynyas and enhances convection, in particular near-boundary convection, which gives meaning to both sea-ice – ocean coupled GCMs and fully

coupled GCMs. Without the application of the IMF, sea-ice – ocean coupled GCMs may reproduce weaker ocean ventilation in SO. In fully coupled GCMs, the atmosphere system and the sea-ice system interact with each other, implying that effects of the IMF-induced positive feedback are included. Moreover, it is presumed that this feedback is somewhat augmented by virtue of the interactively responding atmosphere system. This is discussed again in conjunction with the ACC in section D.

The aforementioned oceanic heat flux anomaly is considered to generate the positive feedback leading to more polynyas and convection, but it must be noted that this positive feedback can also be broken down by an excessive oceanic heat flux, which suppresses convection because an excessive fresh water flux due to ice melting will act to stabilize the water column. Thereby, the sea-ice – ocean interaction diminishes, and so do the formation of AABW and the SH overturning. Besides, the ice shelf melting process, which contributes to stabilizing the water column (e.g. Hellmer 2004), has been excluded in the reference experiments. Therefore, an idea about the PCSII is still in need of further investigations.

C. Oceanic response to the anomalous SO winds via the northward Ekman transport

The anomalous SWWs have a direct influence on the total amount as well as the $T - S$ properties of water transported northward in the Ekman layer, which generate the PCSI loop. First, when the SWWs were just shifted poleward (the PSW-applied experiments in Chapter V), colder water was pushed north in the Ekman layer, and the total amount of northward Ekman transport decreased, which resulted in a decrease and a

cooling of the water flowing into low latitudes along the pycnocline. It influenced the pycnocline depth in low latitudes, leading to a meridional pressure gradient anomaly in the tropical Atlantic. A decreased meridional pressure gradient acted to decrease the frictional current near the western boundary from low latitudes to high latitudes to weaken the NA overturning and decrease the NADW outflow. This explanation follows the arguments of G99. Second, when the SWWs are shifted poleward by 5° and intensified by 50% (BPSW50S experiment in Chapter VI), a larger amount of colder waters pushed north in the Ekman layer causes a larger amount of net buoyancy loss at the northern flank of ACC. Albeit any distinct convection has not been found north of the ACC under the present-day climatic condition, the net buoyancy loss anomaly may give rise to convection there, and thus enhance the Deacon cell overturning along with an increased upwelling south of the ACC. Although the NA overturning remained unchanged, the NADW outflow substantially increased (Table 6-1), which can be explained in two ways. First, according to Hallberg and Gnanadesikan (2006), increased SWWs (by 20%) amplify the deep-to-intermediate cell denoting that the dense NADW outflow and CDW upwell into the mixed layer, and are transformed into the lighter AAIW in the framework of a hemispheric ocean model for the SH. It means that, for the amplifying deep-to-intermediate cell, the NA overturning does not play a roll. Here, I presume that the enhanced Deacon cell overturning affects the deep-to-intermediate cell to increase the NADW outflow. Second, the enhanced Deacon cell overturning acts to suppress the SH overturning associated with AABW formation, leading to an increase in NADW outflow. To sum up, in the former case (PSW-applied cases) the PCSI was transmitted to the northern NA to change the NA overturning, while in the latter case

(BPSW50S) the PCSI was disconnected by the Deacon cell and thus was not transmitted to the northern NA. This difference is presumed to be attributable to the convection due to the net buoyancy loss anomaly in the AAIW formation region (e.g. Ribbe 1999; Sørensen et al. 2001), as well as atmospheric momentum torque.

Not only TS93 and TS95 but also RE97 showed a distinct increase in the NA overturning with 50% intensified SWW fields, while the PSW50S experiment did not give rise to any change in the NA overturning. Instead, the Deacon cell and the NADW outflow substantially increased in PSW50S. This difference was, at first, presumed to be attributable to the poleward shifted SWW fields driving an additional net buoyancy loss via the “colder” water transported northward in the Ekman layer. However, a test experiment (not shown here), in which the SWW fields are not shifted poleward but intensified by 50% following TS93, TS95, and RE97, reveals the same magnitude responses in the NA overturning, the NADW outflow, and the Deacon cell as PSW50S did. What produces this difference is still unclear, so the idea about the remote connection between the PCSI and the NA overturning needs further investigation.

Another doubtful point is the process that the anomalous AAIW-induced SSH anomaly at low latitudes affects the meridional pressure gradient and thus the frictional current near the western boundary in the NA between low latitudes and mid latitudes, albeit it was explored in chapter V on the basis of the argument of G99. This process depends on the amount of the anomalous influx of cold water transported from the SH to the pycnocline in low latitudes. This influx can affect the annual variation of the equatorial cold tongue of SST just south of the Equator, leading to the cross-equatorial SST gradient anomaly. This, according to Chang et al. (1997), will affect the wind fields

over the tropical Atlantic Ocean via thermodynamic air-sea interactions, and then upper-ocean currents including the western boundary current. Therefore, this process also needs further investigation with the consideration of air-sea interactions.

D. Long-term baroclinic adjustment of the ACC to the anomalous SO winds

Gnanadesikan and Hallberg (2000) argued that, in an ocean GCM with restoring surface conditions, the baroclinic part of the ACC depends directly on the winds within Drake Passage because it, in order, determines the conversion rate of the dense CDW to the lighter AAIW, the pycnocline depth in low latitudes, the overturning in the NH, the conversion rate of light water (back) to the NADW, the meridional density gradient across the ACC, the thermal wind shear, and finally the strength of the ACC. Among their arguments, the concept that the thermal wind shear associated with the meridional density gradient in the zonal band of the ACC plays a key role in the long-term baroclinic adjustment of the ACC was adopted in this study. Until now, the anomalous SO winds have been summarized to affect 1) the SH sea-ice – ocean interaction and 2) the amount of cold water transported northward in the Ekman layer. In the former case, the active SH sea-ice – ocean interaction, i.e. an enhanced convection associated with the anomalous SO winds increasing the formation rate of polynyas, acts to increase the formation rate of AABW and to intensify the influence of the SH overturning, which, reversely, weakens the NA overturning and reduces the NADW outflow. As a result, the ocean south (north) of the zonal band of the ACC becomes denser (lighter), leading to an increase in the meridional density gradient, and thus the baroclinic part of the ACC. In the latter case,

regardless of whether the remote connection between the SO winds and the NA overturning is on or off, the anomalous amount of cold water transported northward in the Ekman layer has a critical influence on the NADW outflow. As a result, an increased (decreased) NADW outflow makes the ocean north of the zonal band of the ACC lighter (denser), leading to an increase (decrease) in the meridional density gradient, and thus the baroclinic part of the ACC. According to the conclusion of Gent et al. (2001), when the model formulation and parameter values are fixed, the Drake Passage transport (i.e. the ACC) is set by two external forcing factors: 1) the strength of the thermohaline circulation off the Antarctic shelf and 2) the strength of the meridional Ekman transport at the latitudes of Drake Passage, both of which are exactly consistent with the detailed conclusion proposed above.

Previously in section B, fully coupled GCMs were argued to explicitly include the IMF-induced effects affecting polynyas, convection, and ventilation in the SO. Most fully coupled GCMs show that, as the amount of CO₂ in the atmosphere increase up to double the present-day concentration, the SWWs are shifted poleward and intensified, consistently leading to an increase in the volume transport of the ACC (e.g. Russell et al. 2006; Fyfe et al. 2007). The results that the application of the IMF consistently increased the volume transport of the ACC (see Table 4-2 and Table 6-1) seems to support why most fully coupled GCMs show an increased ACC in response to the poleward shifted and intensified SWWs.

E. Deficient baroclinic effects of mesoscale eddies

The ACC is not a channel flow, but a meandering flow, which is full of mesoscale eddies (refer to Fig. 5 and 6 in Hallberg and Gnanadesikan 2006). Albeit eddy activity is found to be vivid along western boundaries of all continents, the tropics between 10°S and 10°N , the northern NA, the Arctic marginal sea, and the thick zonal band of the ACC, the primary region is that of the ACC, where the eddy-induced transport is a maximum because the largest gradients of temperature and salinity at 500 m in the world's oceans occur in this region (Gent et al. 2002). The scheme described by Gent and McWilliams (1990, hereafter denoted as GM90) and its improved versions (Gent et al. 1995; Visbeck et al. 1997) have been utilized in coarse-resolution ocean GCMs to represent adiabatic transport effects of baroclinic eddies. Moreover, it is another way to go toward a high-resolution model being able to explicitly capture mesoscale eddies (e.g. Hallberg and Gnanadeskan 2001, 2006), which however has a major shortcoming of being too expensive to integrate for very long periods in order to study long-term deep-ocean responses.

Mesoscale eddies play an important role in energy dissipation, so the potential energy of the global ocean could be overestimated in ocean GCMs when the effects of these mesoscale processes are not properly taken into account. Gent et al. (1995) showed that the eddy-induced circulation simulates baroclinic instability by flattening the model isopycnals and reducing the potential energy. Moreover, doubling the isopycnal diffusivity coefficient up to $1600\text{ m}^2\text{ s}^{-1}$ indicative of an enhanced eddy activity appeared to result in a significant decrease in the ACC because this enhanced eddy activity

accelerates the meridional water mass flux in the upper layer, i.e. increasing southward influx of warm water and northward influx of cold water via isopycnal mixing by mesoscale eddies, and thus decreases the meridional density gradient and the corresponding thermal wind shear (Gent et al. 2001). This is well supported by Fig. 5 of Gent et al. (2002) showing that an enhanced eddy activity based on the modified GM90 scheme (Visbeck et al. 1997) cools (warms) upper-ocean water ($\sim 520\text{ m}$) in the southern (northern) flank of the ACC in the Pacific (Atlantic). On the other hand, using a high-resolution ($1/6^\circ$) eddy-permitting hemispheric isopycnal-coordinate model, Hallberg and Gnanadesikan (2006) showed that explicitly resolved eddies play a role in extending the surface-to-intermediate water cell converting the warm, salty Subtropical Water (STW) into the cold, fresh Subantarctic Mode Water (SAMW) farther southward by hundreds of kilometers. It implies a significantly greater poleward heat transport, and is functionally in line with meridional distribution of water mass accelerated by the enhanced eddy activity. Another noticeable issue was that resolving eddies appeared to attenuate responses of the ACC to changes in wind stress. It also appeared to attenuate the response of the overturning circulation to the wind stress anomaly, which is attributed to the aforementioned meridional water mass flux accelerated by the enhanced eddy activity because it reduces the net buoyancy loss anomaly known to be a major driving force for the meridional overturning circulation in the region of ACC together with atmospheric momentum torque (refer to Marshall and Radko 2003).

The previous two paragraphs summarized how well resolved mesoscale eddies in the region of the ACC can change the sensitivity of the ocean circulation to change in external forcing. Then, how is this applied to the conclusions presented in the previous

four sections? In a coarse-resolution ocean GCM used in this study, the effects of mesoscale processes are taken into account implicitly by parameterizing subgrid-scale mixing of momentum and tracers according to K-theory (refer to Appendix I.A). Then, to what part of my conclusions should I throw more doubt, and on what part of my conclusions could I put more reliance? Most doubtful points arise from what the PCSI results in. Baroclinic eddies play an important role in redistributing buoyancy in the mixed layer, which, as argued by Marshall and Radko (2003), affects the meridional overturning circulation, surface convergence occurring where the AAIW and SAMW meet, and subduction. In the results presented here, poorly redistributed buoyancy due to unresolved mesoscale eddies is suspected to give rise to an excessive buoyancy loss anomaly along the northern flank of the ACC, and thus an overestimated increase of the Deacon cell, which was suspected to cut off the PCSI. Therefore, I presume that, if the effects of mesoscale eddies were well taken into account, the responses of the Deacon cell overturning in the BPSW50S and BIMFPSW50S would not be as strong as shown in Figs. 6-6g and 6h, and thus the NA overturning would substantially increase. Finally, this would increase the ACC more via the long-term baroclinic adjustment. However, there would be, simultaneously, a counteraction that decreases the ACC by way of flattening the isopycnals as pointed out in Gent et al. (2001). To conclude, in using non-eddy resolving coarse-resolution ocean GCMs, caution is required when interpreting the impact of the PCSI on the global ocean circulation, while responses of the global ocean circulation to the PCSII seem to be free from the burden associated with the baroclinic effects of mesoscale eddies not being resolved.

REFERENCES

- Alam, A. and Curry, J. A., 1997: Determination of surface turbulent fluxes over leads in Arctic sea ice. *J. Geophys. Res.*, **102**, 3331-3344.
- Andreas, E. L., Tucker, W.B. and Ackley, S.F., 1984: Atmospheric boundary-layer modification, drag coefficient, and surface heat flux in the Antarctic marginal ice zone. *J. Geophys. Res.*, **89**, 649-661.
- Andreas, E. L., and K. J. Claffey, 1995: Air-ice drag coefficient in the western Weddell Sea 1. Values deduced from profile measurements, *J. Geophys. Res.*, **100(C3)**, 4821-4831.
- Andreas, E.L., Jordan, R.E., and, Makshtas, A.P., 2005: Parameterizing turbulent exchange over sea ice: the ice station Weddell results. *Bound.-Layer Meteorol.*, **114**, 439-460.
- Antonov, J. I., R. A. Locarnini, T. P. Boyer, A. V. Mishonov, and H. E. Garcia, 2006: *World Ocean Atlas 2005*, Volume 2: Salinity. S. Levitus, Ed. NOAA Atlas NESDIS 62, U.S. Gov. Printing Office, Washington, DC, 182pp.
- Arakawa, A., and V. R. Lamb, 1977: Computational design of the basic dynamical process of the UCLA general circulation model, *Methods Comput. Phys.*, **17**, 173-265.
- Arya, S. P. S., 1973: Contribution of form drag on pressure ridges to the air stress on Arctic ice. *J. Geophys. Res.*, **78**, 7092-7099.
- Arya, S. P. S., 1975: A drag partition theory for determining the large-scale roughness parameter and wind stress on the Arctic pack ice. *J. Geophys. Res.*, **80**, 3447-3454.
- Arya, S. P., 1999: *Air Pollution Meteorology and Dispersion*. Oxford University Press, Chapter 4, 77-104.
- Bailey D. A., A. H. Lynch, and T. E. Arbetter, 2004: Relationship between synoptic forcing and polynya formation in the Cosmonaut Sea: 2. Regional climate model simulations. *J. Geophys. Res.*, **109**, C04023, doi:10.1029/2003JC001838.
- Bindoff, N. L., and T. J. McDougall, 1994: Diagnosing climate change and ocean ventilation using hydrographic data. *J. Phys. Oceanogr.*, **24**, 1137-1152.
- Birnbaum, G., and Lüpkes, C., 2002: A new parameterization of surface drag in the marginal sea ice zone. *Tellus*, **54A(1)**, 107-123.
- Bitz, C. M., Holland, M.M., Hunke, E.C., and Moritz, R.E., 2005: Maintenance of the sea-ice edge. *J. Climate*, **18**, 2903-2921.

- Brix, H., and R. Gerdes, 2003: North Atlantic Deep Water and Antarctic Bottom Water: Their interaction and influence on the variability of the global ocean circulation. *J. Geophys. Res.*, **108** (C2), 3022, doi:10.1029/2002JC001335.
- Brutsaert, W., 1979: Heat and mass transfer to and from surfaces with dense vegetation or similar permeable roughness. *Bound.-Layer Meteor.*, **16**, 365-388.
- Broecker, W. S., 1987: The great ocean conveyor, *Oceanography*, **4**, 35-40.
- Broecker, W. S., 1998: Paleocean circulation during the last deglaciation: A bipolar seesaw?. *Paleoceanography*, **13**, 110-121.
- Chang, P., and L. Ji, and H. Li, 1997: A decadal climate variation in the tropical Atlantic Ocean from thermodynamic air-sea interactions. *Nature*, **385**, 516-518.
- Claussen, M., 1990: Area-averaging of surface fluxes in a neutrally stratified, horizontally inhomogeneous atmospheric boundary layer, *Atmos. Environ.*, **24A**, 1349-1360.
- Claussen, M., 1991a: Local advection processes in the surface layer of the marginal ice zone, *Boundary-Layer Meteorol.*, **54**, 1-27.
- Claussen, M., 1991b: Estimation of areally-averaged surface fluxes, *Boundary-Layer Meteorol.*, **54**, 387-410.
- Claussen, M., 1992: Scale aggregation in semi-smooth flow, Max-Planck-Institute für Meteorologie, Report No 87, Hamburg.
- Claussen, M., 1995: Flux aggregation at large scales: on the limits of validity of the concept of blending height, *J. Hydrol.*, **166**, 371-382.
- Connolley, W.M. and Harangozo, S.A., 2001: A comparison of five numerical weather prediction analysis climatologies in southern high latitudes. *J. Climate*, **14**, 30-44.
- Codron, F., 2005: Relation between annular modes and the mean state: Southern Hemisphere summer. *J. Climate*, **18**, 320-330.
- Cotton, J. H., and K. J. Michael, 1994: The monitoring of katabatic wind-coastal polynya interaction using AVHRR imagery, *Antarct. Sci.*, **6(4)**, 537-540.
- de Boer, A. M., J. R. Toggweiler, and D. M. Sigman, 2007: Atlantic dominance of the meridional overturning circulation. *J. Phys. Oceanogr.*, accepted.
- Dierking, W., 1995: Laser profiling of the ice surface topography during the winter Weddell gyre study 1992. *J. Geophys. Res.*, **100**, 4807-4820.

- Drijfhout, S. S., C. Heinze, M. Latif, E. Maier-Reimer, 1996: Mean circulation and internal variability in an ocean primitive equation model. *J. Phys. Oceanogr.*, **26**, 559-580.
- Drusch, M., 2006: Sea ice concentration analyses for the Baltic Sea and their impact on numerical weather prediction. *J. Appl. Meteorol. Climatol.*, **45**, 982-994.
- Fichefet, T., and M. A. Morales Maqueda, 1997: Sensitivity of a global sea ice model to the treatment of ice thermodynamics and dynamics, *J. Geophys. Res.*, **102**, 12,609-12,646.
- Fyfe, J. C., O. A. Saenko, K. Zickfeld, M. Eby, and A. J. Weaver, 2007: The role of poleward-intensifying winds on Southern Ocean warming. *J. Climate*, **20**, 5391-5400.
- Ganachaud, A., and Wunch, C., 2000: Improved estimates of global ocean circulation, heat transport and mixing from hydrographic data. *Nature*, **408**, 453-456.
- Garbrecht, T., C. Lüpkes, J. Hartmann, and M. Wolff, 2002: Atmospheric drag coefficients over sea ice – validation of a parameterization concept. *Tellus*, **54A(2)**, 205-219.
- Gent, P. R., and J. C. McWilliams, 1990: Isopycnal mixing in ocean circulation models. *J. Phys. Oceanogr.*, **20**, 150-155.
- Gent, P. R., W. G. Large, and F. O. Bryan, 2001: What sets the mean transport through Drake Passage? *J. Geophys. Res.*, **106**, 2693-2712.
- Gent, P. R., J. Willebrand, T. J. McDougall, and J. C. McWilliams, 1995: Parameterizing eddy-induced tracer transports in ocean circulation models, *J. Phys. Oceanogr.*, **25**, 463-474.
- Gent, P. R., A. P. Craig, C. M. Bitz, and J. W. Weatherly, 2002: Parameterization improvement in an eddy-permitting ocean model for climate. *J. Climate*, **15**, 1447-1459.
- Gille, S. T., 2002: Warming of the Southern Ocean since the 1950s. *Science*, **295**, 1275-1277.
- Gloersen, P., Campbell, W. J., Cavalieri, D. J., Comiso, J. C., Parkinson, C. L., and Zwally, H. J., 1992: Arctic and Antarctic sea ice, 1978-1987: Satellite passive microwave observations and analysis. Spec.Publ., NASA SP-511, NASA, Washington, D.C.
- Gong, D., and S. Wang, 1999: Definition of Antarctic Oscillation index. *Geophys. Res. Lett.*, **26**, 459-462.

- Gnanadesikan, A., 1999: A simple predictive model for the structure of the oceanic pycnocline. *Science*, **283**, 2077-2079.
- Gnanadesikan A., and R. W. Hallberg, 2000: On the relationship of the Circumpolar Current to Southern Hemisphere winds in coarse-resolution ocean models. *J. Phys. Oceanogr.*, **30**, 2013-2034.
- Gordon, A. L., 1982: Weddell Deep Water variability. *J. Mar. Res.*, **40**, 199-217.
- Goosse, H., and T. Fichefet, 2001: Open-ocean convection and polynyas formation in a large-scale ice – ocean model. *Tellus*, **53**, 94-111.
- Grötzner, A., R. Sausen, and M. Claussen, 1996: The impact of sub-grid scale sea-ice inhomogeneities on the performance of the atmospheric general circulation model ECHAM3. *Climate Dyn.*, **12**, 477-496.
- Hall, A., and M. Visbeck, 2002: Synchronous variability in the Southern Hemisphere atmosphere, sea ice, and ocean resulting from the annular mode. *J. Climate*, **15**, 3043-3057.
- Hallberg, R., and A. Gnanadesikan, 2001: An exploration of the role of transient eddies in determining the transport of zonally reentrant current, *J. Phys. Oceanogr.*, **31**, 3312-3330.
- Hallberg, R., and A. Gnanadesikan, 2006: The role of eddies in determining the structure and response of the wind-driven Southern Hemisphere overturning: Results from the Modeling Eddies in the Southern Ocean (MESO) Project. *J. Phys. Oceanogr.*, **36**, 2232-2252.
- Hanssen-Bauer I., and Y. T. Gjessing, 1988: Observations and model calculations of aerodynamic drag on sea ice in the Fram strait. *Tellus*, **40A**, 151-161.
- Harms, S., Fahrbach, E., and Strass, V. H., 2001: Sea ice transports in the Weddell Sea. *J. Geophys. Res.*, **106**, 9057-9073.
- Hartmann, D. L., and F. Lo, 1998: Wave-driven zonal flow vacillation in the Southern Hemisphere. *J. Atmos. Sci.*, **55**, 1303-1315.
- Hellerman, S., and M. Rosenstein, 1983: Normal monthly wind stress over the world ocean with error estimates. *J. Phys. Oceanogr.*, **13**, 922-927.
- Hellmer, H. H., 2004: Impact of Antarctic ice shelf basal melting on sea ice and deep ocean properties. *Geophys. Res. Lett.*, **31**, L10307, doi:10.1029/2004GL019506
- Hibler, W. D. III, 1979: A dynamic thermodynamic sea ice model, *J. Phys. Oceanogr.*, **9**, 815-846.

- Hibler, W. D., III, and S. F. Ackley, 1983: Numerical simulations of the Weddell Sea pack ice. *J. Geophys. Res.*, **88**, 2873-2888.
- Killworth, P. D., 1983: Deep convection in the World Ocean. *Rev. Geophys.*, **21**, 1-26.
- Kim S.-J., and A. Stössel, 1998: On the representation of the Southern Ocean water masses in an ocean climate model. *J. Geophys. Res.*, **103** (C11), 24 891-24 906.
- Kim S. J., and A. Stössel, 2001: Impact of plume convection on global thermohaline properties and circulation. *J. Phys. Oceanogr.*, **31**, 656-674.
- Krupitsky, A., and M. A. Cane, 1994: On topographic pressure drag in a zonal channel. *J. Mar. Res.*, **52**, 1-22.
- Kushner, P. J., I. M. Held, and T. L. Delworth, 2001: Southern Hemisphere atmospheric circulation response to global warming. *J. Climate*, **14**, 2238-2249.
- Levitus, S., 1982: *Climatological Atlas of the World Ocean*. NOAA Prof. Paper No. 13, U.S. Govt. Printing Office, Washington, DC, 173 pp.
- Limpasuvan, V., and D. Hartmann, 2000: Wave-maintained annular modes of climate variability. *J. Climate*, **13**, 4414-4429.
- Locarnini, R. A., A. V. Mishonov, J. I. Antonov, T. P. Boyer, and H. E. Garcia, 2006: *World Ocean Atlas 2005*, Volume 1: Temperature. S. Levitus, Ed. NOAA Atlas NESDIS 61, U.S. Gov. Printing Office, Washington, DC, 182pp.
- Lorenz, D. J., and D. L. Hartmann, 2001: Eddy-zonal flow feedback in the Southern Hemisphere. *J. Atmos. Sci.*, **58**, 3312-3327.
- Louis J. F., 1979: A parametric model of vertical eddy fluxes in the atmosphere. *Boundary-Layer Meteorol.*, **17**, 187-202.
- Lüpkes, C., and G. Birnbaum, 2005: Surface drag in the Arctic marginal sea-ice zone: A comparison of different parameterization concepts. *Boundary-Layer Meteorol.*, **117**, 179-211.
- Markus, T., Kottmeier, C., and Fahrbach, E., 1998: Ice formation in coastal polynyas in the Weddell Sea and their impact on oceanic salinity. In: Antarctic sea ice: physical processes, interactions and variability. AGU, Antarctic Research Series, **74**, 273-292.
- Markus, T. and Cavalieri, 2000: An enhancement of the NASA Team sea ice algorithm. *IEEE Trans. Geosc. and Remote Sens.*, **38**(3), 1387-1398.
- Marshall, G. J., 2003: Trends in the southern annular mode from observations and reanalyses. *J. Climate*, **16**, 4134-4143.

- Marshall, J., and T. Radko, 2003: Residual-mean solutions for the Antarctic Circumpolar Current and its associated overturning circulation. *J. Phys. Oceanogr.*, **33**, 2341-2354.
- Marshall, K., 1971: Drag measurements in roughness arrays of varying density and distribution. *Agr. Meteorol.*, **8**, 269-292.
- Mason, P. J., 1988: The formation of areally averaged roughness lengths. *Quart. J. Roy. Meteorol.*, **114**, 399-420.
- Massom, R.A., Eicken, H., Haas, C., Jeffries, M.O., Drinkwater, M.R., Sturm, M., Worby, A.P., Wu, X., Lytle, V.I., Ushio, S., Morris, K., Reid, P.A., Warren, S.G., and Allison, I., 2001: Snow on Antarctic sea ice. *Rev. Geophys.*, **39**, 413-445.
- Ogura, T., A. Abe-Ouchi, and H. Hasumi, 2004: Effects of sea ice dynamics on the Antarctic sea ice distribution in a coupled ocean atmosphere model, *J. Geophys. Res.*, **109**, C04025.
- Oke, P. R., and M. H. England, 2004: Oceanic response to changes in the latitudes of the Southern Hemisphere Subpolar Westerly Winds. *J. Climate*, **17**, 1040-1054.
- Olbers, D., 1998: Comments on "On the obscurantist physics of 'form drag' in theorizing about the Circumpolar Current." *J. Phys. Oceanogr.*, **28**, 1647-1654.
- Orsi, A. H., W. D. Nowlin, and T. Whitworth, 1993: On the circulation and stratification of the Weddell Gyre. *Deep-Sea Res.*, **40**, 169-203.
- Owens, W. B., and P. Lemke, 1990: Sensitivity studies with a sea ice – mixed layer – pycnocline model in the Weddell Sea. *J. Geophys. Res.*, **95**, 9527-9538.
- Paluszkiwicz, T., and R. D. Romea, 1997: A one-dimensional plume model for the parameterization of oceanic deep convection. *Dyn. Ocean and Atmos.*, **26**, 95-130.
- Parkinson, C. L., and W. M. Washington, 1979: A large-scale numerical model of sea ice. *J. Geophys. Res.*, **84**, 311-337.
- Pease, C.H., 1987: The size of wind-driven coastal polynyas. *J. Geophys. Res.* **92(C7)**, 7049-7059.
- Pinto, J. O., Alam, A., Maslanik, J. A., Curry, J. A. and Stone, R. S., 2003: Surface characteristics and atmospheric footprint of springtime Arctic leads at SHEBA. *J. Geophys. Res.*, **108**, 8051, doi: 10.1029/2000JC000473.
- Pollard, R. T., and R. O. R. Y. Thompson, 1994: Sea-ice dynamics and CO₂ sensitivity in a global climate model. *Atmos. Ocean*, **32**, 449-467.

- Powell, D.C., Markus, T., and Stössel, A. 2005. Effects of snow depth forcing on Southern Ocean sea ice simulations. *J. Geophys. Res.*, 110 (C6), C06001, doi:10.1029/2003JC002212.
- Rahmstorf, S., 1995: Multiple convection patterns and thermohaline flow in an idealized OGCM, *J. Climate*, **8**, 3028-3039.
- Rahmstorf, S., and M. H. England, 1997: Influence of Southern Hemisphere winds on North Atlantic Deep Water flow. *J. Phys. Oceanogr.*, **27**, 2040-2054.
- Renfrew, I. A., King, J. C., and Markus, T., 2002: Coastal polynyas in the southern Weddell Sea: variability of the surface energy budget. *J. Geophys. Res.*, **107**(C6), 10.1029/2000JC000720.
- Ribbe, J., 1999: On wind-driven mid-latitude convection in ocean general circulation models. *Tellus*, **51A**, 517-525.
- Rintoul, S. R., and M. H. England, 2002: Ekman transport dominates local air-sea fluxes in driving variability of subantarctic model water. *J. Phys. Oceanogr.*, **32**, 1308-1321.
- Russell, J. L., K. W. Dixon, A. Gnanadesikan, R. J. Stouffer, and J. R. Toggweiler, 2006: The Southern Hemisphere westerlies in a warming world: Propping open the door to the deep ocean, *J. Climate*, **19**, 6382-6390.
- Saenko O. A., A. Schmittner, and A. J. Weaver, 2002: On the role of wind-driven sea ice motion on ocean ventilation. *J. Phys. Oceanogr.*, **32**, 3376-3395.
- Santoso A., and M. H. England, 2004: Antarctic intermediate water circulation and variability in a coupled climate model. *J. Phys. Oceanogr.*, **34**, 2160-2179.
- Schmittner, A., and A. J. Weaver, 2001: Dependence of multiple climate states on ocean mixing parameters. *Geophys. Res. Lett.*, **28**, 1027-1030.
- Sen Gupta, A., and M. England, 2006: Coupled ocean-atmosphere-ice response to variation in the Southern Annular Mode. *J. Climate*, **19**, 4457-4486.
- Sijp, W. P., and M. H. England, 2006: Sensitivity of the Atlantic thermohaline circulation and its stability to basin-scale variations in vertical mixing. *J. Climate*, **19**, 5467-5478.
- Smith, S. D., R. D. Muench, and C. H. Pease, 1990: Polynyas and leads: an overview of physical processes and environment. *J. Geophys. Res.*, **95**, 9461-9479.
- Stössel, A., P. Lemke, and W. B. Owens, 1990: Coupled sea ice – mixed layer simulations for the Southern Ocean, *J. Geophys. Res.*, **95**, 9539-9555.

- Stössel, A., 1992: Sensitivity of Southern Ocean sea-ice simulation to different atmospheric forcing algorithms, *Tellus*, **44A**, 395-413.
- Stössel, A., and M. Claussen, 1993: On the momentum forcing of a large-scale sea-ice model. *Climate Dyn.*, **9**, 71-80.
- Stössel A., S.-J. Kim, and S. S. Drijfhout, 1998: The impact of Southern Ocean Sea Ice in a Global Ocean Model, *J. Phys. Oceanogr.*, **28**, 1999-2018.
- Stössel, A. and S.-J. Kim, 2001: Decadal deep-water variability in the subtropical Atlantic and convection in the Weddell Sea. *J. Geophys. Res.*, **106**, 22,425-22,440.
- Stössel, A., and Kim. J.-T., 2006: Enhancing the resolution of sea ice in a global ocean GCM. *Ocean Modell.*, **11**, 28-48.
- Stössel A., W.-G. Cheon, and T. Vihma, 2008: Interactive momentum flux forcing over sea ice in a global ocean GCM, *J. Geophys. Res.*, **113**, C05010, doi:10.1029/2007JC004173.
- Stössel, A., Stössel, M.M., and Kim. J.-T., 2007: High-resolution sea ice in long-term global ocean GCM integrations, *Ocean Modell.*, **16**, 206-223.
- Stössel, A., 2008: Employing satellite-derived sea-ice concentration to constrain upper-ocean temperature in a global ocean GCM. *J. Climate*, in press.
- Sørensen, J. V. T., J. Ribbe, and G. Shaffer, 2001: Antarctic Intermediate Water mass formation in ocean general circulation models. *J. Phys. Oceanogr.*, **31**, 3295-3311.
- Thompson, D. W. J., and J. M. Wallace, 2000: Annular modes in the extratropical circulation. Part I: Month-to-month variability. *J. Climate*, **13**, 1000-1016.
- Thompson, D. W. J., J. M. Wallace, and G. C. Hegerl, 2000: Annular modes in the extratropical circulation. Part II: Trends. *J. Climate*, **13**, 1018-1036.
- Thompson, D. W. J., M P. Baldwin, and S. Solomon, 2005: Stratosphere-troposphere coupling in the Southern Hemisphere. *J. Atmos. Sci.*, **62**, 1018-1036.
- Toggweiler, J. R., and B. Samuels, 1993: Is the magnitude of the deep outflow from the Atlantic Ocean actually governed by Southern Hemisphere winds? *The Global Carbon Cycle*, M Heimann, Ed., Springer, 303-331.
- Toggweiler, J. R. and B. Samuels, 1995: Effect of Drake Passage on the global thermohaline circulation. *Deep-Sea Res.*, **42**, 477-500.
- Toggweiler, J. R., J. L. Russell, and S. R. Carson, 2006: Midlatitude westerlies, atmospheric CO₂, and climate change during the ice ages. *Paleoceanography*, **21**, PA2005, doi:10.1029/2005PA001154.

- Uotila, J., Vihma, T., and Launiainen, J., 2000: Response of the Weddell Sea pack ice to wind forcing. *J. Geophys. Res.*, **105**(C1), 1135-1151.
- Vihma, T., 1995: Subgrid parameterization of surface heat and momentum fluxes over polar oceans, *J. Geophys. Res.*, **100**, 22,625-22,646.
- Vihma, T., Uotila, B., Cheng, B., and Launiainen, J., 2002: Surface heat budget over the Weddell Sea: buoy results and model comparisons. *J. Geophys. Res.*, **107**(C2), 2000JC000372.
- Vihma, T. and Brümmer, B., 2002: Observations and modelling of on-ice and off-ice air flows over the northern Baltic Sea. *Boundary-Layer Meteorol.*, **103**, 1-27.
- Vihma, T., C. Lüpkes, J. Hartmann, and H. Savijärvi, 2005: Observations and modeling of cold-air advection over Arctic sea ice. *Boundary-Layer Meteorol.*, **117**, 275-300.
- Visbeck, M., J. Marshall, T. Haine, and M. Spall, 1997: Specification of eddy transfer coefficients in coarse-resolution ocean circulation models, *J. Phys. Oceanogr.*, **27**, 381-402.
- Wadhams, P., 2000: *Ice in the Ocean*, Gordon and Breach Science Publishers, Chapter 1-2, 1-138.
- Wang, L., 1994: A linear homogeneous channel model for topographic control of the Antarctic Circumpolar Current. *J. Mar. Res.*, **52**, 649-685.
- Warren, B., J. LaCasce, and P. A. Robbins, 1996: On the obscurantist physics of “form drag” in theorizing about the Circumpolar Current. *J. Phys. Oceanogr.*, **26**, 2297-2301.
- Winton, M., 2003: On the climatic impact of ocean circulation. *J. Climate*, **16**, 2875-2889.
- Wolff, J. -O., E. Maier-Reimer, and S. Legutke, 1997: The Hamburg Ocean Primitive Equation model HOPE, Tech. Rep. 13, deutsches Klimarechenzentrum, Hambrug, Germany, 98pp.
- Wu, X., W. F. Budd, and I. Simmonds, 1997: Sensitivity of the Antarctic sea ice distribution to its advection in a general circulation model, *Antarct. Sci.*, **9**, 445-455.

APPENDIX I
MODEL PHYSICS

A. Physics for the ocean model

The following mostly refers to the original recorded in the Max-Planck-Institute for Meteorology (MPI-M) technical report No. 13. HOPE is based on the non-linear balance equation for momentum (the equations of motion), the continuity equation for incompressible fluid, and conservation equations for heat and salt. The model employs the hydrostatic and Boussinesq approximations. Prognostic ocean variables are horizontal velocities, sea surface elevation, potential temperature, and salinity.

The horizontal momentum balance equations are (here written schematically in rectilinear coordinates for simplicity):

$$\frac{d\vec{v}}{dt} + f(\vec{k} \times \vec{v}) = -\frac{1}{\rho_0} [\vec{\nabla}_H(p + \rho_0 g \zeta)] + F_H + F_V, \quad (\text{AIA-1})$$

where $\vec{v} = (u, v)$ is the horizontal velocity vector, f the Coriolis parameter, \vec{k} an upward vertical unit vector, ρ_0 a reference density, g the gravitational acceleration, $p = g \int_h^0 \rho dz$ the internal pressure, and ζ the sea surface elevation.

The horizontal and vertical turbulent viscous terms \vec{F}_H and \vec{F}_V are specified according to K-theory. A number of formations can be used in combination. These are harmonic and biharmonic formations

$$\vec{F}_{H1} = A_H \nabla^2(\vec{v}) \quad (\text{AIA-2})$$

$$\vec{F}_{H2} = -B_H \nabla^4(\vec{v}), \quad (\text{AIA-3})$$

and a viscous dissipation depending on the local rate of strain

$$\bar{F}_{H3} = \nabla \left[\nu_A T^2 \bar{\nabla}_H (\bar{v}) \right]. \quad (\text{AIA-4})$$

A_H , B_H , and ν_A are constant coefficient, and T^2 is a function of the local rate of strain $\partial v / \partial x + \partial u / \partial y$. The vertical eddy viscosity is parameterized as:

$$\bar{F}_V = \frac{\partial}{\partial z} \left(A_V \frac{\partial \bar{v}}{\partial z} \right), \quad (\text{AIA-5})$$

where the eddy coefficient A_V can be specified to depend on the local Richardson number. The harmonic viscosity parameter A_H is grid-size dependent. It is $3 \times 10^5 m^2 s^{-1}$ at the equator, otherwise proportional to the relative surface of the grid box. The vertical eddy viscosity parameter A_V is $2 \times 10^{-4} m^2 s^{-1}$.

The internal pressure p is related to the density field by the hydrostatic approximation

$$\frac{\partial p}{\partial z} = -g\rho. \quad (\text{AIA-6})$$

The density is calculated with a non-linear polynomial depending on salinity, temperature, and pressure (UNESCO 1983). The vertical velocity w is calculated diagnostically from the incompressible condition (continuity equation)

$$\frac{\partial w}{\partial z} = -\nabla \bar{v}. \quad (\text{AIA-7})$$

In case of unstable stratification, convective adjustment is applied; that is, each pair of vertically adjacent grid cells is perfectly mixed under consideration of heat and salt conservation.

The sea surface elevation is calculated from the linearized kinematic boundary condition

$$\frac{\partial \zeta}{\partial t} = w|_{z=0} + Q_\zeta = -\nabla \int_{-H}^0 \bar{v} dz + Q_\zeta, \quad (\text{AIA-8})$$

where $H(x, y)$ is the water depth, and Q_ζ the fresh water forcing of the free surface. At the sea surface, a momentum flux must be specified:

$$\rho_0 A_V \left. \frac{\partial \bar{v}}{\partial z} \right|_{z=0} = \bar{\tau}. \quad (\text{AIA-9})$$

Bottom friction is computed applying a Newtonian friction law. No-slip boundary conditions are used at lateral boundaries.

To solve the momentum equation (AI-1), a method of fractional step is used. First, (AI-1) is solved omitting the nonlinear advection terms and the viscous dissipation. The velocities are decomposed into a barotropic and baroclinic part. Then, the barotropic velocities are solved implicitly by direct matrix inversion. The baroclinic subsystem is written in a semi-implicit form and solved by an iterative method. Nonlinear advection is computed with a discretization scheme that guarantees both conservation of kinetic energy and enstrophy (Arakawa and Lamb 1977). Vertical advection and mixing are computed implicitly. Horizontal mixing is computed by an explicit method.

Potential temperature θ and salinity S are determined from the continuity equations:

$$\frac{dS}{dt} = \frac{\partial}{\partial z} \left(D_V \frac{\partial S}{\partial z} \right) + D_H \nabla^2(S) + \nabla \left[\nu_D T^2 \bar{\nabla}_H(S) \right] \quad (\text{AIA-10})$$

$$\frac{d\theta}{dt} = \frac{\partial}{\partial z} \left(D_V \frac{\partial \theta}{\partial z} \right) + D_H \nabla^2(\theta) + \nabla \left[\nu_D T^2 \bar{\nabla}_H(\theta) \right] \quad (\text{AIA-11})$$

where ν_D and D_H are constant coefficient, and T^2 is defined as for the horizontal viscosity. The vertical eddy diffusivity D_V can be specified to depend on the local Richardson number. Salinity is restored to the annual mean sea surface salinity (Levitus

1982) with a timescale of 40 days. Solar radiation is parameterized by a simple geometrical function, dependent on the latitude and the day of the year. Maximum input is 63 Wm^{-2} in the surface layer of 50 m .

The salinity boundary condition forces also changes in ζ by calculating the equivalent freshwater flux. At lateral boundaries and the seafloor no-flux conditions apply for heat and salt. The advection and horizontal diffusion of temperature and salinity are computed by a half-split method (Arakawa and Lamb 1977; the same method used to compute the nonlinear horizontal momentum advection). Vertical mixing of the thermohaline fields is solved implicitly.

B. Physics for the sea-ice model

1. Dynamic part

The following mostly refers to the original recorded in the Max-Planck-Institute for Meteorology (MPI-M) technical report No. 3. The dynamic part of the model was developed by Hibler (1979) and is characterized by the following equation of motion:

$$\rho_i h_i \frac{d\vec{v}_i}{dt} = -\rho_i h_i f \vec{k} \times \vec{v}_i + \vec{\tau}_a + \vec{\tau}_o - \rho_i h_i g \vec{\nabla} H + \vec{F} \quad (\text{AIB-1})$$

where

- ρ_i : sea-ice density,
- h_i : mean ice thickness within a grid cell,
- \vec{v}_i : ice velocity,
- t : time,
- f : Coriolis parameter,
- \vec{k} : unit vector normal to the surface,

- $\bar{\tau}_a$: stress at the interface atmosphere/sea ice,
 $\bar{\tau}_o$: stress at the interface sea ice/ocean,
 g : gravitational acceleration,
 H : height of dynamic topography,
 \vec{F} : force due to internal ice stress.

The surface stresses are calculated by bulk formula, e.g. $\bar{\tau}_o$ as:

$$\bar{\tau}_o = \rho_o C_{do} |\vec{v}_{og} - \vec{v}_i| \left[(\vec{v}_{og} - \vec{v}_i) \cos \phi_o + \vec{k} \times (\vec{v}_{og} - \vec{v}_i) \sin \phi_o \right], \quad (\text{AIB-2})$$

- where
- ρ_o : sea-water density,
 C_{do} : drag coefficient for the interface sea ice/ocean,
 \vec{v}_{og} : geostrophic current,
 ϕ_o : deviation angle.

Here, the relative velocity between ice drift and ocean current is used, whereas in the calculation of $\bar{\tau}_a$ the ice velocity can be neglected. Since usually $|\vec{v}_{og}| < |\vec{v}_i|$, $\bar{\tau}_o$ effectively slows down the movement of ice.

The components of \vec{F} are determined from:

$$F_i = \frac{\partial \sigma_{ij}}{\partial x_j}, \quad (\text{AIB-3})$$

(Eqs (5) and (6) in Hibler (1979)), where σ_{ij} represents the two-dimensional stress tensor. This is considered to obey a constitute law of a non-linear viscous compressible fluid:

$$\sigma_{ij} = 2\eta \dot{\epsilon}_{kk} \delta_{ij} - \frac{p \delta_{ij}}{2}, \quad (\text{AIB-3a})$$

$$\text{with } \zeta = \frac{P}{2\Delta}, \quad (\text{AIB-3b})$$

$$\eta = \frac{\zeta}{e^2}, \quad (\text{AIB-3c})$$

$$P = P^* h_i e^{[-C^*(1-N_i)]}, \quad (\text{AIB-3d})$$

$$\text{and } \Delta = \left\{ e^{-2} \left[(\dot{\epsilon}_{11} - \dot{\epsilon}_{22})^2 + 4\dot{\epsilon}_{12}^2 \right] + (\dot{\epsilon}_{11} + \dot{\epsilon}_{22})^2 \right\}^{1/2}, \quad (\text{AIB-3e})$$

where p : ice strength,

p^* : empirical ice strength parameter,

C^* : empirical constant,

ζ : bulk viscosity,

η : shear viscosity,

e : ratio of compressive to shear strength,

$\dot{\epsilon}_{ij}$: deformation-rate tensor,

N_i : ice compactness (=ice coverage per grid cell = ice concentration).

The stress-strain rate is described by the associated flow rule (Hibler 1977). The viscous-plastic rheology represents an elliptical yield curve in principle component stress space, which determines the ratio of compressive to shear strength (Leppäranta and Hibler 1985).

2. Thermodynamic part

In the thermodynamic part of the model, the heat balance equation is solved separately for the open water and the ice covered part of a grid cell, following Semtner (1976) and Parkinson and Washington (1979).

Over ice:

$$(1 - \alpha)Q_{sw} + Q_{lw} - \varepsilon\sigma T_s^4 + Q_{se} + Q_{la} + Q_c \equiv Q_a + Q_c = 0, \quad (\text{AIB-4})$$

where

- α : albedo (of ice or snow),
- Q_{sw} : shortwave radiation heat flux,
- Q_{lw} : longwave radiation heat flux,
- ε : emissivity (of ice or snow),
- T_s : surface temperature (of ice or snow),
- Q_{se} : sensible heat flux,
- Q_{la} : latent heat flux,
- Q_c : conductive heat flux through the ice,
- Q_a : atmospheric heat flux.

The radiation and turbulent heat fluxes are calculated by standard (bulk) formulae (similar to Parkinson and Washington, 1979). The albedo is allowed to vary with snow cover and freezing or melting conditions.

The conductive heat flux yields:

$$Q_c = \frac{(T_b - T_s) \cdot k_i}{\tilde{h}_i}, \quad (\text{AIB-5})$$

where T_b : temperature at the ice bottom (=freezing point),

k_i : thermal conductivity of ice,

and $\tilde{h}_i = \frac{\hat{h}_i}{N_i}$ (AIB-6)

where \tilde{h}_i : “effective” ice thickness,

$$\tilde{h}_i = h_i + h_{sn} \frac{k_i}{k_{sn}} \quad (\text{AIB-7})$$

where \hat{h}_i : “total” ice thickness,

k_{sn} : thermal conductivity of snow.

For the ice-covered part, the heat balance equation (AIB-4) can now be calculated with the locally existing effective ice thickness (AIB-6). Changing the actual snow thickness into an equivalent ice thickness, the total ice thickness (AIB-7) implicitly includes the insulation effect of snow.

T_s is determined from (AIB-4) by iteration. If T_s is higher than 0° , it is set to 0°C and (AIB-4) identical to $-\rho_i L_f \left(\frac{\partial \tilde{h}_i}{\partial t} \right)_s$ in order to derive the change of ice thickness due to surface melt (Maykut 1982):

$$\left(\frac{\partial \tilde{h}_i}{\partial t} \right)_s = \frac{1}{\rho_i L_f} (-Q_a - Q_c), \quad (\text{AIB-8})$$

where L_f : latent heat of fusion.

At the bottom of the ice:

$$\left(\frac{\partial \tilde{h}_i}{\partial t} \right)_b = \frac{1}{\rho_i L_f} (Q_a - Q_o), \quad (\text{AIB-9})$$

where Q_o : oceanic heat flux.

Thus the total change of the effective ice thickness yields:

$$\left(\frac{\partial \tilde{h}_i}{\partial t}\right) = \left(\frac{\partial \tilde{h}_i}{\partial t}\right)_b + \left(\frac{\partial \tilde{h}_i}{\partial t}\right)_s \delta_{jk}, \quad (\text{AIB-10})$$

where $j = k$, if $T_s = 0^\circ\text{C}$,

and $\delta_{jk} = 1$, if $j = k$

0, if $j \neq k$.

In order to include the new-ice production in the ice free part of a grid cell, the total thermodynamic change of ice thickness (Hibler, 1979; Owens and Lemke, 1990) combines to:

$$\left(\frac{\partial \tilde{h}_i}{\partial t}\right)_{th} = N_i \left(\frac{\partial \tilde{h}_i}{\partial t}\right) \delta_{jk} + (1 - N_i) \left(\frac{\partial h'_i}{\partial t}\right), \quad (\text{AIB-11})$$

where $j = k$, if $(\partial \tilde{h}_i / \partial t) < 0$ and $h_{sn} > 0$,

h'_i : new-ice thickness.

Here, $\delta_{jk} = 0$ applies for snow, which in this case is melted first according to (AIB-13).

The new-ice production, given in the second term of (AIB-11), is determined from (AIB-4), using the albedo of water and the ocean surface temperature (i.e. the mixed-layer temperature).

The thermodynamic change of ice compactness is determined empirically (Hibler, 1979):

$$\left(\frac{\partial N_i}{\partial t}\right)_{th} = \frac{(1 - N_i)}{h^*} \left(\frac{\partial h'_i}{\partial t}\right) \delta_{jk} + \frac{N_i}{2h_i} \left(\frac{\partial h_i}{\partial t}\right)_{th} \delta_{ln}, \quad (\text{AIB-12})$$

where $j = k$, if $(\partial h'_i / \partial t) > 0$,

$l = n$, if $(\partial h_i / \partial t)_{th} < 0$,

h_* : empirical parameter.

In the first term on the right hand side of (AIB-12) h^* determines the rate of lead closing. In the second term it is assumed that in the case of ice melting, the ice within a grid cell is equally distributed between twice the mean ice thickness and zero. That part of the grid cell, which became ice free due to vertical ice melting, subsequently determines the reduction of ice compactness, i.e. the so called lateral ice melting.

According to Owens and Lemke (1990) the thermodynamic change of snow thickness is treated as follows:

$$\left(\frac{\partial h_{sn}}{\partial t}\right)_{th} = N_i P_w \frac{\rho_w}{\rho_{sn}} \delta_{jk} + N_i \left(\frac{\partial \tilde{h}_i}{\partial t}\right) \frac{\rho_i}{\rho_{sn}} \delta_{sn}, \quad (\text{AIB-13})$$

where $j = k$, if $T_a \leq 0^\circ\text{C}$,
 $l = n$, if $(\partial \tilde{h}_i / \partial t) < 0$ and $h_{sn} > 0$,
 P_w : precipitation rate,
 ρ_w : fresh-water density,
 ρ_{sn} : snow density.

In order to avoid exaggerated accumulation of snow on multi-year ice, a snow to ice conversion is introduced. It applies whenever the weight of the snow exceeds the buoyancy of the ice-plus-snow column to an extension that the snow submerges below the water line.

A further modification to Hibler (1979) is a seven-level ice-thickness parameterization:

$$\left(\frac{\partial \tilde{h}_i}{\partial t}\right) \equiv w_i(\tilde{h}_i) = \frac{1}{n} \sum_{k=1}^n w_i \left(\frac{(2k-1)\tilde{h}_i}{n}\right), \quad (\text{AIB-14})$$

where $n = 7$: number of levels,
 w_i : ice-growth rate.

With (AIB-14) the heat balance equation is calculated for seven ice-thickness categories, thus taking into account the highly non-linear relationship between growth rate and ice thickness.

3. Continuity equations

The link between the dynamic and the thermodynamic part of the model is given by continuity equations for ice thickness, ice compactness and snow thickness:

$$\frac{\partial h_i}{\partial t} = -\tilde{\nabla} \cdot (\tilde{v}_i h_i) + \left(\frac{\partial h_i}{\partial t} \right)_{th} + diffusion , \quad (\text{AIB-15})$$

$$\frac{\partial N_i}{\partial t} = -\tilde{\nabla} \cdot (\tilde{v}_i N_i) + \left(\frac{\partial N_i}{\partial t} \right)_{op} + \left(\frac{\partial N_i}{\partial t} \right)_{th} + diffusion , \quad (\text{AIB-16})$$

$$\frac{\partial h_{sn}}{\partial t} = -\tilde{\nabla} \cdot (\tilde{v}_i h_{sn}) + \left(\frac{\partial h_{sn}}{\partial t} \right)_{th} + diffusion , \quad (\text{AIB-17})$$

where h_{sn} is the mean snow thickness and where the index th represents thermodynamic terms, which will be illustrated in the previous section. The ice velocities in the advection terms are derived from the dynamic part.

VITA

Woo Geun Cheon was born in Seoul, Republic of Korea on August 25, 1975 of Whan Sook Lim and Jin Cheon. He received his B.S. and M.S. degrees in Atmosphere Sciences from Yonsei University in 2000 and 2003, respectively. After working for one year at the Korea Oceanographic Research Development Institute, he went to Texas A&M University to pursue his Ph.D. degree in physical oceanography. He received his Ph.D. degree in August 2008.

Permanent Address: Samsung APT 303-904, Topyong-dong, Guri-si, Kyonggi-do, Republic of Korea, 471-761.